UNIVERSITY
of
GLASGOW

InAlGaAs-InP Laterally Coupled DBR and DFB Lasers for Microwave Generation

by Francesca Pozzi

April 2007

A thesis submitted for the degree of
Doctor of Philosophy (Ph.D.) to the Faculty of Engineering
Department of Electronics and Electrical Engineering
University of Glasgow

In nature's infinite book of secrecy
A little I can read

William Shakespeare

Abstract

The work reported in this thesis is concerned with the fabrication and characterisation of laterally coupled (LC) distributed feedback (DFB) lasers, both single- and dual-mode, based on InAlGaAs-InP material emitting at 1.35 μm. The aim of the research is to realise a compact device, able to emit two wavelengths simultaneously, to be used for the generation of gigahertz (GHZ) and terahertz (THz) signals by photo-mixing. The motivation comes from the need for portable sources of radiation in the so-called THz region. The first part of the work involved the implementation of a laterally coupled grating that is intended to become a building block for the dual-wavelength device. To prove the effectiveness of the grating structure, single-mode DFBs and distributed Bragg reflector (DBR) lasers were designed and fabricated in the InAlGaAs-InP material, aiming to optimise the necessary technological processing. Assessment of these devices showed excellent performance: stable single-mode emission, with low threshold currents of about 55 mA and high sidemode suppression ratio (SMSR) over 40 dB, were demonstrated. Ridge-waveguide lasers (RWGL) were also fabricated alongside the single-mode devices, to allow comparison of the operating characteristics. The second part of the work was concerned with the implementation of a novel dual-wavelength laser, based on the lateral grating structure. The final device realised was a DFB laser having two different grating periods, one on each sidewall, fabricated in the InAlGaAs-InP material using the technology previously implemented. This source was thoroughly assessed in terms of lasing characteristics, mode behaviour, and suitability to generate microwave signals. Stable dual-mode operation, with low threshold currents around 50 mA and SMSR approaching 30 dB, was successfully demonstrated in continuous wave (CW) operating mode, at room temperature. The dual-mode behaviour was characterised by inspection of the modal transverse distribution and by injection locking experiments. Generation of microwave signals by photo-mixing was performed at about 23 GHz, and the linewidths of each of the individual modes and of the beat mode were measured as a function of the injection current. It was observed that, while the linewidth of the separate modes has a modest dependence on the injection level, the linewidth of the beat mode experiences a strong decrease as the injected current increases.

Acknowledgements

I want to express all my gratitude to my supervisor, Dr. Marc Sorel, who gave me the chance to carry out this research, supporting and encouraging me during all the time. My sincere thanks to Prof. Richard M. De La Rue, for his stimulating and valuable suggestions. My appreciation to Dr. Stephen Thoms, for introducing me to the "art" of e-beam lithography. Thanks to my friends and colleagues in the the Optoelectronics and Nanoelectronics Groups at the University of Glasgow, among them Barry Holmes, Corrie Farmer, Cross HK Tan, Dave Moran, Derrick HY Wong, Fiona McEwan, Franck Robert, Grant Erwin, Harold MH Chong, Marco Gnan, Michael Strain, Pierre Pottier, Richard Hill and Sandor Fürst, and to all the staff in the James Watt Nanofabrication Centre. Thanks also to Prof. Peter Laybourn and his family, for welcoming and encouraging me in my time in Glasgow. My appreciation goes to those in Italy who urged me to pursue this opportunity, Prof. Donati and Prof. Rigamonti, Guido Giuliani, Ilaria Cristiani and Marco Passerini. All my gratitude to Paoloplacido, my family and friends, for their encouragement and affection during such an important time in my life. Finally, I would like to acknowledge Fondazione Aurelio Beltrami and Università degli Studi di Milano for providing my financial support.

List of publications

Publications arising from this work

Journal Papers

F. Pozzi, R. M. De La Rue, M. Sorel, *Dual-wavelength InAlGaAs-InP laterally coupled distributed feedback laser*, IEEE Photonics Technology Letters, vol. 18, n. 24, pp. 2563-2565, December 2006.

Conference Proceedings

F. Pozzi, R. M. De La Rue, M. Sorel, *Laterally-coupled dual-wavelength distributed feedback lasers*, Proceedings of SPIE, Invited paper to Photonics Europe 2006, Strasbourg.

Conferences

F. Pozzi, M. Sorel, *Dual-wavelength distributed feedback lasers on InP/InAlGaAs*, PREP 2005, Lancaster.

Other Publications

Journal Papers

R. Iyer, F. Pozzi, M. Sorel, Z. Yang, P. Chak, J. E. Sipe, and J. S. Aitchison, *Integrated AlGaAs side-coupled racetrack microring resonators with up to eight periods*, submitted to Photonics Technology Letters.

F. Pozzi, M. Sorel, G.A. Siviloglou, S. Suntsov, R. El-Ganainy, R. Iwanow, G.I. Stegeman, D.N. Christodoulides, D. Modotto, A. Locatelli, C. De Angelis and R. Morandotti, *Enhanced third-order nonlinear effects in ultra-compact AlGaAs nanowires*, OSA Optics & Photonics News, End-of-year Special Issue "Optics in 2006", p.36, December 2006.

G. A. Siviloglou, S. Suntsov, R. El-Ganainy, R. Iwanow, G. I. Stegeman, D. N. Christodoulides, R. Morandotti, D. Modotto, A. Locatelli, C. De Angelis, F. Pozzi, C. R. Stanley, M. Sorel, *Enhanced third-order nonlinear effects in optical AlGaAs nanowires*, Optics Express vol. 14, n. 20, pp. 9377-9384, October 2006.

Conferences

D. Duchesne, R. Morandotti, G. A. Siviloglou, R. El-Ganainy, G. I. Stegeman and D. N. Christodoulides, D. Modotto, A. Locatelli, C. De Angelis,F. Pozzi, M. Sorel, *Cross-phase modulation in AlGaAs photonic nanowires*, CLEO 2007, Baltimore.

Y. Lahini, A. Avidan, D. Mandelik, Y. Silberberg, F. Pozzi, M. Sorel, R. Morandotti, *Direct observation of Anderson localized modes and the effect of nonlinearity*, Post-deadline paper at Photonics Metamaterials 2006, Grand Bahama Island.

F. Pozzi, M. Sorel, Z.Yang, R.Iyer, P. Chak, J. Sipe, S. Aitchison, *Integrated high order filters in AlGaAs waveguides with up to eight side-coupled racetrack microresonators*, CLEO 2006, Long Beach.

R. Iwanow, G. Stegeman, D. Christodoulides, R. Morandotti, D. Modotto, A.

Locatelli, C. De Angelis, F. Pozzi, C. Stanley, M. Sorel, S. Aitchison, *Enhanced third order nonlinear effects in AlGaAs nanowires*, CLEO 2006, Long Beach.

S. Fürst, F. Pozzi, M. Sorel, *Optimisation of InP dry etching for the development of a rapidly tuneable semiconductor ring laser*, PREP 2005, Lancaster.

Contents

Introduction

Emission of radiation in the terahertz (THz) range, namely from tenths of GHz up to several THz, has been the subject of extensive research for the past couple of decades. The search has been driven on the one hand by keen interest in potential new applications, and on the other hand by a remarkable lack of sources able to emit efficiently in this range. Hence the expression "THz gap", that is conventionally defined to be between 300 GHz (1 mm) and 10 THz (30 μm). Although the result of work carried out has been the development of some commercial systems, for instance by Picometrix and TeraView, the quest for THz sources is still a very active topic of research. The main target nowadays is to create a compact and reliable device, able to work at room temperature.

Among the various methods to generate high frequency signals, one of the most promising is the optical heterodyne technique, also known as photo-mixing. It consists in the mixing of two optical signals at a fast photodetector, to generate an electrical signal at the frequency difference between the two modes. As a consequence of this interest in photo-mixing, dual-wavelength lasers have attracted much attention in the past few years as appealing sources for this application [IPHOBAC].

The aims of the present work

Dual-wavelength lasers, also known as dual-mode or two-colour lasers, are a particular type of multi-wavelength laser, specifically designed to emit two longitudinal

modes. Besides their application for THz generation, these devices are potentially key elements in various other applications, such as ultra-fast optical communications and optical spectroscopy.

Looking at the literature it appears that a variety of dual-wavelength systems have already been reported, from solid-state and fiber-based sources, to microchip and photonic devices. However, among all the reported configurations, simultaneous emission of the two modes from within the same laser cavity is the most appealing, due to its compactness, stability and spectral quality [Tani 05].

Starting from this observation, the present research has sought to develop a compact and reliable dual-wavelength laser diode, to be used to generate microwave signals by means of photo-mixing. The device has to be technologically as simple as possible, based on InP material, to guarantee its reliability and suitability for integration, and also be "flexible", in the sense that the basic structure has to allow for changes of design parameters. The building block that was chosen to implement the device is a shallow Bragg grating, also called lateral grating, since it is defined on the sidewalls of a ridge-waveguide structure (Fig. 1). This structure allows maximum flexibility in the definition of the grating reflectivity and period, and reduces the technological complexity, since it does not require regrowth. Moreover, since it is such a versatile structure, it has strong potential as a technological platform for photonic integrated circuits (PIC).

The final goal of the work is to demonstrate the feasibility of such a device, measuring its lasing characteristics and assessing its suitability for the generation of microwave signals.

Thesis outline

Chapter 1 of this thesis reports on the present status of research in the field of far-infrared (FIR) sources and integrated dual-wavelength lasers. The issue of GHz and THz signal generation is outlined, highlighting some applications of this

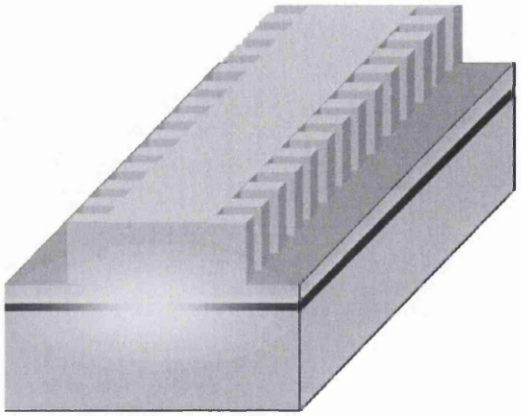

Figure 1: Schematic of the shallow lateral grating, defined on the side of a ridge-waveguide structure. The transversal profile of the optical mode propagating inside the core region is also shown.

latter type of radiation. Photonic techniques are then analysed in more detail; state-of-the-art dual-wavelength sources are described, focusing in particular on integrated devices. Finally, laser diodes based on lateral gratings are reviewed. Chapter 2 is an introduction to the analysis of single-mode Bragg lasers, that is DBRs and DFBs, based on the coupled-mode theory. Some properties of laser light and some physical effects which are of interest to this work are addressed. Chapter 3 describes how single- and dual-mode lasers were modelled. Design of the ridge-waveguide (RWG), lateral grating structure, and laser cavity for the single-mode devices are reported. The concept of common-mode-noise rejection effect is explained, and a simple model for the prediction of the behaviour of dual-wavelength lasers is presented. Although general, it proves very helpful for understanding the laser operation. Chapter 4 illustrates the fabrication work carried out. The structure of the epitaxial material employed is given; the process implemented to create lateral gratings is described; the fabrication steps required to define RWG lasers, as well as DBR and DFB lasers, are reported. Finally, the main fabrication

problems encountered during the research are addressed, with discussion of some potential improvements. Chapter 5 reports on the experimental results obtained from testing of the fabricated single-mode lasers. Their lasing characteristics, tuning behaviour and coupling coefficients are assessed. For completeness, results on ridge waveguide lasers fabricated on the same samples are also reported, to allow a comparison with the single-mode devices. Chapter 6 reports on results from testing of the dual-mode DFB lasers; similarly, these lasers are assessed in terms of lasing characteristics. Due to the novelty of the device, the properties of the transversal mode distribution are reported in more detail. Results from photomixing experiments follow, showing the potential of these devices for microwave generation. Assessment of the linewidths of the two sepate modes and of the beat signals are reported, and findings from optical injection locking experiments are given. Chapter 7 summarises the major achievements of this work, and provides some ideas for possible future work.

Chapter 1

Literature review and background

As a first step in this research, a comprehensive review of the relevant literature was carried out. In this Chapter, an overview on various techniques for the generation of high frequency signals is given, focusing in particular on photonic techniques, photo-mixing and related optical sources. Subsequently, since the proposed dual-wavelength device is based on a lateral grating, laser diodes incorporating such structures are thoroughly examined.

1.1 High frequency signals

In recent years, generation of signals at GHz and THz frequencies has attracted a lot of attention due to potential applications in several fields. High frequency signals are very appealing not only for ultrafast communications, but also in other areas, such as medicine, security and radio-astronomy. However, despite the interest in this range of frequencies, the portion of the electromagnetic (EM) spectrum ranging between microwaves and near-infrared (NIR) has substantially remained unexploited for a long time, due to a lack of suitable sources. In fact, this region is often referred to as *THz gap* [THz-network], to explicitly address the need for devices, stressing that this range of frequencies is on the one end covered by electronic sources, while on the other by optical devices. Wavelengthwise, this

interval is known as the far-infrared (FIR) range. Fig. 1.1 shows the electromagnetic spectrum, highlighting the absence of sources for the above-mentioned range of interest.

On the one side of the THz gap, there are traditional electronic sources that are based on high-speed electronic circuitry. Among them the fastest ones are impact avalanche transit time (IMPATT) diodes, Gunn diodes, and resonant tunneling diodes (RTD) [Dragoman 04], all of them able to generate frequencies below 1 THz, and frequency multipliers, which can emit up to a few THz. Although these types of devices are widely available at GHz frequencies and up, their operation above 1 THz faces major physical obstacles [Tredicucci 05]. An alternative electronic source is the micromachined reflex klystron, recently proposed to operate at several THz [Garcia-Garcia 04]. Nonetheless, it is important to point out that although these devices can generate up to a few THz, they are intrinsically very complex, hence very fragile.

On the other side of the gap, there are photonic systems, which traditionally generate radiation at hundreds of THz and higher. In this case, in order to generate the desired frequencies, the approach is either to engineer traditional sources to get them to emit at lower frequencies, or to define new devices, to be employed in specific optical configurations.

1.1.1 Some applications of FIR radiation

One of the major fields of application of FIR radiation is spectroscopy, in particular astronomical high-resolution spectroscopy. In fact, frequencies located in the millimeter-wave (mm-wave) range (30 - 300 GHz) are of interest to detect the so-called "cold Universe", since these regions are optically dark, but they are very bright in the mm-wave region [ALMA]. In this field, large telescopes are employed [CARMA], comprising arrays of large (>10 m) antenna dishes placed on earth, while a step forward is the making of complete radio telescopes, that can float in

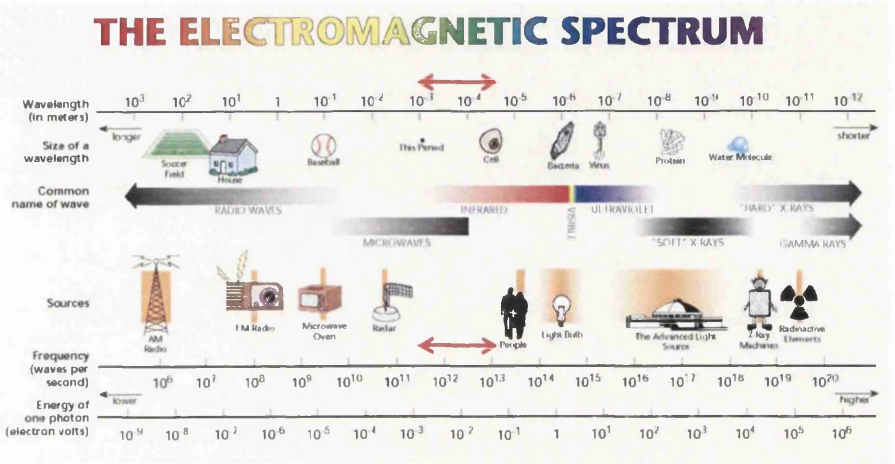

Figure 1.1: Depiction of the electromagnetic spectrum, showing the different ranges of frequencies [THz-network]. The THz gap is indicated by a red arrow.

space, as in [SWAS], or [SAFIR].

Millimetre-waves are also a significant area of research in the field of remote sensing, where FIR radiation finds applications in gas detection [Mittleman 98] and radar sensors for intelligent transport systems (ITS) [Abou-Jaoude 03].

In the field of optoelectronics, high frequency signals are of interest for applications in ultrafast communications, in particular for optical clock recovery in high-speed all-optical signal processing [Möhrle 01]. They have also been used to characterise semiconductors, as in [Huber 01], where ultrafast interactions were used to monitor charge-charge interactions.

Another major application of THz radiation is imaging, which looks very promising in various fields, from chemistry, biology and medicine, to industrial monitoring,

and homeland security. An interesting feature that makes THz waves very attractive is that they can penetrate nonconducting materials, such as clothing, wood and plastics, but they don't penetrate metals, and they are strongly absorbed by water [Mueller 06]. For this reason they could be employed in industrial applications, as for packaged good inspection, or to monitor microchip quality through imaging of integrated circuits.

Another main feature of THz waves is that their photon energy is much smaller than that of X-rays, which means that THz waves are nonionizing, hence safer for human applications. Today nondestructive imaging of biological samples is a very active area of research, as it appears by looking at the amount of published papers found in the literature, for instance the issue n. 47 (2002) of Physics in Medicine and Biology, or in [Koch 02]. As an example, a consortium of European Universities was recently involved with researching the effects of THz radiation onto biological systems [THz-BRIDGE]. Their conclusion is that medical imaging employing appropriate exposure parameters is not harmful, that THz systems may provide useful information in diagnostics applications, and they prove to be much less invasive than other commonly used techniques, like X-rays. Further applications to disease diagnostics are subject of research, for instance for tumour recognition [Woodward 03].

Potential monitoring applications, like gas sensing and biohazard detection, but also THz imaging of human beings, are eagerly looked for in the bustling field of security and defence [Woolard 05]. An example is given in Fig. 1.2, showing the potential of THz radiation in detecting concealed weapons.

At present, the main commercial application of THz waves is in the so-called terahertz time-domain spectroscopy, that measures materials properties at high frequency. The method is used to assess dielectric properties by measuring the field transmitted through them, then Fourier-transforming the time-domain wave to obtain amplitude and phase of the signal. From that the real and imaginary parts of the dielectric properties in the frequency domain are retrieved. This method has

been used on several materials already, from semiconductors and superconductors, to fluids and biological samples [Dorney 01], [Harde 01].

Figure 1.2: Application of millimetre-waves to security: the image shows a picture taken under natural light (left), and using THz radiation [THz-network] (right).

1.2 Photonic techniques for FIR generation

As mentioned earlier, due to physical limitations which are intrinsic to electronic devices, optical sources look today more promising in the quest to fill the THz gap. With this application in mind, photonic devices can be grouped into two major categories: i) direct sources, ii) laser-enabled systems [Mueller 06]. The first ones are devices able to emit radiation in the far-IR region, while the second ones are those employed in specific detection schemes, to generate the wanted frequency.
Main direct sources are gas lasers, optical parametric oscillators (OPO), and quantum cascade lasers (QCL). The gas laser, also known as optically pumped terahertz laser [Coherent], consists of a CO_2 laser exiting a gas cell that usually contains

small organic molecules, like methanol. It can emit high power, but it is also quite awkward, since it is difficult to control its cavity length, hence to guarantee stable emission wavelength. Another way of achieving laser emission in the FIR region is by optical parametric generation. As an example, an OPO employing a nonlinear crystal ($MgO:LiNbO_3$) inside the cavity of a Nd:YAG laser was recently reported [Edwards 06]. It can emit in the wavelength range of 100-250 μm, however its mean power is only 75 nW. Moreover, both gas lasers and parametric oscillators are very large and bulky systems. On the other hand, QCLs are compact semiconductor devices, that can be designed to emit in the FIR range, by tailoring the wafer structure. First demonstration of QCL lasing at 4.4 THz, in pulsed conditions, was reported by [Köhler 02]. Since then, thanks to improved fabrication, continuous-wave (CW) operation and higher output powers have been achieved [Williams 06]. The main advantage of QCLs are very narrow linewidth and good output power, however they have to be driven at low temperature. Another option that was proposed in the past is a very high frequency mode-locked laser [Yanson 02], based on harmonic mode-locking, which managed to achieve up to 2.1 THz. This is a very interesting source, however it has some major drawbacks in that it is not tunable, since the generated frequencies have to be multiple of the fundamental cavity frequency, and it presents extremely tight technological requirements.

More recently, quantum dot (QD) based mode-locked lasers have been proposed as high-frequency sources, as reported in [Renaudier 05], showing very narrow linewidth at 45 GHz. However, QD lasers are still in an early stage of research, where growth and basic lasing performance are still major issues which have to be looked at.

Among the so-called laser-enabled techniques, time-domain systems and photomixing are the most popular at present. In time-domain systems ultrafast optical pulses (typically in the femtosecond range) are detected by a low temperature grown photoconductor [Shen 04]. This method is also known as terahertz pulsed

technology [TeraView]. Since in this technique the pulse power is spread over a wide range of frequencies, although providing a broad range of frequencies, it causes low output powers ($< 1\ \mu$W). Moreover, detection sensitivity is restricted, due to the pulsed nature of the source, and spectral purity is limited, due to source laser jitter.

Another laser-enabled technique is the optical heterodyne technique, also known as photo-mixing. It is considered as the low-cost alternative to commercial technologies [Gregory 05], since pulsed technology, although generating signals with excellent properties, requires a very complex and bulky apparatus. This is the technique chosen for the present project, as it is the most commercially viable.

1.2.1 Photo-mixing

The heterodyne detection technique, i.e. photo-mixing, is based on a coherent detection scheme, where two CW optical modes (usually laser modes) are shone onto a photoconductive element. As a result, due to the quadratic response of the detector to the applied electric field, the photoconductor produces a photocurrent with a frequency equal to the frequency difference of the two modes. The result is also known as heterodyne mixing, or optical beating. This scheme can be described analytically using the formula:

$$i(t) = I_{01} + I_{02} + I_{12}\ cos[(\omega_1 - \omega_2)t + \phi_1 - \phi_2)] \tag{1.1}$$

where $i(t)$ is the generated photo-current, I_{0i} are the CW electrical signals generated by each separate mode, I_{12} is the beat signal, and ω_i and ϕ_i are the frequencies and phases of the optical signals [Siegman 86]. Note that all the sum-frequency terms have been neglected, since they cannot be detected. The I_{12} term is given by the overlap integral between the transversal distributions of the two modes U_i, and it is written as:

$$I_{12} = \int\int U_1^*(x,y)U_2(x,y)dxdy \tag{1.2}$$

In practice, the degree of spatial overlap between the two modes can be described using a parameter m, called the *spatial mixing efficiency*, which varies from 0 (no overlap) to 1 (complete overlap).

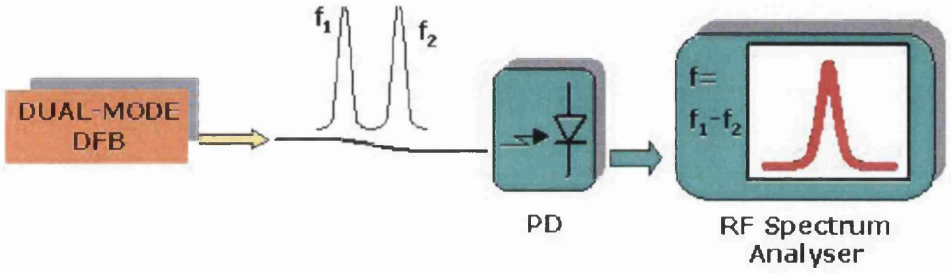

Figure 1.3: Schematic of the photo-mixing experiment, showing its principle of operation.

In the heterodyne scheme, when the incident optical fields are narrow-line with a stable frequency difference, then the photo-generated electrical signal is itself a clean, narrow-line sinusoid. The other main advantage of this technique is its wide range of tunability, which is limited only by devices used and by the bandwidth of the photoconductive element.

Although the scheme has been known for many years [Forrester 55], [Teich 68], its exploitation to generate signals in the THz range is more recent [McIntosh 95]. Since then, a large number of works about photo-mixing at GHz and THz frequencies have been reported, using different laser systems, from two separate lasers to dual-wavelength sources, and different detection schemes. A detailed review of the most interesting laser systems for heterodyne mixing is given in the next paragraph (1.3).

Apart from research on potential laser sources, extensive work into other aspects of photo-mixing has been carried out, to improve frequency response and performance, in terms of stability, noise and linewidth. Different detectors have been employed, such as low-temperature-grown GaAs (LTG-GaAs) [Hyodo 96], and fast

photodiodes (PD), like traveling-wave (TW-PD) [Stöhr 01] or unitraveling-carrier (UTC-PD) [Ito 04].

Ways of improving the quality of the generated signals have also been proposed and investigated, in particular for the case of two separate lasers, since the performance is limited by the phase noise of each source, which is converted to the mm-wave domain [McIntosh 95, Braun 98]. Improvements in performance were recorded by using the optical phase lock-loop technique (OPLL) [Ramos 92], [Langley 99], or the optical injection locking technique [Goldberg 83]. However, OPLL requires narrow linewidth lasers ($\ll$ MHz) and short loop propagation delay, which is a limitation to its feasibility, while relatively wide linewidth requires very short loop propagation delay ($\ll$ cm) in order to achieve acceptable phase noise reduction. On the other hand, optical injection locking can provide low phase-error variance, but its locking range is limited by stability considerations [Walton 98]. Introduction of an integrated technique, combining OPLL and OIL, called optical injection phase-lock loop (OIPLL) [Bordonalli 94], has proven to be a step forward in terms of performance. Another way to improve the stability of generated signals is by using an external modulation, as by adding a subharmonic sinusoidal modulation to the current injected into a dual-wavelength source [Grosskopf 00].

After reviewing the available technology and system options, the general conclusion is that best suited sources for photo-mixing are lasers that can simultaneously emit two different wavelengths [Tani 00].

1.3 Dual-wavelength laser sources

In recent years, photo-mixing using two modes emitted by the same laser source, the so-called dual-wavelength (or dual-mode, or two-color) lasers, has become increasingly popular [Tani 05] and these sources are today subject of extensive research [IPHOBAC]. Reported experiments employ a very wide range of sources, from solid-state and fiber-based lasers, to semiconductor devices.

Among solid-state lasers, dual-wavelength emission has been reported in a Nd:YVO_4 laser operating at two different transition levels [Chen 00], in a system consisting of two resonators and a common gain medium [Siebert 02], and in a more compact systems as a dual-mode microchip laser [Hyodo 96]. Dual-wavelength fiber ring lasers have also been used to generate microwave signals [Chen 06], showing the advantage of having only one gain medium, which reduces the modes relative fluctuations. However , both solid-state and fiber-base systems are complex and large sources.

A lot of effort has been made to exploit two-colour external-cavity (EC) laser systems, that consist of a laser diode coupled to an external mirror. Various examples can be found in the literature, such as devices using a biperiodic grating [Hidaka 91], a fixed optical grating [Hoffmann 04a], an external fiber-Bragg-grating [Wang 05b], or in a VECSEL (vertical external-cavity surface-emitting laser) configuration [Leinonen 05]. Nonetheless they are mechanically critical devices, not suitable as portable sources. Microfluidic dye lasers have also been investigated as potential dual-wavelength sources [Kou 06]. Again, they are complex and mechanically unstable sources.

The alternative to the above-mentioned systems is given by dual-mode monolithic devices. In fact, looking at reviews of laser sources for photo-mixing applications [Razavi 98, Tani 00, Matus 04], it appears that monolithic dual-wavelength lasers, DFBs and DBRs in particular, are the most suitable for this application, thanks to their spectral quality, stability, compactness and integrability.

1.3.1 Monolithic dual-wavelength lasers

The first reported dual-mode DBR laser is by [Iio 95], later the device was specifically employed in photo-mixing experiments [Gu 98]. In this case, two-colour emission is achieved by defining a phase-shifted grating, on an AlGaAs-GaAs ma-

terial. The reflection spectrum of the grating shows two reflection peaks, where the centre wavelength is selected by the grating period, while the spacing between the two peaks is determined by the phase shift section. The laser spectrum was assessed under different driving conditions, showing three regimes: single longitudinal mode operation at the shortest wavelength for low injection current, two longitudinal mode operation for medium injection current and single-mode operation at the longer wavelength for high injection current. The explanation is that the gain peak moves to longer wavelengths as the injected current is increased, while the peaks of the DBR section do not move. Two-mode operation occurs when the gain peak wavelength coincides with the centre wavelength of the Bragg peaks. More recently, Coleman reported a dual-wavelength InGaAs-GaAs DBR laser [Roh 00] based on a ridge-waveguide structure, comprising a gain section and two grating sections having different Bragg periods, hence the two-colour spectrum (Fig. 1.4). Tuning of one grating was achieved by injection current, showing a large

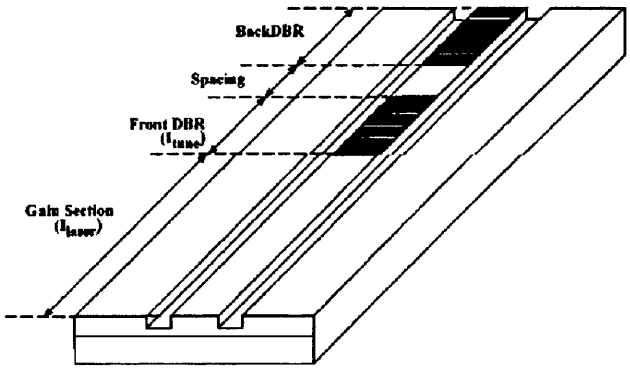

Figure 1.4: [Roh 00]: The two wavelengths are defined by two gratings with different periods.

shift between the two modes, up to 6.9 nm. Other lasers comprising two gratings

have been reported, for example in a Y-junction configuration, as in [Teng 00], where a quantum well (QW) intermixing technique is employed for fabrication, or in a more complex structure [ODaniel 06], where the two different gratings are one on the p-contact side and the other on the n-side. Presently the four-section DBR laser (gain, phase section, and two gratings) is the most appealing dual-wavelength source for photo-mixing applications, mainly due to its wide tuning range.
The most popular alternative to DBR lasers is the DFB laser, due to its reduced technological complexity. The first reported dual-wavelength integrated DFB laser is by Dutta [Dutta 86]. The device was fabricated by defining a second-order Bragg grating, using the re-growth technique, then defining two separate, although very close, ridge-waveguide structures. Dual-wave emission was demonstrated, aiming to applications in wavelength multiplexed optical systems. Another reported dual-wavelength DFB laser is a multisection long-cavity DFB laser [Lima 95]. The DFB structure was specially modified to obtain laser oscillation on both sides of the stop-band, the mode spacing was adjusted to the desired frequency by specifically designing the coupling coefficient. Two modes around 1.55 μm, with 60 GHz spacing, were detected, and by tuning the bias current the mode spacing could be adjusted to 40 GHz. Two-section DFBs were also used as microwave sources [Wang 99], and more recently a dual-wavelength InGaAsPInP multi-section (MS) DFB laser was reported by Sartorius [Möhrle 01]. This structure comprises three sections: two single-mode DFBs, having different Bragg periods, and a phase section in between them, for wavelength tuning (Fig. 1.5). This laser is also called self-pulsating (SP) DFB laser, since the amplitude superposition of the two CW single modes produces a beating type self pulsation (SP).

Other types of two-colour monolithic lasers are a vertical cavity surface emitting lasers (VCSEL) and dual-QCLs. Pellandini reported on a dual-wavelength VCSEL comprising two cavities, placed one on top of the other, and coupled through a common mirror [Pellandini 97]. The main limitation for such structures is that they are not integrable with other optoelectronics device, such as semiconductor

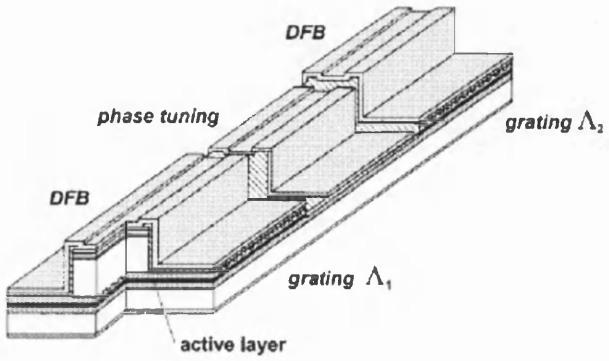

Figure 1.5: Three section DFB: two active ones, having different periods, and a phase adjustment section [Möhrle 01].

optical amplifiers (SOA) or photodiodes (PD). A dual-mode interband cascade laser incorporating two active regions was demonstrated in [Garcia 97], and recently in [Yan 06].

Double core devices have also been reported, either using a stacked active layer (SAL) technique [Beernink 94], or with a more simple regrowth [Uchida 05].

Another interesting integrated device that is able to emit simultaneously two longitudinal modes was proposed very recently by [Wilk 07]. It is a waveguide laser with a 7.5 μm wide ridge, designed on purpose for guiding two transversal modes, as shown in Fig. 1.6. Since the two modes have slightly different propagation constants, their operating wavelength is also slightly different, hence the possibility to generate a frequency difference signal. This laser is very appealing due to its conceptual and technological simplicity, moreover it takes advantage of the common cavity for increased stability. However, since the two modes have a limited spatial overlap around 50%, this source is not optimum in terms of photo-mixing efficiency.

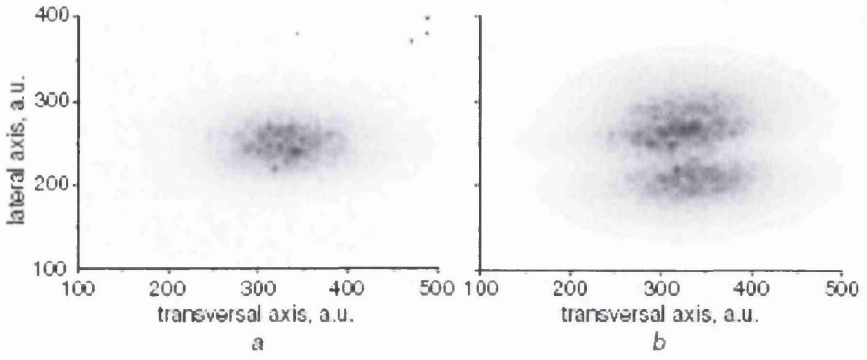

Figure 1.6: Far-field profiles of the dual-mode laser by [Wilk 07], (a) at 100 mA, (b) at 400 mA.

1.3.2 Some applications of dual-wavelength lasers

Dual-wavelength lasers have other applications besides photo-mixing. Among them, a significant effort is put into researching new dual-wavelength monolithic lasers for optical data storage and processing, as several recent papers on the subject testify [Tojo 05], [Uchida 05]. These devices look very appealing because they comply with the requirements of robust, compact and low-cost sources, that are essential in the field of optical recording systems.

Dual-mode lasers find also applications in optical remote sensing, for instance in differential absorption lidar (DIAL) [Yu 97] and two-wavelength interferometry [Gurov 99].

Finally, one of the most consolidated applications for monolithic multiwavelength

laser diodes is for wavelength division multiplexing (WDM), in communication systems.

1.4 Distributed reflector lasers defined with lateral gratings

There are two main ways of creating gratings on distributed feedback lasers : i) by defining them during the growth process, which is known as "re-growth" technique, ii) by post-growth fabrication, that is by etching surface gratings. In the re-growth technique the grating is defined by etching it very close to the active region, then filling it, by standard growth techniques, with a material having a different refractive index. On the other hand surface gratings, sometimes reported as shallow, or index-guided, gratings, are defined by etching into the upper cladding, hence causing a periodic variation of the refractive index of the guiding structure. The advantage of the first approach is a strong interaction of the mode with the grating, while the second one is technologically more simple and flexible. Since the purpose of this project is to show the feasibility of the integrated dual-wavelength laser, it was chosen to use surface gratings. Among the possible approaches to define surface gratings, a very convenient way is to periodically vary the width of the waveguide. In the literature, this type of structure has been named in a variety of ways, the most used being lateral grating [Miller 91] and laterally coupled [Tiberio 94], sidewall grating [Wong 93], and vertical grating [Wiedmann 01].
First demonstration of a laser incorporating this structure was given by Miller in 1991 [Miller 91]. They showed laser operation of a lateral grating DFB fabricated on InGaAs-AlGaAs material, under pulsed conditions. Fig. 1.7 depicts Miller's device.
The same type of structure was later fabricated on GaAs-AlGaAs material, by Abe [Abe 95], in 1995. Single-mode operation under CW conditions was also demon-

strated [Yee 99].

Subsequently this type of structure has been widely exploited, in various optical integrated circuits (OIC). Arrayed structures for instance were fabricated [Miller 91] for high-power applications, while Kim [Kim 03] fabricated a new structure called "distributed reflector", that integrates a lateral DFB laser with a lateral DBR reflector.

Recently, it was shown that accurate design of the ridge-waveguide, along with high-quality dry-etching, can lead to very good lasing performance [Wang 05a].

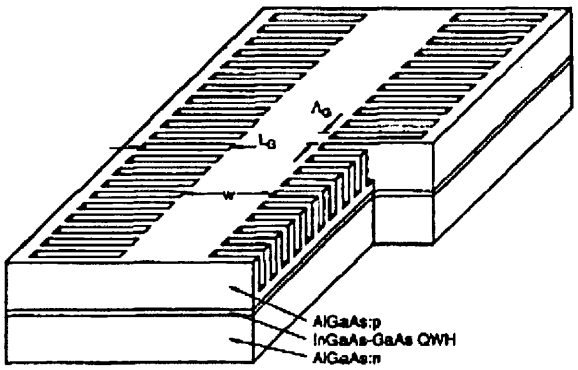

Figure 1.7: Schematic diagram of the lateral DFB RWG laser reported by [Miller 91].

Wang showed low threshold and a very high SMSR of about 45 dB from a standard lateral grating DFB laser fabricated on InAlGaAs-InP material.

A slightly different type of lateral grating was fabricated by defining metal gratings alongside the laser ridge wave-guide [Kamp 99]. In this case the grating acts as a periodic absorber for the evanescent part of the propagating mode, hence causing complex coupling. In the literature, the shallow gratings, that are etched into the upper cladding, are referred to as index-coupled DFBs, while the gratings

etched into the active region, or into a loss providing layer, are called gain-, loss- or complex-coupled DFBs.

A further development on the field of laterally complex-coupled gratings is the introduction of a focussed ion beam (FIB) technique [Rennon 01], to define complex-coupled DFB laser, without need for post-growth.

Another example of lateral grating laser, which shows the strong potential of this technology as a platform for monolithic integration, was recently reported in [Strain 06]. In this work the lateral grating was designed in order to introduce a chirp in the optical signal, to compensate for the chirp typically generated by mode-locked lasers.

A device similar to the lateral grating laser is the photonic wire (PhW) Bragg grating [Gnan 06]. This structure differs from lateral gratings in its size, which is much smaller (ridge-widths are around a few hundred nanometres), and hence it induces a stronger perturbation over the mode, which can no longer be assumed unchanged along the direction of propagation. It follows that approximate analytical approaches, such as the coupled-mode solutions or the transfer matrix method, do not hold for such structures, and more complex numerical techniques, such as the Floquet-Bloch expansion, are required.

1.5 Conclusions

Today the generation of signals in the far-IR range is a very active topic of research, due to its many applications in key areas of research, such as astronomy, medicine and security. After a thorough review of potential sources, photonic techniques appear to be very promising candidates. In particular the optical heterodyne technique is the most appealing approach to achieve tunable THz sources, due to its wide range of frequencies. From a review of potential sources for photomixing, dual-wavelength monolithic devices appear to be best suited, due to low power consumption and low production cost, and above all due to their common

cavity, which allows generation of very stable beat signals (section 3.4.1). Finally, a review of the lateral grating structure, which was chosen as building block of the Bragg reflector lasers, was given showing its potential in the integration of different functionalities on the same chip, without need for material re-growth.

Chapter 2

Theory of Bragg reflector lasers

The most common way to achieve single-mode operation in semiconductor lasers is by using a grating structure, either in a passive (DBR) or active (DFB) configuration. These types of devices, which have been developed since 1971 [Kogelnik 71], still today are subject of extensive research as fundamental elements in optical integrated circuits.
In this Chapter the analysis of Bragg grating lasers is addressed, alongside some characteristic features and effects, which are useful to the understanding of the experimental results.

2.1 Coupled-wave equations

Distributed Bragg reflectors are optical guiding structures in which a periodic perturbation of the refractive index along the cavity length causes coupling between forward and backward propagating waves. This effect, known as *backward Bragg scattering*, from the name of the scientist who first discovered it [Bragg 13], produces coherent coupling between EM fields that propagate with wavelengths satisfying the Bragg condition [Agrawal 93]:

$$\Lambda = \frac{m\lambda_B}{2n_{eff}} \tag{2.1}$$

where Λ is the grating period, λ_B is the wavelength of light propagating within the structure (Bragg wavelength), n_{eff} is the effective refractive index of the mode, and m is the grating order. Due to this effect, the Bragg reflector substantially behaves as a wavelength dependent mirror.

The effect over the fields involved can be described starting from the general wave equation (Helmholtz equation):

$$\frac{d^2E}{dz^2} + n(z){k_0}^2E = 0 \tag{2.2}$$

where the field E is given by the sum of the forward and backward propagating waves, and $n(z)$ is the axially varying refractive index, and k_0 is the wavenumber $2\pi/\lambda_B$. Starting from a general solution of the form:

$$E(x,y,z) = U(x,y)[E_{FW}exp(j\beta z) + E_{BW}exp(-j\beta z)] \tag{2.3}$$

where the x- and y-axis define the plane perpendicular to the z direction of propagation of light, $U(x,y)$ is the transversal field distribution of the mode, and β is the mode propagation constant, by substituting the expressions for E, k_0, and $n(z) = n_{eff} + \Delta n(z)$, in Eq. 2.2, after neglecting second order derivatives, one obtains a set of equations that relate the counter-propagating waves:

$$\frac{dE_{FW}}{dz} + j\Delta\beta E_{FW} = -j\kappa E_{BW} \tag{2.4}$$

$$\frac{dE_{BW}}{dz} - j\Delta\beta E_{BW} = j\kappa E_{FW} \tag{2.5}$$

Eqs. 2.4-2.5 are known as *coupled-wave equations*. Here $\Delta\beta$ is the detuning between β and β_0, while κ is a parameter called *coupling coefficient*, that accounts for the coupling between the two fields (it is usually reported in cm^{-1}). The most general definition for κ can be derived from the coupled-wave theory, and it results:

$$\kappa = \frac{k_0^2}{2n_{eff}} \frac{\iint_{grating} \Delta\epsilon(x,y)U^2(x,y)dxdy}{\iint_{\infty} U^2(x,y)dxdy} \tag{2.6}$$

where $\Delta\epsilon$ is the dielectric perturbation. κ basically measures the strength of the interaction between the propagating field and the perturbation on the material

caused by the presence of the grating.

General solutions to the coupled-wave equations are of the form [Buus 05]:

$$E_{FW}(z) = \left[\cosh(\gamma z) - \frac{j\Delta\beta}{\gamma}\sinh(\gamma z)\right]E_{FW}(0) - \frac{j\kappa}{\gamma}\sinh(\gamma z)E_{BW}(0) \quad (2.7)$$

$$E_{BW}(z) = \frac{j\kappa}{\gamma}\sinh(\gamma z)E_{FW}(0) + \left[\cosh(\gamma z) + \frac{j\Delta\beta}{\gamma}\sinh(\gamma z)\right]E_{BW}(0) \quad (2.8)$$

with γ defined as $\gamma^2 = \kappa^2 - \Delta\beta^2$. The coupled-wave theory here presented, despite giving accurate predictions, is based on a few approximations, and a more rigorous analysis can be carried out using the Green function [Buus 05]. Interestingly however, this approach, which is in principle more accurate, gives the same results as the coupled mode theory.

The solutions given in 2.7-2.8) can be re-written in matrix form as:

$$\begin{bmatrix} E_{FW}(z) \\ E_{BW}(z) \end{bmatrix} = M(z) \begin{bmatrix} E_{FW}(0) \\ E_{BW}(0) \end{bmatrix} \quad (2.9)$$

where $M(z)$ is:

$$M(z) = \begin{pmatrix} \cosh(\gamma z) - \frac{j\Delta\beta}{\gamma}\sinh(\gamma z) & -\frac{j\kappa}{\gamma}\sinh(\gamma z) \\ \frac{j\kappa}{\gamma}\sinh(\gamma z) & \cosh(\gamma z) + \frac{j\Delta\beta}{\gamma}\sinh(\gamma z) \end{pmatrix} \quad (2.10)$$

In the literature, Bragg laser analysis is sometimes reported as transfer matrix theory. As mentioned above, Eq. 2.9 is simply a re-formulation of the coupled mode theory which makes use of matrix formalism, that proves to be a very powerful tool, by allowing direct analytical solution to the coupled mode equations [Carroll 98].

2.2 DBR lasers

DBR lasers are edge-emitting lasers in which at least one of the two facets is replaced by a Bragg reflector. In this case the grating structure is passive, i.e. it does not provide any optical gain. The behaviour of a DBR grating as a wavelength

dependent reflector is conveniently described by its power reflectivity $R(\lambda)$, that is given by [Buus 05]:

$$R(\lambda) = \frac{\kappa^2 \sinh^2(\gamma L_{DBR})}{\Delta\beta^2 \sinh^2(\gamma L_{DBR}) + \gamma^2 \cosh^2(\gamma L_{DBR})} \tag{2.11}$$

It is interesting to investigate how the coupling coefficient κ and the reflector length L_{DBR} can affect the performance of the Bragg grating. Fig. 2.1(top) shows the power reflectivity R versus λ at a fixed κ, for different grating lengths, while Fig. 2.1(bottom) shows $R(\lambda)$ for different coupling coefficients, for a fixed grating length.

It appears that R increases when both κ or L_{DBR} increase, however the reflectivity width (also known as *stop-band width*) is affected in a different way, since for higher κ it broadens, while for longer gratings it reduces.
Note that for a wavelength $\lambda = \lambda_B$ the power reflectivity reduces to:

$$R = \tanh^2(\kappa L_{DBR}) \tag{2.12}$$

showing that the magnitude of reflection at the peak wavelength λ_B is determined only by the κL_{DBR} product, also known as the normalised coupling coefficient. From this relation it is clear that the coupling coefficient measures the strength of reflection per unit length. The curve describing the peak power reflectivity $R(\lambda_B)$ as a function of κL_{DBR} is shown in Fig. 2.2.

From Eq. 2.11 it is readily found that (for $\Delta\beta L_{DBR} > \kappa L_{DBR}$) the first zeros of R are at:

$$\Delta\beta L_{DBR} = \sqrt{(\kappa L_{DBR})^2 + (\pi)^2} \tag{2.13}$$

A useful tool in treating a DBR laser structure is to approximate it with a Fabry-Perot (FP) cavity [Yee 95]. In fact, a DBR laser with reflector length L_{DBR} and gain section length L_A can be analysed as an equivalent FP laser whose length is given by $L_A + L_{eff}$, where L_{eff} is the effective length of the Bragg grating, defined as:

$$2L_{eff} = \frac{d\phi}{d\beta} \tag{2.14}$$

where ϕ is the phase shift of the DBR section. For $\lambda = \lambda_B$, L_{eff} becomes:

$$L_{eff} = \frac{tanh(\kappa L_{DBR})}{2\ \kappa} \tag{2.15}$$

From Eq. 2.15 it results that L_{eff} approaches L_{DBR} for small values of κ,

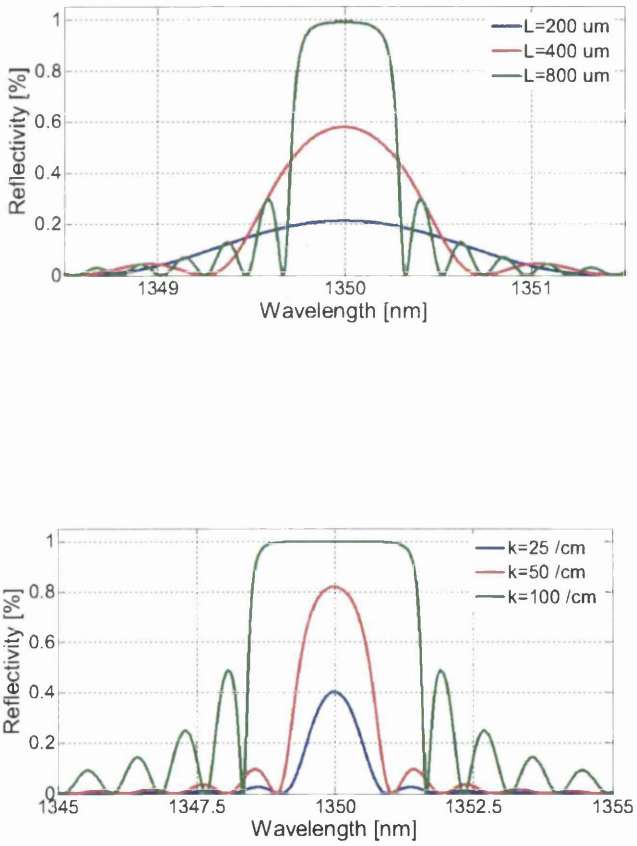

Figure 2.1: Simulations of the spectral response of a generic passive Bragg reflector, having length L_{DBR} and coupling coefficient κ. Power reflectivity vs. wavelength, for a grating with $\kappa = 25\ cm^{-1}$, and different lengths $L_{DBR} = (200, 400, 800)\mu m$ (top); for L_{DBR}= 300 μm and different $\kappa = (25, 50, 100)\ cm^{-1}$ (bottom).

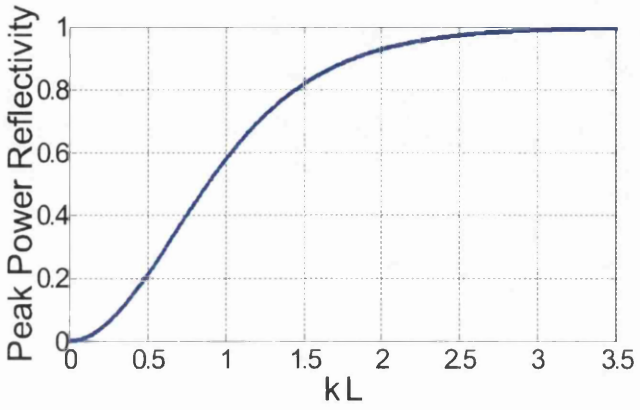

Figure 2.2: Power reflectivity of a distributed Bragg reflector at λ_B, as a function of κL.

while for high κ it decreases. In this view, the Bragg reflector can be seen as a wavelength selective mirror which overlaps the frequency comb of longitudinal modes created by the FP cavity, hence leading to single-mode operation.

2.2.1 Another approach to the DBR analysis

Another, more simple, approach which can be used to model Bragg reflectors is the multi-reflection layers analysis. This approach, which is accurate for deep-etched and microstructured mirrors, treats the grating structure as a stack of reflective layers, using the Fresnel formula for plane waves $r = \Delta n/2n_{eff}$ [Buus 05]. More precisely, following the Macleod analysis [Erwin 07], it can be shown that the stack reflectivity can be defined as:

$$R = \left(\frac{1-Y}{1+Y}\right)\left(\overline{\frac{1-Y}{1+Y}}\right) \tag{2.16}$$

where Y is the optical admittance C/B, and the terms B and C are derived from the characteristic matrix for the multi-layer system:

$$\begin{bmatrix} B \\ C \end{bmatrix} = \left(\prod_{r=1}^{q} \begin{bmatrix} cos\delta_r & jsin(\delta_r/n_r) \\ jn_r sin(\delta_r) & cos\delta_r \end{bmatrix} \right) \begin{bmatrix} 1 \\ \overline{n_m} \end{bmatrix} \tag{2.17}$$

where n_r is the refractive index of the r-th layer, n_m is the refractive index of the substrate, δ_r is defined as $\frac{2\pi}{\lambda} n_r d_r = k d_{opt}$, and d_r is the thickness of the layer.

2.3 DFB lasers

A DFB (distributed feedback laser) is a laser source in which the effects of Bragg grating reflections and optical amplification are combined, hence its name.

For the case of a structure with non-reflecting mirrors, since the laser consists essentially of an active periodic structure, its analysis can be carried out from the 2.4-2.5 taking into account the gain by replacing $\Delta\beta$ with $\Delta\beta + j\ g_0$, where g_0 is the field gain. The oscillation condition is then found by taking into account the boundary conditions for the system. It is important to notice that this device differs substantially from usual laser cavities, where the boundary conditions for the internal waves are determined by outcoming waves, incident onto the mirrors [Kogelnik 72]. Since the distributed feedback structure is a self-oscillating system, the internal waves start from zero amplitude at the boundaries, receiving their energy via scattering from the counter-propagating wave. From this observation, the boundary conditions $E_{FW}(0) = E_{BW}(L) = 0$ follow. Re-writing Eq. 2.9 for the case $z = L$:

$$E_{FW}(L) = M_{11}(L)E_{FW}(0) + M_{12}(L)E_{BW}(0) \tag{2.18}$$

$$E_{BW}(L) = M_{21}(L)E_{FW}(0) + M_{22}(L)E_{BW}(0) \tag{2.19}$$

it is found that the boundaries conditions require the M_{22} term to be set to zero, hence leading to the expression:

$$\cosh(\gamma L) + \frac{j(\Delta\beta + j\ g_0)}{\gamma} \sinh(\gamma L) = 0 \tag{2.20}$$

which is known as the *oscillation condition* (see A7.10) for the ideal DFB laser. The γ coefficient that appears in the previous equation is:

$$\gamma^2 = \kappa^2 - (\Delta\beta + j\ g_0)^2 \tag{2.21}$$

The oscillation condition can be re-written as:

$$\gamma L \coth(\gamma L) = -j(\Delta\beta L + j\ g_0 L) \tag{2.22}$$

From this condition it results that for any given set of values κ and L there is only a discrete number of allowed solutions, in the form of $(\Delta\beta, g_0)$ eigenmodes. This is due to the fact that, in contrast to FP and DBR lasers, gain and phase are linked through the complex number $\Delta\beta + j\ g_0$. In general, solutions to Eq. 2.22 have to be calculated numerically, however for the case of $\kappa L >> 1$ there is an asymptotic solution for the mode with the lowest required gain. Results from numerical calculations carried out at different κL values are shown in Fig. 2.3.

From this plot it can be noticed that the mode having the lowest required gain (first lasing mode) is not at the Bragg wavelength, as for DBR lasers. Moreover, the degeneracy effect creates a pair of first lasing modes symmetrically located across the Bragg wavelength.

A characteristic parameter highlighted from this analysis is the distance between the two first degenerate modes Δ_S, called *stop-band width*. It depends only on the κL product and, for the case of an ideal DFB laser with non-reflecting facets, it has to be calculated numerically. However, for high κL values Δ_S is well approximated by $2\kappa L$. It can be shown that $2\sqrt{(\kappa L)^2 + (\pi)^2}$, previously derived for passive structures (Eq. 2.13), can be used as a very good approximation for calculating the stop-band width of DFB lasers. As κL decreases the normalised mode spacing approaches π, which is the same as for a Fabry-Perot laser of length L. Fig. 2.4 shows a comparison between the numerical solution for a DFB laser, the asymptotic solution $2\kappa L$, and the exact solution for a DBR laser.

The simplest way to remove the DFB mode-degeneracy is by introducing a cleaved facet, in order to lift the symmetry of the structure. This can be accounted

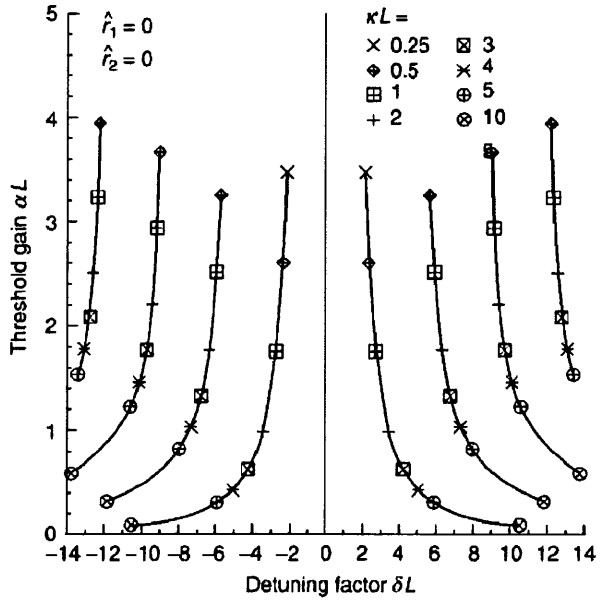

Figure 2.3: Amplitude threshold gain αL (i.e. $g_0 L$) vs. detuning δL (i.e. $\Delta\beta L$) for a mirrorless index-coupled DFB, for different values of the κL product, from [Shiraz 96].

for in Eq. 2.22 by introducing the facet complex reflectivity $re^{j\theta}$:

$$\gamma \cosh(\gamma L) + [j(\Delta\beta + jg_0) + j\kappa r e^{-2j\theta}] \sinh \gamma L = 0 \tag{2.23}$$

where θ is the phase angle due to the fraction of period left close to the cleaved facet. Since in practice it is not possible to control the facet cleaving position within the grating period (for first order gratings this is around 200-250 nm), the phase shift introduced by the facet has to be treated as a statistical variable. A numerical solution of Eq. 2.23, for different values of κL, is shown in Fig. 2.5. From this result it is clear that the mode-degeneracy previously shown has been lifted, leading to single-mode behaviour.

Another way to ensure single-mode operation in DFB lasers is, for instance, the introduction of a $\lambda/4$ phase shift at the centre of the structure [Buus 05].

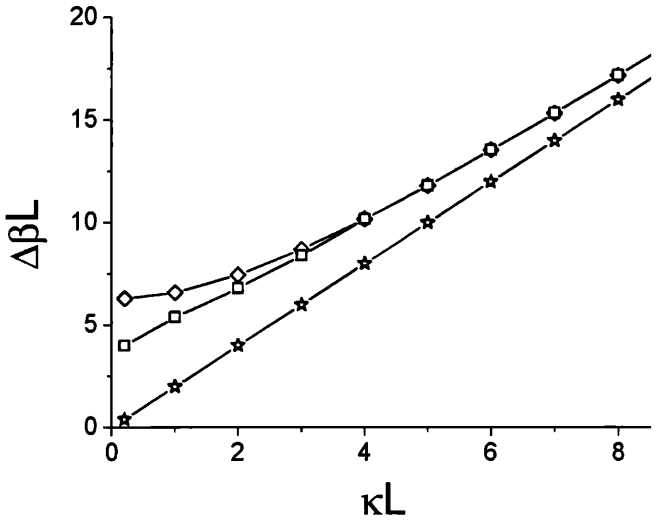

Figure 2.4: Normalised stop-band width vs. κL product, for an ideal DFB laser with non-reflecting facets: ($\square$) numerical solution, ($\star$) approximation for high κL values, ($\diamond$) approximation for low κL values.

2.4 Wavelength tuning mechanisms

In the case of DBR and DFB lasers, tuning of the emission wavelength is achieved by tuning of the Bragg wavelength. From the Bragg condition 2.1 it is clear that the only parameter which can be varied is the effective refractive index of the grating structure. This can be changed by varying the operational temperature of the device or, in the case of DBR lasers, by carrier injection into the grating section.

2.4.1 Thermal Tuning

Temperature changes in semiconductor lasers affect the emission wavelength either by changing the gain peak wavelength or by varying the refractive index of the grating structure, giving increased operation wavelengths at increased temperature

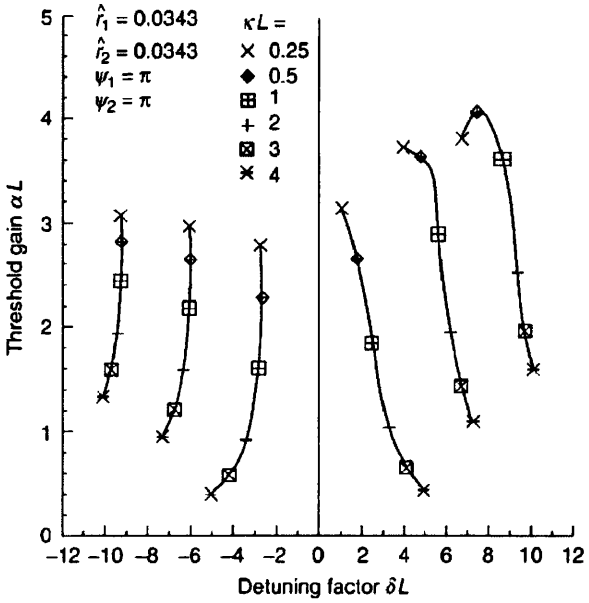

Figure 2.5: Amplitude threshold gain αL vs. detuning δL for a DFB with finite reflectivities, for different values of the κL product, from [Shiraz 96]

levels. Standard Fabry-Perot lasers show the same temperature dependence as the gain peak, with a tuning efficiency around 0.5 nm/°C, while for DBR and DFB lasers the lasing mode is function of the refractive index only, giving a tuning of 0.1 nm/°C[Buus 05]. This translates in a very fine control over the emission wavelength for single-mode lasers. On the other hand, this also means that when the plasma effect is used as a tuning mechanism, the thermal effect due to heating of the device tends to compensate the refractive index decrease caused by carrier injection.

2.4.2 Tuning by current injection

The refractive index in semiconductors can be varied by changing the carrier concentration, that is by current injection. There are three main effects which affect

the refractive index: i) free-carrier absorption, or plasma effect, ii) bandfilling, and iii) bandgap shrinkage [Bennett 90] (see Fig. 2.6). Free-carrier absorption is an intraband effect, given by absorption of a photon by a carrier, which can move to a higher energy level within the same band. It gives a decrease of the refractive index.

Bandfilling results in a blue-shift of the absorption peak, due to electrons filling the lowest energy states, hence electrons from the valence band (VB) require energies greater than the bandgap to be optically excited to the conduction band (CB).

Bandgap shrinkage occurs when the electron concentration is large enough for the electrons to behave as a gas of interacting, repelling, particles. This yields to a lowering of the CB edge. This effect tends to produce an increase in refractive index.

However, what is most important for tuning applications is the global effect caused by the combination of the three effects. It was shown, from both theoretical and experimental works, that at injection levels below 10^{18} cm^{-3}, and wavelengths around the bandgap, the result is a negative variation of the refractive index.

2.4.3 Phase tuning section

In DBR lasers, in order to improve their tuning performance, a more advanced structure, known as three-section DBR laser, is usually chosen [Coldren 95]. It is basically a DBR laser that includes an additional passive section, located between the gain and the grating section (Fig. 2.7). This additional section allows to introduce a small change of the refractive index, by carrier injection, which translates into a variation of the cavity length. This causes a very small shift of the comb of cavity frequencies, thus it allows for a very "smooth" wavelength tuning. This section is generally called *phase section*, since it allows for an independent control of the phase.

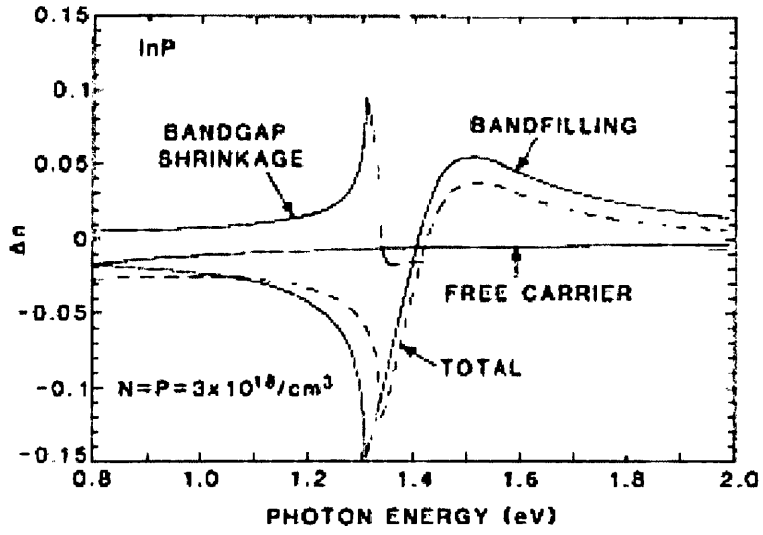

Figure 2.6: Change of the index of refraction due to carrier injection, in InP material, from [Bennett 90]. The overall response generated by the three different effects is shown.

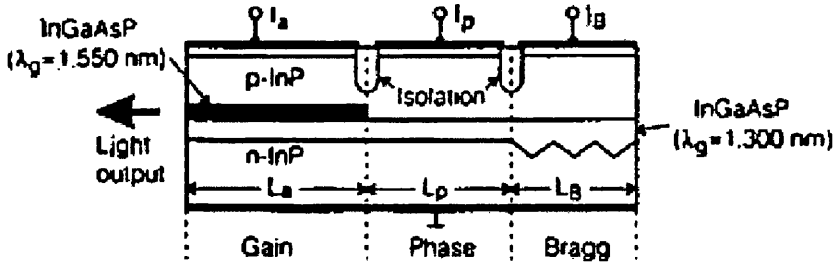

Figure 2.7: Typical three-section DBR laser, from [Coldren 00].

2.5 Spectral linewidth

Laser light is, by definition, produced through a process known as *stimulated emission*, which generates photons having all the same energy and phase, so that they

add up coherently. However, in a real laser source, light is also generated by spontaneous emission (SE), which creates photons having random phases, causing real devices to have a finite linewidth. Since spontaneous emission is a random process, laser linewidth analysis has to follow a statistical approach. Assuming that the phase distribution of SE photons follows a Gaussian distribution, which is correct for a large number of photons, it follows that the laser lineshape has a Lorentzian shape [Buus 05]. From statistical analysis, it can be shown that the laser linewidth $\Delta\nu$ is given by:

$$\Delta\nu_{ST} = \frac{h\nu v_g^2(\alpha_i + \alpha_m)\alpha_m n_{sp}}{8\pi P} \tag{2.24}$$

which is known as the Shawlow-Townes law. Here $h\nu$ is the photon energy, v_g is the group velocity, α_i are the internal loss, α_m are the end loss (or mirror loss, see A7.3), n_{sp} is the spontaneous emission coefficient, and P is the optical power per end, which can be written as:

$$P = \frac{v_g\ \alpha_m \overline{S} V_a h\nu}{2\Gamma} \tag{2.25}$$

where $\overline{S}$ is the averaged photon density, V_a is the volume of the active region and Γ is the confinement factor of the mode.

Eq. 2.24 defines the quantum limit for the laser linewidth, i.e. it gives the narrowest possible linewidth. However, for diode lasers a significant correction factor has to be added to the previous formula, to account for carrier density changes. Eq. 2.24 then becomes:

$$\Delta\nu_{STH} = \frac{h\nu v_g^2(\alpha_i + \alpha_m)\alpha_m n_{sp}}{8\pi P}(1 + \alpha_H^2) \tag{2.26}$$

which is labelled as the Shawlow-Townes-Henry law, from the name of the scientist who introduced the correction factor α_H [Henry 82]. The α factor, also known as the *linewidth enhancement* factor, is defined as:

$$\alpha_H = -\frac{\partial n'/\partial N}{\partial n''/\partial N} \tag{2.27}$$

where $\partial n'/\partial N$ and $\partial n''/\partial N$ are respectively the rate of change of the real and of the imaginary part of the refractive index with respect to carrier density. This factor accounts for the link between optical gain g and refractive index n, and hence phase (see (3.4)). The effect of α_H is to increase the minimum linewidth by coupling gain fluctuations to refractive index fluctuations, thus to the emitted wavelength via changes of the effective length of the cavity. As an example, every spontaneous event changes the population inversion and thus changes the refractive index, so if for instance n changes g fluctuates, causing frequency noise. Note also that due to (2.27), and to dispersion in semiconductors, α_H results in being wavelength dependent. This can be usefully exploited in DFB lasers, where the Bragg wavelength can be detuned from the gain peak, using negative detuning to have a lower value of α_H.

The narrowest linewidth reported to date for a DFB laser is 3.6 kHz, by Okai [Okai 93]. It was achieved by using a material with low α_i, high κL, which gives low α_m, and a distributed phase shift, to reduce spatial hole burning, hence allowing single-mode operation at high power levels. While for DBR lasers the lowest reported up to date is 25 kHz [Lammert 97].

2.6 Optical injection locking

Optical injection is a technique consisting in seeding a laser (slave) with a signal coming from a second source (master). If the frequencies of the two lasers are sufficiently close, the slave is "forced" to oscillate at master frequency, hence locking takes place. Injection locking phenomena can be described by taking a very general approach, which applies to any systems consisting of two coupled oscillators. The locking relation between the two oscillator is given by the Adler's equation [Annovazzi-Lodi 98]:

$$\Delta\omega = \frac{K/\tau_{in}}{e_S + 1}(\alpha_H \cos\phi_S - \sin\phi_S) \tag{2.28}$$

where $\Delta\omega$ is the frequency detuning, K is the relative amplitude of the injected field, τ_{in} is the cavity round trip, α_H is the linewidth enhancement factor, and e_S and ϕ_S are the stationary solutions of the system. From this formula it results that locking takes place within a certain range of frequencies $\Delta\omega$, known as locking range, and this $\Delta\omega$ is a function of the injection strength, so that as the intensity increases $\Delta\omega$ widens. Another frequency range is also defined, the pre-locking range, in which a phenomenon called frequency pulling takes place. These different zones of injection can be seen in Fig. 2.8. Note that at high levels of injection more complex behaviours can be seen.

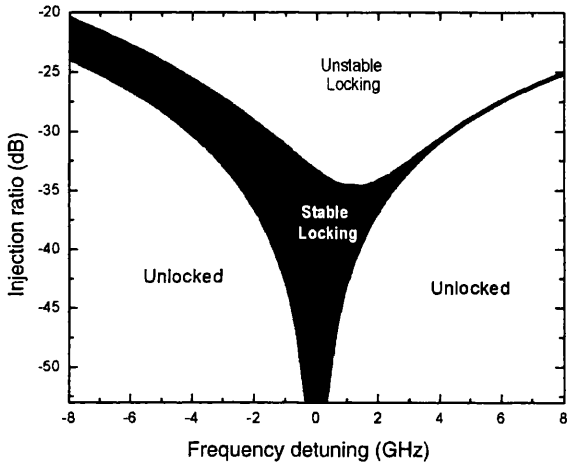

Figure 2.8: A typical map of locking range as a function of frequency detuning and injected power, from [Fukushima 03].

2.7 Conclusions

This Chapter is intended to help understanding the laser modelling described in Chapter 3, the technological choices made in Chapter 4, and the analysis of the experimental data reported in Chapter 5 and Chapter 6. The coupled-mode

theory, that describes the behaviour of Bragg grating lasers, was presented. The key parameters Bragg wavelength λ_B, coupling coefficient κ, and stop-band width Δ_S were introduced. The effect of mode degeneracy, which is typical of DFB lasers, was discussed; fundamental formulae were described for future reference. The effects of wavelength tuning and finite laser linewidth, which are relevant to distributed reflector lasers, were described. The phenomenon of optical injection locking, which was exploited in the experimental work on dual-wavelength lasers (Chapter 6), was introduced.

Chapter 3

Modelling of the Bragg lasers

In this research single-mode DBR and DFB lasers were developed, along with a novel dual-wavelength device, based on a lateral grating structure. This Chapter illustrates the work carried out in order to design the reported devices.

3.1 Modelling of the ridge-waveguide structure

The waveguide was modelled using a commercial mode finder software called FIMMWAVE [Photon Design], based on a fully vectorial approach. In these calculations in particular the FIMMWAVE FMM Solver was used, which is a fully vectorial solver based on the mode matching method, optimised for rectangular geometry waveguides like epitaxial structures.

Simulations were run searching for both transverse electric (TE) and transverse magnetic (TM) fields, within a six quantum well Al-quaternary material (section 4.1). The aim was to optimise the ridge-waveguide (RWG) structure in order to ensure single transversal mode operation. Results showed no TM guiding, which is what expected in this type of ridge-waveguide structures. The ridge waveguide width was determined by choosing the optimum trade-off between single-mode operation and technological limits, which proved to be a 2.5 μm wide ridge structure, while to achieve single-mode operation the depth was chosen to be around 1.7 μm

(Fig. 3.1).

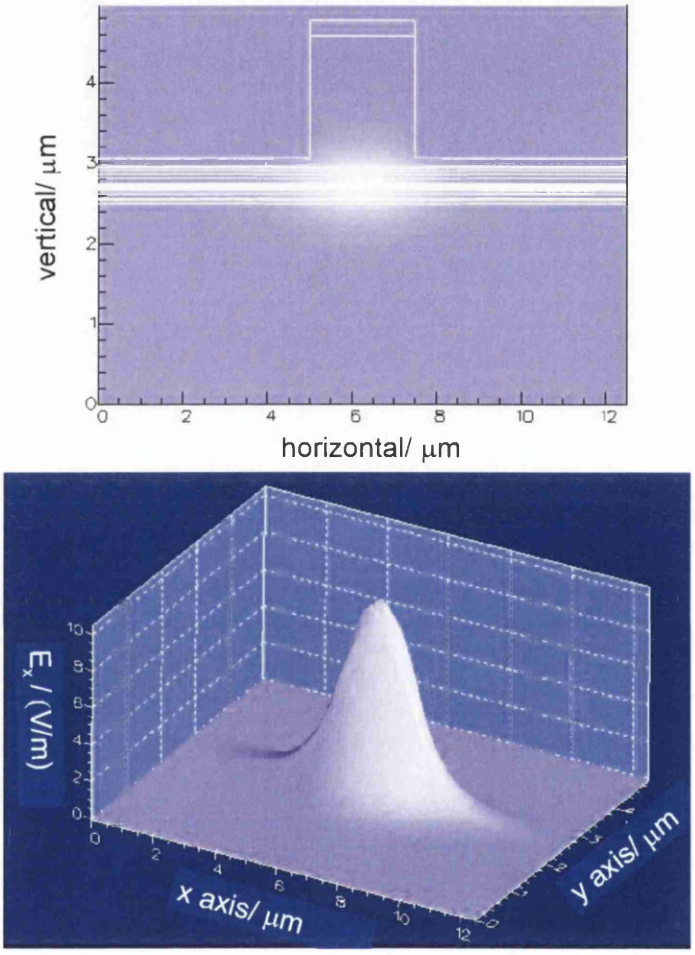

Figure 3.1: Simulated plots of mode propagation in the optimum ridge-waveguide structure: transversal section (top), and 3D distribution (bottom).

3.2 Modelling of the lateral grating

Modelling of the lateral grating structure was carried out starting from the general expression for the coupling coefficient (Eq. 2.6). Firstly, the geometry of the

grating was chosen to be rectangular, for simplicity of design and fabrication.

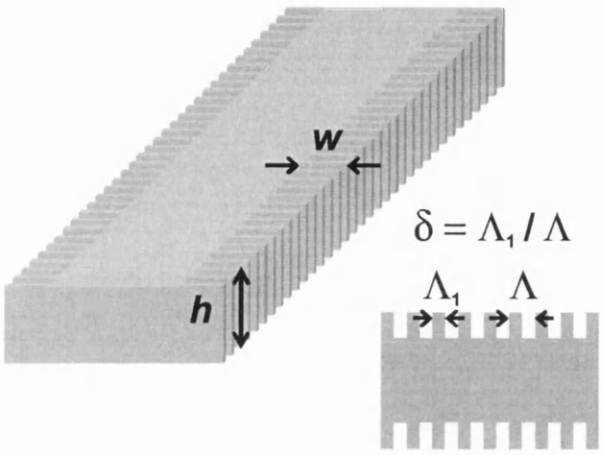

Figure 3.2: Schematic of the lateral Bragg grating, showing the design parameters δ (aspect ratio), h (etch-depth), and w (grating recess).

In this case the expression for κ reduces to [Agrawal 93]:

$$\kappa = \frac{sin(\pi m\delta)}{m}\Gamma_g \frac{{n_1}^2 - {n_2}^2}{\lambda_B n_{eff}} \tag{3.1}$$

where n_1 and n_2 are the refractive indexes of the semiconductor and of the dielectric layer respectively, n_{eff} is the effective refractive index of the guided mode, and δ is the duty cycle, or aspect ratio (see Fig. 3.2), of the grating. The parameter Γ_g, which in general represents a confinement factor, in this case represents the fraction of mode energy confined within the grating region. It is defined as:

$$\Gamma_g = \frac{\iint_{grating} E^2(x,y)dxdy}{\iint_{\infty} E^2(x,y)dxdy} \tag{3.2}$$

In order to maximise the first factor in Eq. 3.1 to 1, the grating was chosen to be first order (m= 1), with aspect ratio δ= 50%, hence Eq. 3.1 simplifies to:

$$\kappa = \Gamma_g \frac{{n_1}^2 - {n_2}^2}{\lambda_B n_{eff}} \tag{3.3}$$

The period Λ was calculated from the Bragg formula $\Lambda = \lambda_B/2n_{eff}$, using the effective refractive index calculated for the optimum RWG structure using FIMMWAVE. Since n_{eff} was found to be 3.3, the grating period Λ at 1.35 μm was calculated to be around 205 nm.

In order to estimate Γ_g using Eq. 3.2, it was followed the approach suggested in [Agrawal 86], where the field distribution $E(x, y)$ is approximated to be that of a structure in which the grating pitch is a continuous medium having dielectric constant ϵ_{ave} given by the average between ϵ_1 (semiconductor) and ϵ_2 (SiO_2 layer), as in Fig. 3.3.

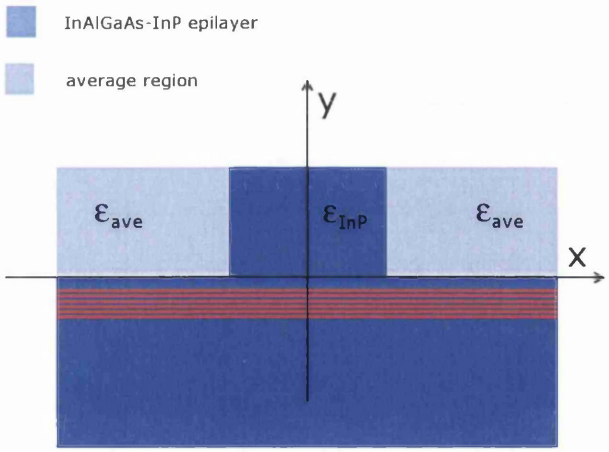

Figure 3.3: Schematic of the approximated lateral grating structure used to simulate the grating confinement factor Γ_g.

Using the relation $n = \sqrt{\epsilon}$, and taking $\epsilon_1 = 10.1$ and $\epsilon_2 = 2.1$, n_{ave} was found to be 2.47. The structure was simulated using FIMMWAVE, varying the depth of the ridge h and the grating width w, and the calculated $E(x, y)$ was integrated over the grating region using MATLAB. By substituting the values for Γ_g into Eq. 3.3, an estimate of the coupling coefficient can be given for different ridge configurations. Fig. 3.4(top) shows simulated values of κ as a function of the etch

depth h, and Fig. 3.4(bottom) simulated κ for different recess depths w.

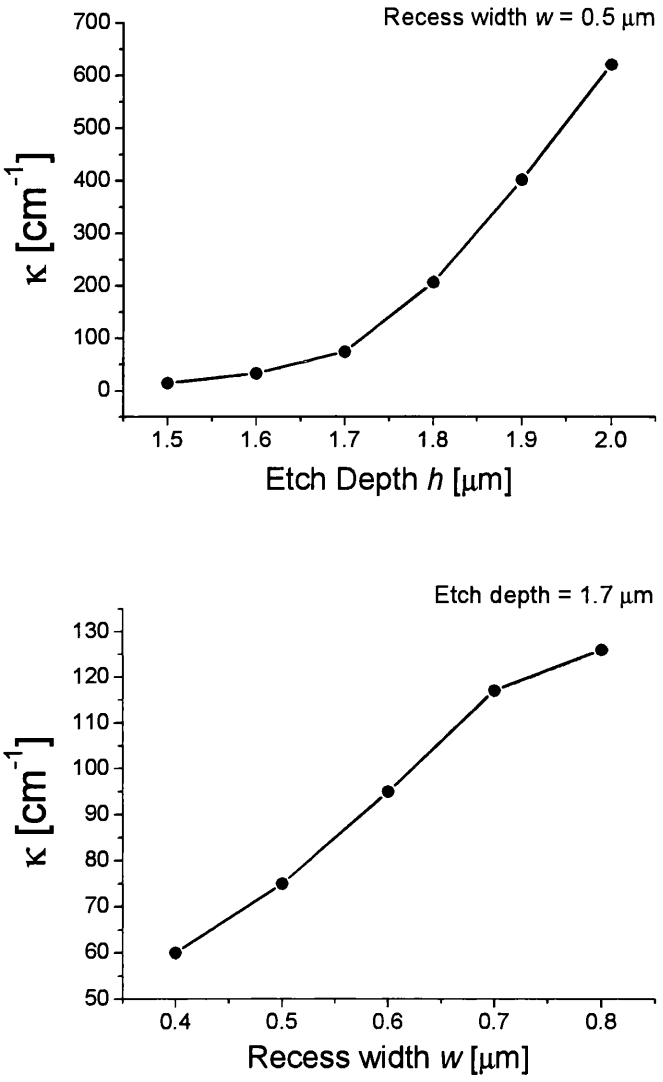

Figure 3.4: Dependence of κ over (top) grating etch depth (w=0.5 μm), (bottom) recess depth (1.7 μm etch depth); for a RWG width of 2.5 μm covered with a SiO_2 ($n(SiO_2)$=1.44) insulation layer.

From these plots it can be noticed that κ depends critically on the geometry of the structure, in particular on the etch depth. The reason is that the confinement

of the mode is very sensitive to variations of the RWG depth: if the ridge is too deep the mode will be more confined in the horizontal direction, if it is too shallow it will be more confined in the vertical direction. In order to guarantee good single-mode operation, the grating was finally designed to have a 0.5 μm recess and a 1.7 μm etch depth. This geometry should give a 75 cm coupling coefficient, which for a 600 μm long DFB gives a high κL product of 4.5.

3.3 Modelling of the single-mode lasers

Initial modelling was performed on single-mode DBR lasers. Since from previous simulations the κ coefficient was estimated to be around 75 cm^{-1}, the reflector length L_g was designed to be 300 μm, to give high power reflectivity. However, later measurements showed that κ was lower than predicted, therefore, to increase the power reflectivity, the grating length was increased to 750 μm. The length of the active section was designed to minimise the threshold current I_{th}, following the theoretical model for MQW lasers by [Kurobe 88]. Recalling Eq. 2.15, and assuming 20% reflectivity from the DBR mirror and 30% from the cleaved facet, and using the material parameters already measured by oxide stripe laser (OSL) assessment, the optimum length for the gain section L_A was found to be 550 μm. It was also necessary to estimate the band-gap wavelength shift required for the grating section, in order to obtain optimum balance between high tuning efficiency and low absorption losses. This was done using the Kramers-Kronig relations, which are dispersion relations that relate the real part of the refractive index to the imaginary part, and vice versa. The expression that relates the change of the real part of the refractive index Δn to the change of the absorption $\Delta\alpha$ (or gain Δg) is:

$$\Delta n(\omega) = \frac{c}{\pi} P \int_0^\infty \frac{\Delta\alpha(\omega')}{\omega'^2 - \omega^2} d\omega' \tag{3.4}$$

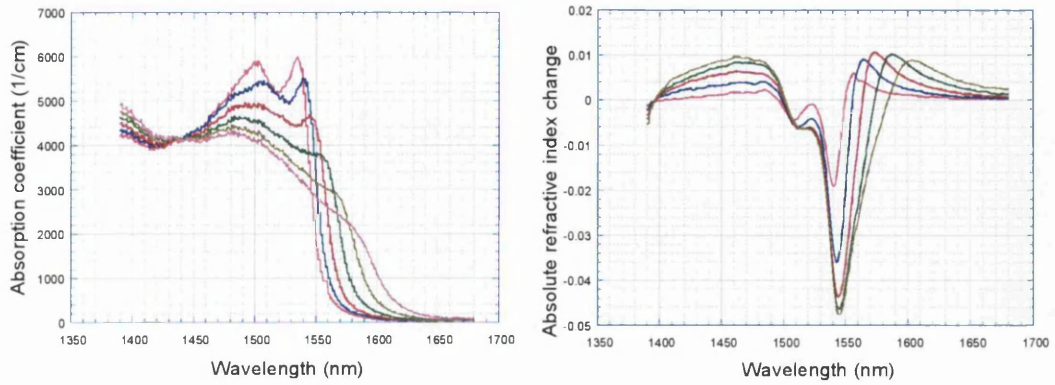

Figure 3.5: Results from measurement of absorption and refractive index change, on Al-quaternary material, for different applied voltages (Courtesy of A.J. Seeds (UCL)).

where ω is the optical frequency. This relation is routinely used to calculate the refractive index profile from losses measured over a wide range of frequencies. The typical dependence of the two components of the complex refractive index $n = n_r + n_i$ as a function of the optical wavelength, are shown in Fig. 3.5.

Using results from [Wong 05] the optimum wavelength shift was chosen to be 60 nm.

Design of the single-mode DFB lasers followed the experimental results obtained from testing of the first batch of DBR lasers, for which lasing was recorded from devices having 210 nm period. Since the DBR lasing wavelength was slightly blue shifted with respect to the gain peak wavelength, in order to define a Bragg wavelength that was 10 nm higher, some DFBs were designed (using Eq. 2.1) to have 211.6 nm period. The lateral grating was still chosen to be first order, with 50% duty cycle, 2.5 μm RWG width, and 1.7 μm etch depth. In order to investigate the effects of some design parameters over the lasing properties of the devices, recesses were chosen to be 500 nm and 800 nm.

3.4 Modelling of the dual-grating lasers

The implementation of the dual-wavelength device was focused on the requirements of a reliable, compact and low-cost solution for dual-mode operation, which could be exploited to generate frequency difference signals. The novel structure proposed in this work, that consists of a single cavity on which two different grating periods are located, undoubtedly meets all the requirements, since it is a simple structure, that comprises only one section, it requires the same technology as for single-mode DFBs, and in principle it offers the same lasing performances (I_{th}, SMSR, linewidth) as for standard DFBs. Moreover, the use of an integrated dual-mode laser has an advantage in the optimisation of optical alignment, which makes the spatial-mixing efficiency m close to 1 (section 1.1), and it should also give modes with the same state of polarisation, determined by the epitaxial structure.
Besides this, the double-grating laser was expected to offer a major benefit in consisting of only one cavity, as it will be explained in the next section.

3.4.1 Common-mode-noise rejection effect

If one considers the case of photo-mixing of two separate and independent lasers, due to the fact that the two sources are affected by uncorrelated noise terms, the quality of the generated microwave signal is affected by the combination of the two noises. On the other hand, the case of two modes propagating within the same cavity is much more favorable in terms of stability since, although the absolute frequencies of the two modes might drift, the fluctuations that arise from electrical, thermal or mechanical variations, are common to the two modes, hence they are subtracted from the difference frequency [Siegman 86]. This phenomenon, known as *common-mode-noise rejection effect*, was recently stressed by [Tani 05], who proposed to describe it using a mathematical expression called common-mode rejection ratio (CMRR). The CMRR is the ratio between the average frequency

shift for each laser mode and the shift in the difference frequency:

$$CMRR = \frac{\Delta\overline{f}}{\Delta f_{diff}} = \frac{\sqrt{(\Delta {f_1}^2 + \Delta {f_2}^2)/2}}{\Delta f_{diff}} \tag{3.5}$$

This expression gives a measure of the stability of the generated beat signal with respect to each separate mode. Experimental demonstration of the common-mode effect was reported by [Hyodo 96], using a dual-wavelength microchip laser. In that case the linewidth of each separate mode was around 100 kHz, while the generated GHz signal showed a linewidth of 430 Hz, giving a reduction of 1/230. Nonetheless, it is important to note that for the case of a monolithic device mechanical and thermal fluctuations are negligible compared to external cavity and microchip lasers, so the expected linewidth reduction is much smaller.

3.4.2 Competition between two modes

The most crucial question faced when designing the dual-wavelength laser was whether the device was capable of supporting simultaneous oscillation of two laser modes. In fact, although the cavity can potentially support two longitudinal frequencies, in practice the modes might have different gain, losses and saturation parameters, which can cause competition for the available population inversion in the cavity [Siegman 86]. For instance, oscillation of one mode can reduce the available gain and prevent the other mode from lasing. In the case of a semiconductor laser, the phenomenon of mode competition is a very complex problem, since it depends on many parameters, among which gain saturation effects, and spatial and spectral mode overlap. Here a simple model for mode competition analysis is reported, to help understanding what are the possible situations. This approach follows the notation used by Lamb, and later by Sargent [Sargent III 74].

$$\frac{dI_1}{dt} = [\alpha_1 - \beta_1 I_1 - \theta_{12} I_2] I_1 \tag{3.6}$$

$$\frac{dI_2}{dt} = [\alpha_2 - \beta_2 I_2 - \theta_{21} I_1] I_2 \tag{3.7}$$

where I_i are the mode intensities, α_i are the gain minus loss terms for each mode, and β_i and θ_{ij} are the self-saturation and cross-saturation coefficients, respectively. The β_i and θ_{ij} coefficients depend mainly on the spatial overlap between the modes, on their spectral overlap, and on the gain medium (homogeneous or inhomogeneous). Their calculation is quite complex, however, as an example, for the case of a homogeneous medium and two incoherently related modes closely spaced near the centre of the gain, these four coefficients have approximately the same value. On the other hand, in the case of an inhomogeneous medium, the cross-saturation effect is much smaller than the self-saturation.
Steady-state solutions to this set of equations are found for by setting the $\alpha_i - \beta_i I_i - \theta_{ij} I_j$ factor equal to zero:

$$I_1 = (\alpha_1/\beta_1) - (\theta_{12}/\beta_1) I_2 \tag{3.8}$$

$$I_2 = (\alpha_2/\beta_2) - (\theta_{21}/\beta_2) I_1 \tag{3.9}$$

These equations can be represented on a I_1 vs. I_2 plane and, depending on the way they do or do not intercept, one finds different situations, as shown in Figs. 3.6-3.7-3.8.

Note that the T points in Fig. 3.6-3.7-3.8 do not correspond to physical solutions (see the previous set of Eqs. 3.7). Looking at the case of no intercept (Fig. 3.6), the O_1 and O_2 solutions represent regimes of single-mode operation, while a further potential solution O_3 appears when the two lines intercept (Fig. 3.7-3.8), which represents two-mode operation. In order to figure out which of these solutions are stable, it is convenient to introduce a *coupling factor* C, in the form:

$$C = \frac{\theta_{12}\theta_{21}}{\beta_1\beta_2} \tag{3.10}$$

which is used to express the O_3 solution as:

$$I_1(O_3) = \frac{\alpha_1 - \theta_{12}\alpha_2/\beta_2}{\beta_1(1-C)} \tag{3.11}$$

$$I_2(O_3) = \frac{\alpha_2 - \theta_{21}\frac{\alpha_1}{\beta_1}}{\beta_2(1-C)} \tag{3.12}$$

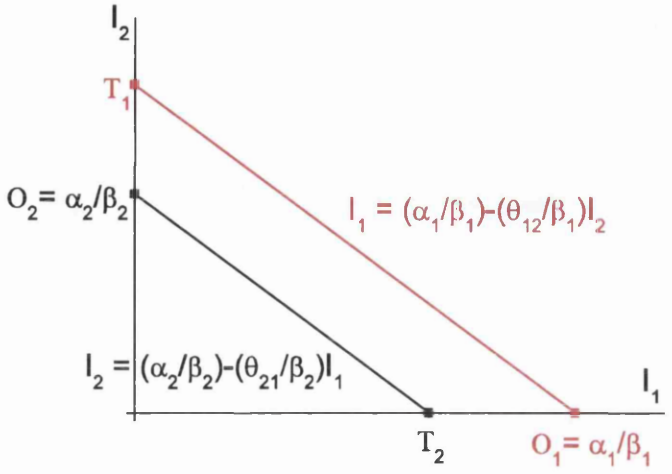

Figure 3.6: Solution to the mode competition analysis: no intercept.

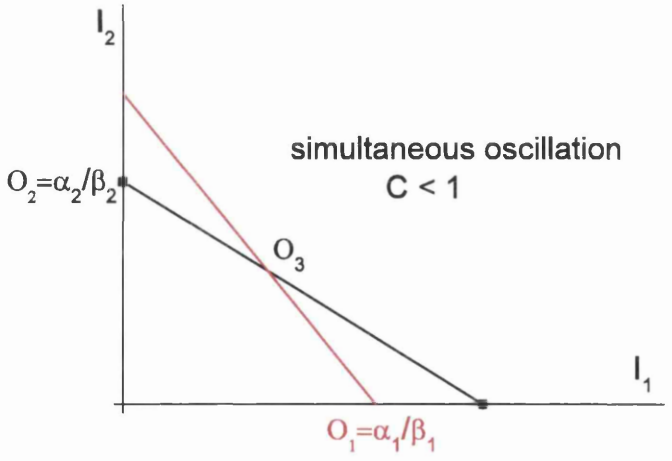

Figure 3.7: Solution to the mode competition analysis: O_3 is stable solution, while O_1 and O_2 are unstable.

Steady-state conditions are then found by performing a small-signal analysis, which yields the following results:

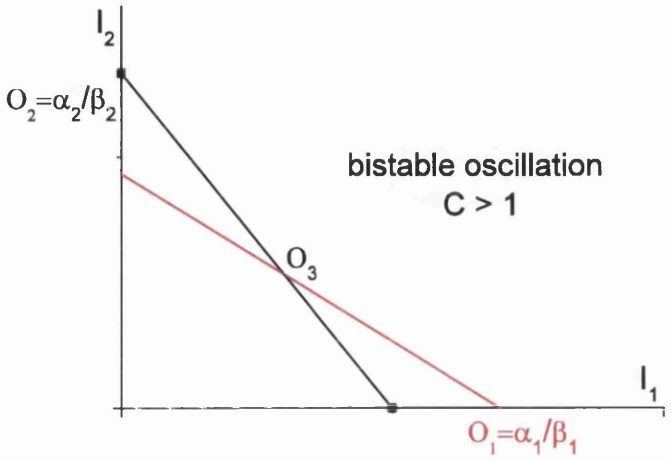

Figure 3.8: Solution to the mode competition analysis for the case: both O_1 and O_2 are stable solutions, while O_3 is unstable.

- Fig. 3.6 O_1 is a stable solution, O_2 is unstable
- Fig. 3.7 In the $C < 1$ condition (weak-coupling), both O_i and O_2 solutions are unstable, while O_3 is stable
- Fig. 3.8 In the $C > 1$ condition (strong-coupling), both O_1 and O_2 are stable, while O_3 is unstable

3.5 Conclusions

The design of DBR and DFB lasers was reported. InAlGaAs-InP single-mode DBRs were designed on a ridge waveguide geometry. Using a commercial software, it was found that single-mode operation was achieved with a 2.5 μm wide waveguide. The corresponding effective refractive index was used to design the Bragg grating period, at 1.35 μm wavelength, which was found to be 210 nm. Further simulations were run to estimate the strength of the coupling coefficient κ, for

different widths and etch depths of the ridge waveguide, with a 50% duty cycle. In order to have a κ of around 75 cm^{-1}, the Bragg grating was chosen to be 1.7 μm deep, 300 μm long, and with 0.5 μm recess. Taking into account the reflectivity of the grating and of the cleaved facet, the optimum length of the active section of the DBR laser was estimated to be 550 μm. The band-gap of the passive section was also designed to be blue shifted by 60 nm, using QWI. Design of single-mode DFBs followed the first experimental results from the fabricated DBRs. The ridge waveguide parameters and the grating period were confirmed, while lengths were varied between 600 μm and 1 mm. Since the lasing wavelength of the DBR lasers was slightly blue shifted, some DFBs were designed with a higher Bragg period of 211.6 nm, which was estimated to increase the lasing wavelength by 10 nm. Moreover, since testing of early devices gave lower κ than designed, subsequent batches were etched deeper, to give a higher coupling coefficient.

Dual-wavelength DFBs were designed with the same ridge waveguide geometry as for the single-mode devices, aiming to achieve simultaneous lasing of two different Bragg frequencies within the same cavity. The motivation for this choice came from the so-called common-mode-noise rejection effect, as it was explained in detail. Finally, to help understanding the various regimes which can take place in multi-mode oscillators, a simple model on competition between two modes was presented. This shows that simultaneous dual-mode operation is predicted under weak-coupling conditions.

Chapter 4

Device fabrication

In this research InAlGaAs-InP DFB lasers, both single- and dual-mode, were fabricated. Single-mode DBRs were also fabricated on the same material, to show the potential for integration of these devices. In this Chapter the material employed, with its main characteristics, is presented and the processing required to fabricate lateral gratings, Fabry-Perot lasers, DBR and DFB lasers is described in detail. An overview on the technological issues which were highlighted during the work will be also given.

4.1 InAlGaAs-InP MQW material structure

The devices reported in this thesis were fabricated on an InAlGaAs-InP multi-quantum-well (MQW) wafer emitting at around 1.35 μm, that was grown by molecular beam epitaxy (MBE). The material, known as Al-quaternary alloy, is considered very promising due to low threshold current and high-temperature operation [Lin 99]. The cap layer is a heavily doped ($p = 10^{19}$ cm^{-3}), 200 nm thick $In_{0.53}Ga_{0.47}As$. The upper cladding comprises a 1600 nm InP layer ($p = 10^{18}$ cm^{-3}), a 20 nm undoped InP layer, a 5 nm undoped $In_{0.72}Ga_{0.28}As_{0.6}P_{0.4}$ layer, a 30 nm undoped InP layer, a 50 nm p-doped $In_{0.52}Al_{0.48}As$ ($p = 5 \cdot 10^{17}$ cm^{-3}) layer, and a 50 nm p-doped $In_{0.52}Al_{0.4}Ga_{0.08}As$ ($p = 5 \cdot 10^{17}$ cm^{-3}) layer. The active region

consists of six 6 nm thick $In_{0.73}Al_{0.165}Ga_{0.105}As$ quantum wells (QWs) and seven 10 nm thick $In_{0.52}Al_{0.36}Ga_{0.12}As$ barriers. The lower cladding consists of a 50 nm n-doped $In_{0.52}Al_{0.4}Ga_{0.08}As$ ($n = 5 \cdot 10^{17}$ cm^{-3}) layer, a 50 nm n-doped $In_{0.52}Al_{0.48}As$ ($n = 5 \cdot 10^{17}$ cm^{-3}) layer, a 20 nm n-doped $In_{0.52}Al_{0.4}Ga_{0.08}As$ ($n = 10^{18}$ cm^{-3}) layer, and a 50 nm n-doped InP ($n = 10^{18}$ cm^{-3}) layer. The whole structure was grown on top of an n-doped InP substrate. It is worth noticing that the material structure comprises a higher energy band-gap layer, $In_{0.52}Al_{0.48}As$, to minimise the thermal roll-off effects and enhance the carrier confinement [Minch 99], which can also be used as a dry-etch stop-layer [Shinoda 03]. Fig. 4.1 shows a schematic of the material, while the detailed epilayer structure is reported in Tab. 4.1.

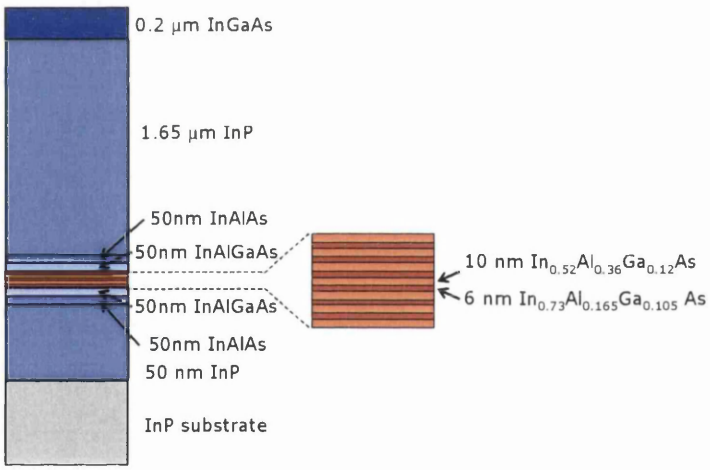

Figure 4.1: Schematic of the InAlGaAs-InP material used.

Two wafers (MBE3183 and MBE3186) with identical composition and slightly different characteristics were employed in this research. They were characterised by fabricating and testing oxide stripe lasers (OSL). From the assessment, the threshold current at infinite length $J_{th}(\infty)$ was estimated to be 1.23 kA/cm^2 and

THICKNESS [nm]	MATERIAL	DOPING [cm^{-3}]
200	$In_{0.53}Ga_{0.47}As$	10^{19} Zn
1600	InP	10^{18} Zn
20	InP	
5	$In_{0.72}Ga_{0.28}As_{0.6}P_{0.4}$	
30	InP	
50	$In_{0.52}Al_{0.48}As$	$5{\cdot}10^{17}$ Be
50	$In_{0.52}Al_{0.4}Ga_{0.08}As$	$5{\cdot}10^{17}$ Be
6 X 6	$In_{0.73}Al_{0.165}Ga_{0.105}As$	
7 X 10	$In_{0.52}Al_{0.36}Ga_{0.12}As$	
50	$In_{0.52}Al_{0.4}Ga_{0.08}As$	$5{\cdot}10^{17}$ Si
50	$In_{0.52}Al_{0.48}As$	$5{\cdot}10^{17}$ Si
20	$In_{0.52}Al_{0.4}Ga_{0.08}As$	
50	InP	
	S-doped InP	

Table 4.1: Epilayer structure of the material used in this research.

0.62 kA/cm^2, for MBE3183 and MBE3186 respectively. After these results, initial work was carried out on the less performing material (MBE3183), then, once the technology had proved to be mature, devices were fabricated on the MBE3186 wafer material.

4.2 Grating fabrication

In order to optimise the parameters required to define the Bragg structure, preliminary fabrication tests were performed on sets of different gratings. Since the grating period is in the range of 200 nm, electron beam lithography (EBL) is required to define the designed pattern.

4.2.1 Electron beam lithography

EBL is a type of lithography in which an electron gun (e-beam) is used to expose an electron sensitive layer, usually an organic polymer, called resist. Exposure of resist to the e-beam induces a reaction, which causes the resist to become either more or less sensitive to a developer solution. This lithographic technique, thanks to small beam sizes and very precise stage control, which makes use of an interferometric technique, offers very high resolution, down to 10 nm or less [Macintyre 06]. Moreover, since it is a direct writing technique, i.e. the beam is scanned along the sample, it is a very flexible tool, hence useful for research purposes. However, it has some disadvantages, which are mainly high maintenance costs and long writing times, compared to other patterning techniques such as optical lithography (photolithography) or direct imprint lithography.
The EBL machine used in this work is a EBPG5-HR100 (Electron Beam Pattern Generator), made by Leica Microsystems Lithography. The EBPG5, also called beam-writer or e-beam machine, is a commercial tool capable of writing features down to 20 nm. The first step in fabricating the gratings was to find the optimum e-beam parameters to define the pattern. EBL masks that comprised the recessed gratings were designed using a computer aided design (CAD) software called L-Edit [Tanner EDA]. After performing tests using different resists recipes and e-beam doses, the resist mask was chosen to be a 200 nm thick polymethyl methacrylate (PMMA) bi-layer. Writing tests with different pitch aspect ratios and different recess depths were then carried out, searching to optimise the process performance, both in terms of rendering and of writing time. In fact, it is very important to maximise the efficiency of the process, by minimising the writing time, not only to reduce machine costs, but also more importantly to avoid temperature drift effects. The optimum mask was finally designed to have 75:25 aspect ratio, as shown in Fig. 4.2.

Due to an effect known as *proximity effect*, the actual grating pattern, that

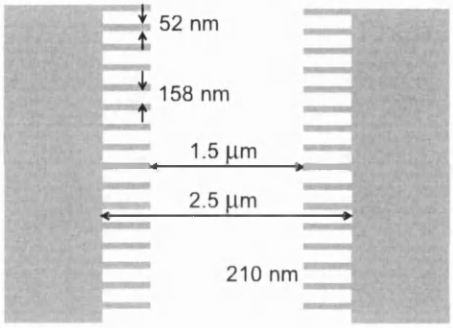

Figure 4.2: Bragg grating pattern, as it was designed with L-Edit.

Figure 4.3: Monte Carlo simulation of a Si substrate irradiated by an e-beam, showing backscattered electrons, from [Macintyre 06].

appears on PMMA after sample development, has 50:50 aspect ratio, has designed in 3.2. The proximity effect is due to backscattered electrons that are generated within the sample when it is irradiated, and it causes beam spreading, as shown in Fig. 4.3.

In this work the proximity effect proved advantageous in reducing the writing time. In general, however, this effect is a major problem when writing narrow features, since it broadens the patterns. In practice, it is usually corrected by using a software tool that, after simulating the effect in the material of interest,

allows adjustment of the e-beam dose to achieve the wanted electron distribution. In this work possible detrimental effects of proximity on the required features were investigated by comparing results from gratings fabricated with and without proximity correction. Interestingly, from these tests it appeared that the effect was minor, and introduction of correction did not produce any noticeable improvement. For this reason the rest of the work was carried out without use of proximity correction.

Another critical issue related to EBL is the stitching effect, which is generated by the limited writing field of the EBL (typically 800 μm by 800 μm). To write patterns larger than the writing field, the sample has to be mechanically moved and realigned to the EBL axis. Even the most accurate mechanical stage produces stitching errors between writing fields in the order of 40-60 nm, which introduce phase jumps in the grating. This was circumvented by ensuring that the grating lengths were within block size dimension and by adjusting the pattern design in such a way that the critical parts of the pattern were away from block boundaries. Finally, the optimum pattern was defined using two 100 nm thick 2041 PMMA layers, an e-dose of 310 $\mu C/cm^2$, and no proximity correction. Fig. 4.4 shows a resist pattern defined using the above parameters: the pattern is very clean and well defined.

Patterning of dual-gratings was also carried out using EBL. In this case the pattern was designed by defining two independent structures, one on each side of the waveguide, in order to be able to assign a different step resolution to each of them. This approach is illustrated in Fig. 4.5, where a typical dual-wavelength grating layout is shown. In this picture each colour corresponds to a different Bragg period, which is written by using its own specific resolution. Importantly, although the resolution difference required for the gratings is lower than that of the machine, in practice the significant parameter for writing dual-gratings is the differential resolution. Due to the fact that any mechanical perturbations of the system are seen by both, the common mode error is extremely low.

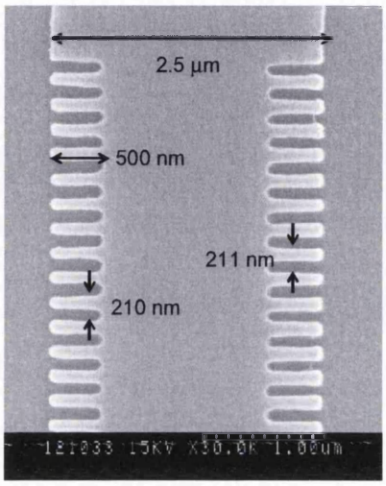

Figure 4.4: Scanning electron micrograph of PMMA resist mask (top view), reporting the actual grating sizes.

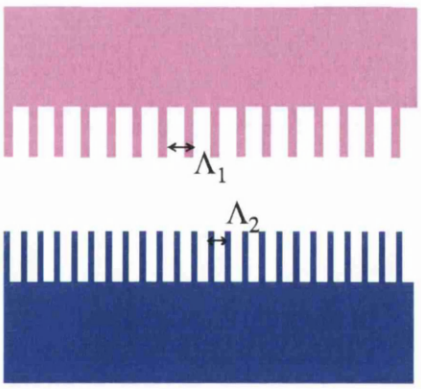

Figure 4.5: Pattern of a dual-wavelength Bragg grating, as it is designed using L-Edit.

4.2.2 Reactive ion etching

After defining the PMMA pattern by EBL, to avoid depletion of the mask during the next etching steps, the pattern was transferred into a 200 nm thick plasma

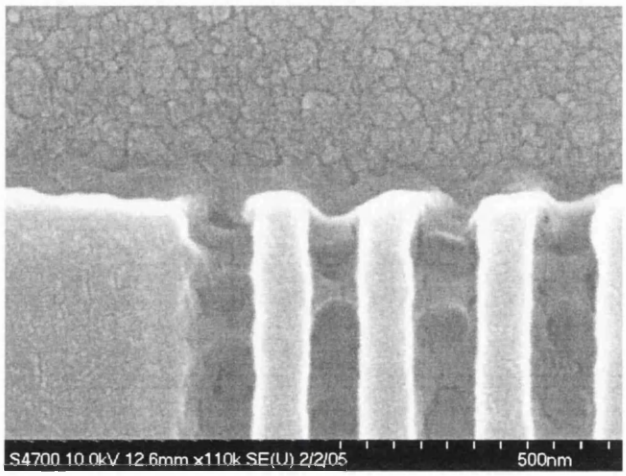

Figure 4.6: SEM picture of the SiO_2 mask (detail).

enhanced chemical vapour deposition (PECVD) SiO_2 layer by reactive ion etching (RIE). Plasma is initiated in the chamber by applying a strong radio frequency (RF) EM field, then, due to a large voltage difference within it, (positive) ions tend to drift toward the wafer platter, where they collide with the samples to be etched. Unlike wet-etching, dry-etching can provide a very anisotropic attack, which allows definition of vertical structures.
The first dry-etching step was the mask transfer from PMMA into SiO_2, using CHF_3. The result was assessed using a scanning electron microscope (SEM); Fig. 4.6 shows a detail of the etched SiO_2 mask, that proves good definition of the grating pattern.

To assess the effectiveness of the SiO_2 mask, etching tests were first carried out on AlGaAs-GaAs samples, whose etching process is well established. GaAs etching was performed using $SiCl_4$ in a BP80 machine (Oxford Plasma Technology). Inspection of the fabricated gratings, using an SEM, gave very promising results, showing very well defined and narrow structures (Fig. 4.7). Fig. 4.7(right) shows a detail of the lateral grating, where two distinct vertical profiles can be recog-

nised: this feature was due to different material composition within the ridge, which was then affected in a slightly different way in the vertical direction during the dry-etching process.

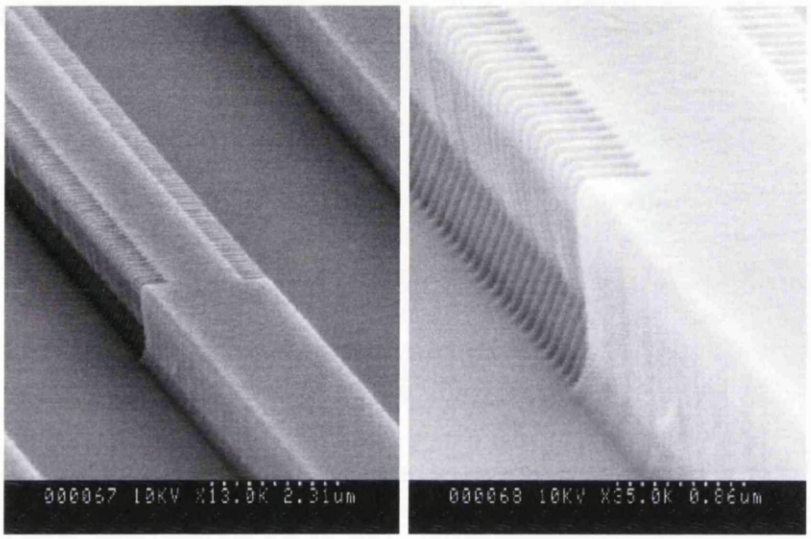

Figure 4.7: Grating fabrication tests on an AlGaAs-GaAs sample: (left) first-order lateral grating on a ridge-waveguide structure; (right) zoom on the grating pitch.

Subsequently, test structures were fabricated on InAlGaAs-InP test samples. Using SiO_2 as an etching mask, the InP cladding was etched using CH_4 and H_2 gases, in an ET 340 (Electrotech Plasmafab). SEM inspection of the etched Al-quaternary samples showed a well defined, vertical profile, as it can seen in Fig. 4.8, although the profile roughness is much higher than on the AlGaAs-GaAs material system. This confirms that etching of quaternary alloys has not yet reached the same maturity as that of GaAs processing. On the other hand, it is worth noting that in shallow etched gratings the mode only interacts with the very bottom area of the grating, therefore the roughness on the top of the waveguide does not affect the device performance.

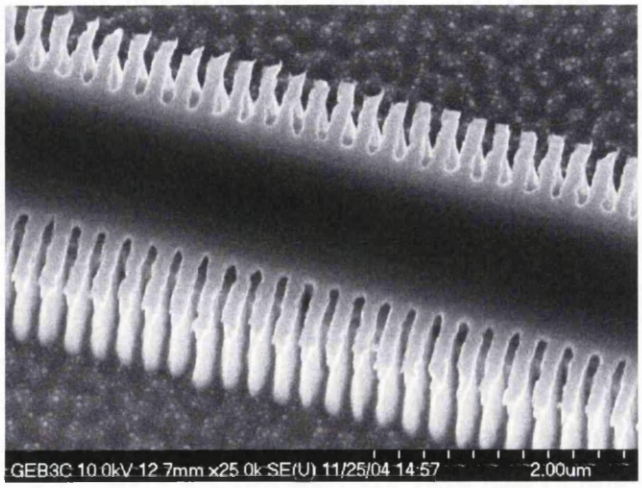

Figure 4.8: Grating fabrication test on an InAlGaAs-InP sample.

4.3 Fabrication of DBR and DFB lasers

DBR and DFB lasers were fabricated on the InAlGaAs-InP multi-quantum-well (MQW) material emitting at 1.35 μm. Table (4.2) lists the main technological steps undertaken in the fabrication process.

Fabrication of DBR lasers differs from DFBs in that it is preceded by a process known as *quantum well intermixing* (QWI), aimed at shifting the bandgap of the grating section. This process is reported in detail below, in section (4.3.1). Once intermixing has been completed, fabrication of DBRs and DFBs can carry on simultaneously.

First, gold markers are defined on top of the sample, as reference marks for the next EBL steps, using lithography (either optical or electronic), gold evaporation and metal lift-off. Next, the required laser pattern is defined, using EBL on PMMA resist. The pattern is transferred into a 200 nm thick PECVD SiO_2 layer, and then the ridge-waveguides are etched into the InP upper cladding layer. Subsequently, a 200 nm thick insulating layer (SiO_2) is deposited, and contact windows are defined on top of the ridge structure, and etched using dry-etching. The contact

PECVD SiO_2 Deposition	
Intermixing Pattern Definition	E-beam Lithography SiO_2 mask Etching
Sputtered SiO_2 Deposition	
Annealing	
SiO_2 Mask Stripping	

Markers	Lithography Metal Deposition Lift-Off
PECVD SiO_2 Deposition	
RWG and Grating Definition	E-beam Lithography SiO_2 mask Etching InP Etching
SiO_2 Mask Stripping	HF acid wet-etch
PECVD SiO_2 Deposition	
Contact Windows	E-beam Lithography SiO_2 Etching
P-type Contacts	E-beam Lithography Metal Deposition Lift-Off
Sample Thinning	
N-type Contact	Metal Deposition
Contacts Annealing	@ 360 C for 1 minute
Cleaving	
Mounting	

Table 4.2: (left) DBR sample preliminary processing, in order to shift the bandgap of the grating section; (right) DBR and DFB laser fabrication steps.

pattern is defined on the $p-$side by EBL, and a Ti-Pd-Au metal layer is deposited, using electron-gun evaporation (Plassys). The sample is thinned to a thickness of approximately 250 μm, using a mixture of water and Al_2O_3 powder. Finally, an n-type contact layer is deposited on the substrate side, and the sample is then annealed at 360 °C for 60 seconds. The devices are cleaved, only at one end, to provide optical output and reduce facet reflection effects, and mounted on top of brass mounts, using an epoxy adhesive film.

Ridge-waveguide lasers were also fabricated on the InAlGaAs-InP multi-quantum-well (MQW) material emitting at 1.35 μm. Since the required processing steps are identical to what described above for DFB lasers, it was possible to fabricate them simultaneously, alongside DBRs and DFBs, on the same sample. A schematic of the necessary technological steps is illustrated in Fig. 4.9(top), while the final

result for a RWGL is shown in the SEM picture in Fig. 4.9(bottom).

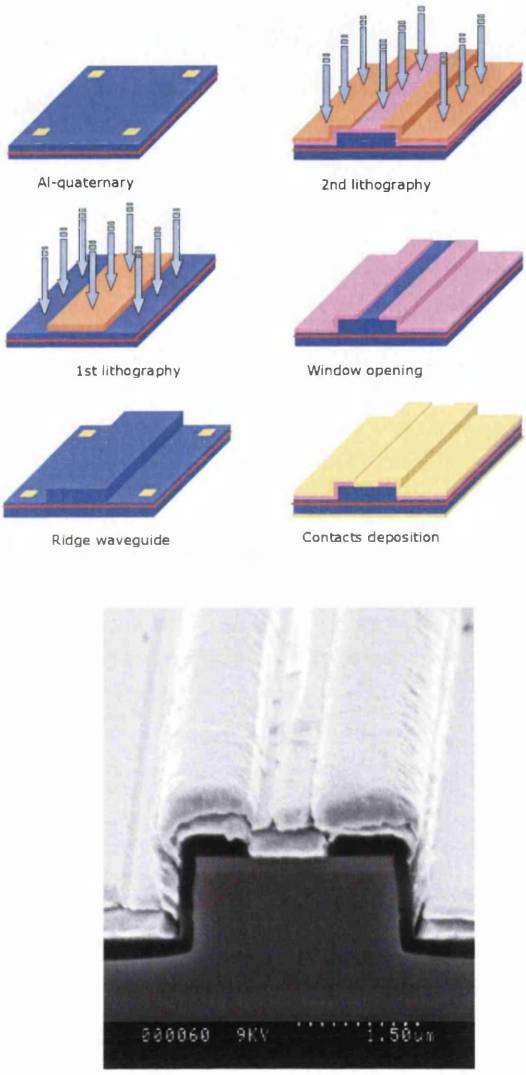

Figure 4.9: (top) Schematic of the RWGL fabrication process; (bottom) Transversal section of a ridge-waveguide laser fabricated on the InAlGaAs-InP material.

4.3.1 Intermixing

In order to passivate the Bragg section of the DBRs, i.e. to reduce losses in the grating section, a quantum well intermixing (QWI) process [Marsh 99] was used in this work. The process is aimed at shifting the core band-gap of the grating, precisely to blue-shift it, to prevent direct band-gap absorption. In the literature several techniques can be found, as in [Skogen 05], [Teng 00], or using ion implantation [Rennon 01]. However, the technique available at Glasgow, and that was employed in this work, is based on sputtered SiO_2, which relies on the generation of point defects during the sputtered silica deposition. By subsequently annealing the material at high temperature (700-900 °C), point defects diffuse into the QWs and promote interdiffusion between wells and barriers (Fig. 4.10). As a result, the band-gap of the material shifts to higher energy. The main advantage of this technique is that it is a fully post-growth process, hence it does not require re-growth, that is generally a complex process.

Before processing the actual DBR samples, tests were carried out in order to inspect the effect of intermixing on the InAlGaAs-InP material. Test samples were assessed by measuring their photo-luminescence (PL) emission at low temperature (77 °K), before and after annealing at different temperatures. A typical plot of PL tests is shown in Fig. 4.11. The actual DBR samples were finally annealed at 750 °C, for 30 seconds, in order to shift the emission peak by 60 nm.

4.3.2 Optimisation of InP etching

Etching of InP is a critical technological step in grating definition. Although a swift inspection of etched gratings on InP material sample shows vertical profile, with precise definition of the grating pitch, as in Fig. 4.8, from a closer SEM assessment it appears that the recesses are not so well defined. From Fig. 4.12, for instance, it appears that the grating is not completely etched at the bottom of the ridge waveguide.

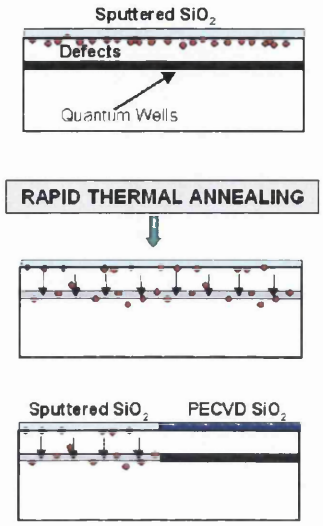

Figure 4.10: Schematic of the quantum well intermixing process.

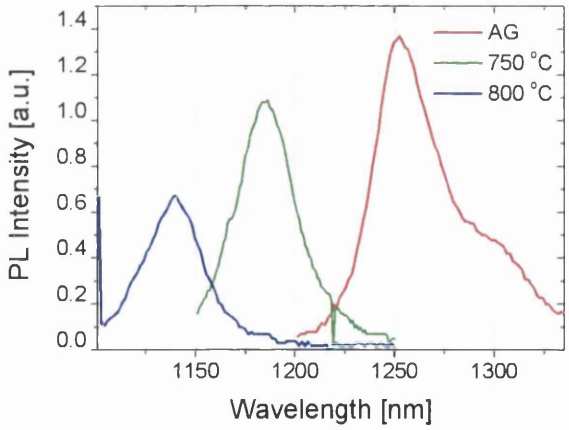

Figure 4.11: Intermixing tests: Photoluminescence measurements on material 3183, comparing PL emission from an as grown (AG) sample, a sputtered sample annealed at 750 °C for 60s (with 15s raising time), and one annealed at 800 °C for the same settings.

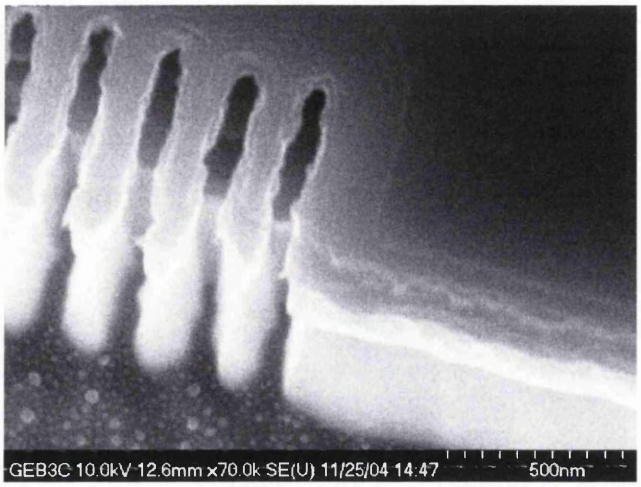

Figure 4.12: Grating fabrication tests on an InAlGaAs-InP sample, showing a not fully opened recess.

The issue results even more clear when looking at a section cleaved at an oblique angle (Fig. 4.13).

This is a detrimental feature which affects the coupling coefficient strength, reducing the reflectivity of the fabricated structures. These etch results are probably due to the formation of a polymer during CH_4/H_2 run, which acts as a mask for the ongoing etching process. It has been reported [Shinoda 03] that the addition of a small amount of O_2 to the gas mixture partially removes the polymer. Moreover, since in $CH_4/H_2/O_2$ gases InAlAs has a lower etch rate than InP (ratio 10:1), the InAlAs layer can be used as an etch-stop layer to ensure careful control on the desired etch depth. Further etch tests were designed, in order to optimise the process, using structures comprising shifted gratings. This geometry allows inspection of the transversal section at different positions with respect to the grating period. Preliminary tests were performed, adding O_2 to the CH_4/H_2 mixture, and varying the RF power. As an example, Fig. 4.14 shows results from etching at higher power (100 W), causing SiO_2 mask depletion. Up to now, these experiments did not lead to substantial improvements, and further extensive work will be needed.

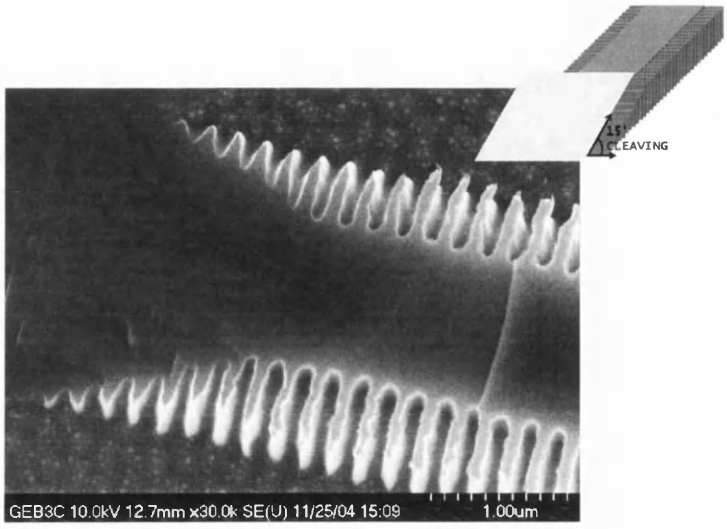

Figure 4.13: Grating fabrication tests on InP: top view of lateral gratings showing under-etching at the bottom of the ridge waveguide.

As a result of the non-complete etching, the coupling strength of the grating is reduced. This reduction can be compensated at the design stage and it will be discussed in more detail in the experimental section of the thesis (5.2).

4.4 Conclusions

The Al-quaternary MQW material employed to fabricate DBRs and DFBs in this research was described. The technological steps required to define the devices were described, stressing in particular those parameters and effects which are relevant to the fabrication of good quality lateral gratings. The key processes were electron beam lithography, reactive ion etching and quantum well intermixing. Results from accurate assessment of InP gratings that were fabricated by RIE were described more in detail. They showed some features which are detrimental to the device performances; possible solutions which will require future work were suggested.

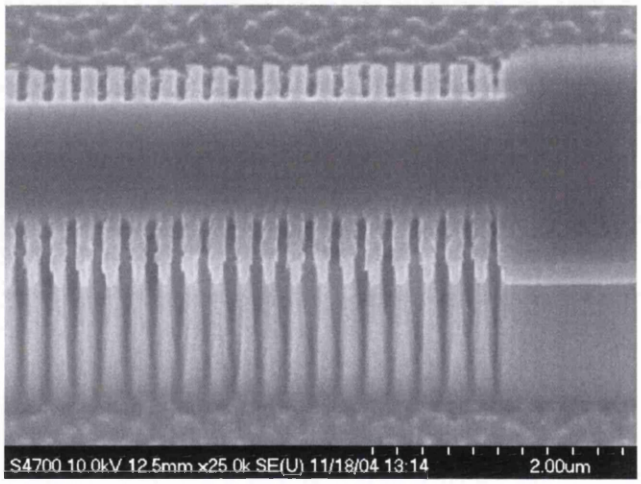

Figure 4.14: Further InP fabrication tests: lateral gratings etched at higher power (100 W), showing SiO_2 mask depletion, along with surface damage.

Chapter 5

Single-wavelength lasers

Lasers emitting one longitudinal mode were fabricated in the first stage of the project, to check both the feasibility of the fabrication process and as a reference, for future comparison with dual-mode lasers. Standard RWG lasers were also fabricated alongside DBRs and DFBs, for further comparison. In this Chapter results from the characterisation of these devices will be shown.

5.1 DBR lasers

In order to assess the properties of the lateral grating, DBR lasers were fabricated varying several design parameters of the Bragg structure, so-called *bracketing*. Fig. 5.1 shows the design parameters under investigation. Assessed lengths (L_{DBR}) of the Bragg section were (100, 200, 300, 400) μm, periods (Λ) were (200, 205, 210, 215) nm, recesses (w) (+500, -300, -500, -700) nm (here "+" and "-" indicate an increase and decrease in the waveguide width, respectively), while the gain section length L_A was designed to be 550 μm (section 3.3).

A few batches of samples comprising single-mode DBR lasers were fabricated, all of them having an etch depth of 1.68 μm.

Device testing was conducted under CW conditions, on a copper heat sink, over a temperature range between 12.5 °C and 25 °C, by coupling light into a lensed

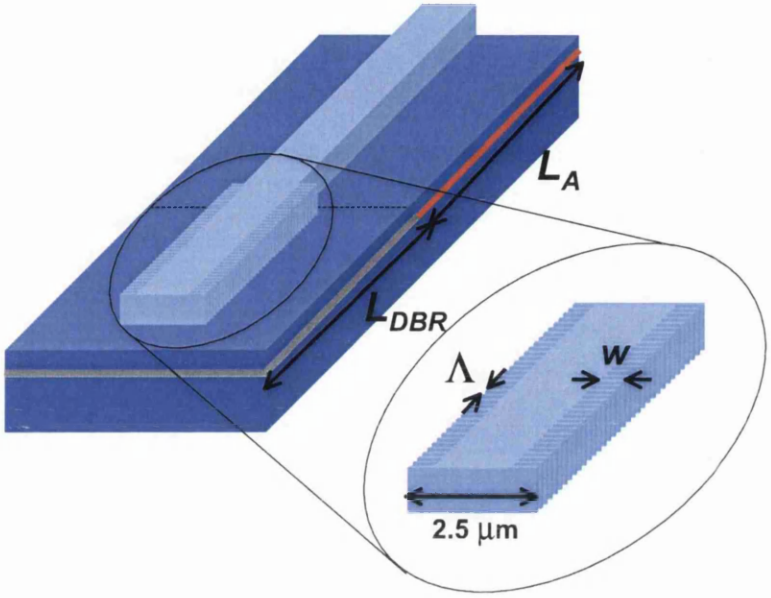

Figure 5.1: Schematic of the lateral grating DBR laser, showing the design parameters L_{DBR} (grating length), L_A (gain section length), Λ (grating period), and w (grating recess).

single-mode fibre with an angled facet at the other end, to ensure optical isolation.

5.1.1 Lasing characteristics

The Light-Current (L-I) characteristic, that is the laser output power as a function of the injected current, was assessed by driving the devices at a constant temperature, using a current source with integrated temperature controller (Newport Model8000). The light was coupled into the lensed fibre, which was connected at its other end to a photodetector (Anritsu MA9611A). The measured data were collected through an automated Labview program.

Among the bracketed devices, those with 210 nm period and (-500, -700) nm recess (from here on the "-" sign will be omitted), showed a clear threshold, proving

laser action. This information was also used to retrieve the effective refractive index n_{eff} from Eq. 2.1, which was found to be 3.2, close to what predicted in section 3.2.

Typical threshold current values I_{th} were found to be around 70 mA, as shown in the plot in Fig. 5.2left. The I_{th} value is slightly higher than expected, probably due to the fact that the recesses was not fully opened at the bottom of the waveguide (section 4.3.2).

Optical spectra were also taken, using an optical spectrum analyser (OSA) with 0.07 nm resolution (Agilent 86140B), showing stable single-mode operation at 1344.4 nm (Fig. 5.2right).

5.1.2 Tuning

The tuning behaviour of the fabricated DBR lasers was assessed both by varying the temperature of operation and by carrier injection into the grating section.

The temperature tuning coefficient was measured to be 0.09 nm/°C, for all the single-mode devices. This value is in very good agreement with previously reported results [Buus 05].

On the other hand, current tuning was not as effective as expected. On a first set of devices, current tuning showed shifts of 0.2 nm for injected currents around 20 mA, and above that value of current the mode power decreased very rapidly. Such small tuning range could be explained by measuring the spontaneous emission spectrum from the DBR section: the results showed that the emission peak of the intermixed section was at 1240 nm, which is 30 nm more than designed. Due to the fact that the operating wavelength was far from the DBR bandgap, the change in refractive index caused by injected carriers was very small. Further tests on devices fabricated on a different sample, which had been blue shifted by about 40 nm, lead to at most 1 nm variation, when injecting current up to 40 mA. In this case, the effectiveness of the QWI process was assessed by measuring

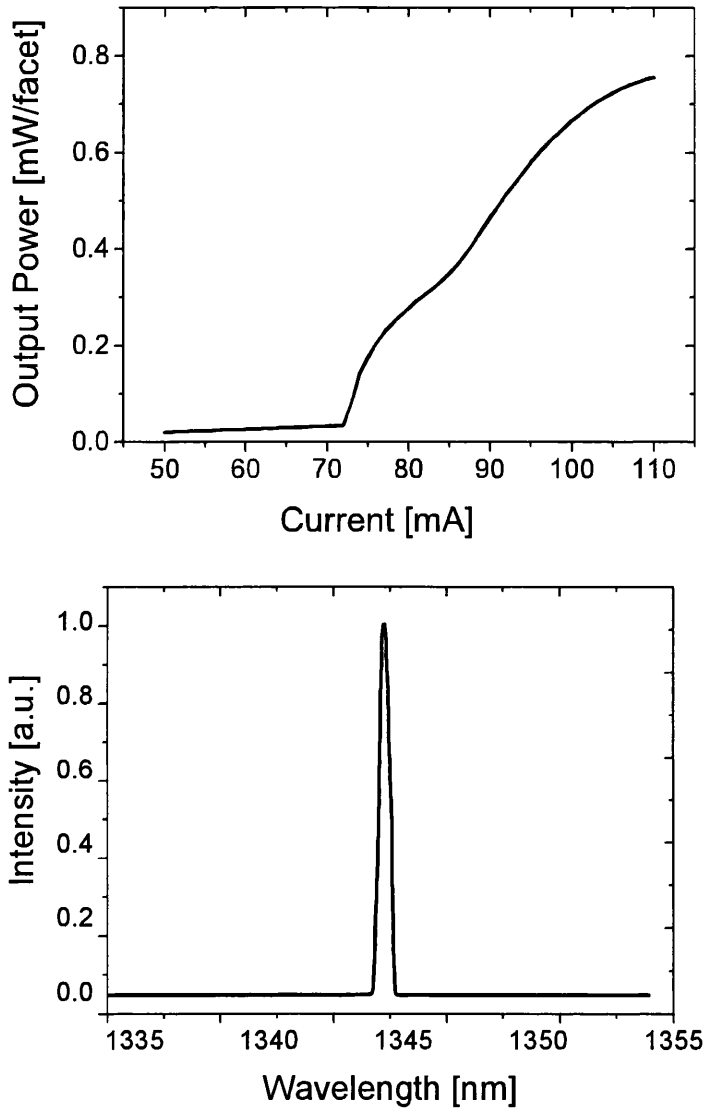

Figure 5.2: DBR laser having Λ= 210 nm, L_{DBR}= 400 μm, waveguide width (W) = 2.5 μm, 1.68 μm etch depth, and active section L_A=520 μm: (left) L-I curve; (right) optical spectrum (resolution bandwidth = 0.07 nm).

absorption losses, using intermixed ridge-waveguides that had been fabricated for this purpose, on the same sample alongside the DBR devices. The passive RWGs were characterised using the Fabry-Perot technique, giving losses of around 5 cm^{-1},

at the material emission wavelength of 1340 nm. These residual losses are likely to be due to free carrier absorption in the doped claddings. The variable results obtained on current tuning confirm that the effectiveness of the current-injection tuning critically depends on the band-gap shift between the DBR and the active section.

5.1.3 Measurement of the coupling coefficient

Various attempts were made in order to measure the coupling coefficient κ for the fabricated lateral gratings. Initially, transmission through passive grating structures was assessed, using a commercial tunable laser source (HP 8167B). However, κ proved to be too low to retrieve any useful data, and the only detected effect was given by the Fabry-Perot cavity, defined by the sample cleaved facets. For this reason angled waveguide structures were defined, but in this case coupling of light from the tunable laser was practically impossible. Finally, the coupling coefficient for the fabricated lateral gratings was estimated by measuring the transmission from the back DBR grating using the spontaneous emission (SE) of the active section as a light source. From these measurements the coupling coefficient was estimated to be 8 cm^{-1}, which is lower than expected. Again, this result is explained by the fact that gratings were not well etched at the bottom of the ridge.

5.1.4 Comparison with ridge-waveguide lasers

Fig. 5.3 shows a comparison between L-I curves for a RWGL ($L = 420$ μm, ridge width $W = 2.5$ μm) and a DBR laser ($\Lambda = 210$ nm, $L_{DBR} = 400$ μm, $L_A = 520$ μm, $W = 2.5\mu$m). The first one shows a I_{th} of 32 mA, while the DBR laser has a 68 mA threshold. The higher I_{th} of the DBR is explained by the low coupling coefficient, which gives a much longer cavity than the FP laser. A comparison between spectra of the same devices is given in Fig. 5.4, showing that the grating effectively acts as a narrowband filter overlapping the FP laser frequency comb.

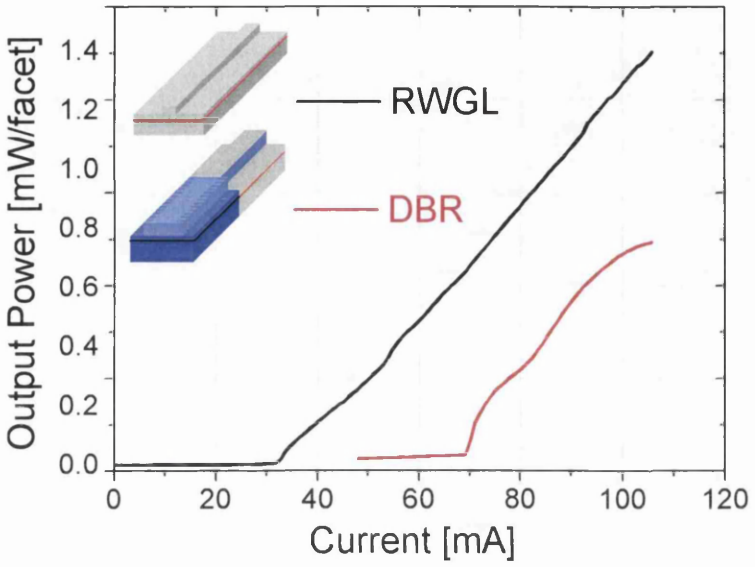

Figure 5.3: L-I curves for a RWGL (L=420 μm, W=2.5 μm) and a DBR (Λ =210 nm, L_{DBR}=400 μm, L_A=520 μm, W=2.5 μm).

The temperature tuning coefficient of the RWG lasers was also measured, yielding a change of wavelength of 0.42 nm/°C, which is about 5 times higher than the DBR coefficient. The corresponding data are plotted in Fig. 5.5. This is a further significant indication of the effectiveness of the Bragg grating [Buus 05].

5.2 DFB lasers

Single-mode DFB lasers were also fabricated choosing different design parameters. Grating periods were defined to be 210 nm and 211.6 nm, recesses were 500 nm and 700 nm, and lengths were chosen to range from 600 μm up to 1 mm. Lengths were chosen as a compromise between high enough κL product and e-beam patterning constraints. Devices were fabricated on the InAlGaAs-InP material, and again they were cleaved only at one end to avoid Fabry-Perot effects. Although DFB

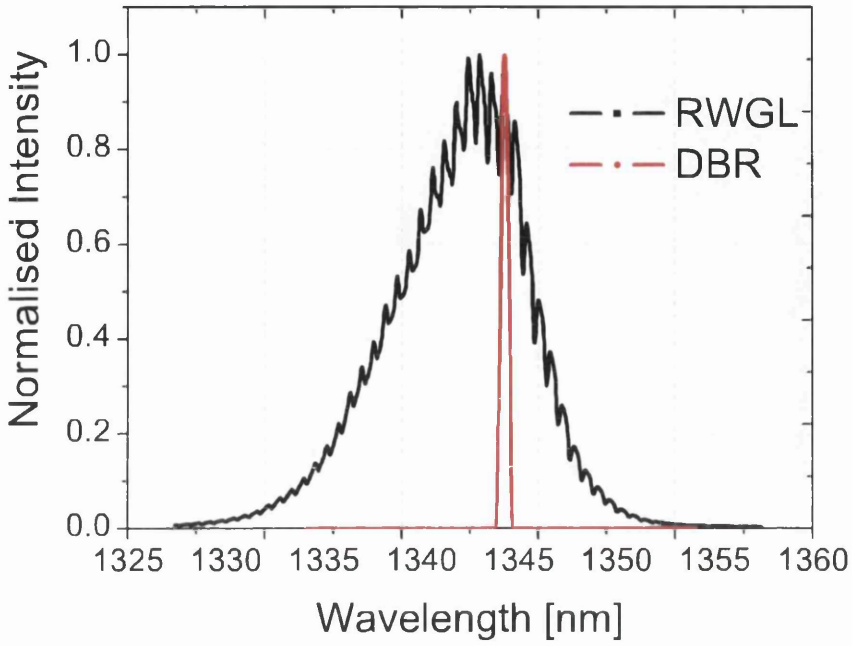

Figure 5.4: Optical spectra of a RWGL (L=420 μm, W=2.5 μm) and a DBR (Λ =210 nm, L_{DBR}=400 μm, L_A=520 μm, W=2.5 μm). Resolution bandwidth = 0.07 nm.

etch depths were initially defined to be the same as for DBR lasers, about 1.7 μm, the majority of the DFB lasers were realised with deeper etch depths, between 1.8 μm and 2 μm, in order to increase the grating effectiveness. This additional etching depth provided a partial compensation to the decrease in the coupling coefficient caused by imperfect etching inside the gratings. Testing of these devices was conducted CW on a copper heat sink, using the same setup as for DBR lasers.

5.2.1 Lasing characteristics

Lasers showed stable single-mode operation between 12.5 °C and 25 °C, up to three times the threshold current I_{th}. Fig. 5.6 shows a plot of the output power as a function of injected current for a 210 nm period, 1 mm long DFB laser, which shows a threshold current of 55 mA, at 15 °C. Fig. 5.7 shows an optical spectrum

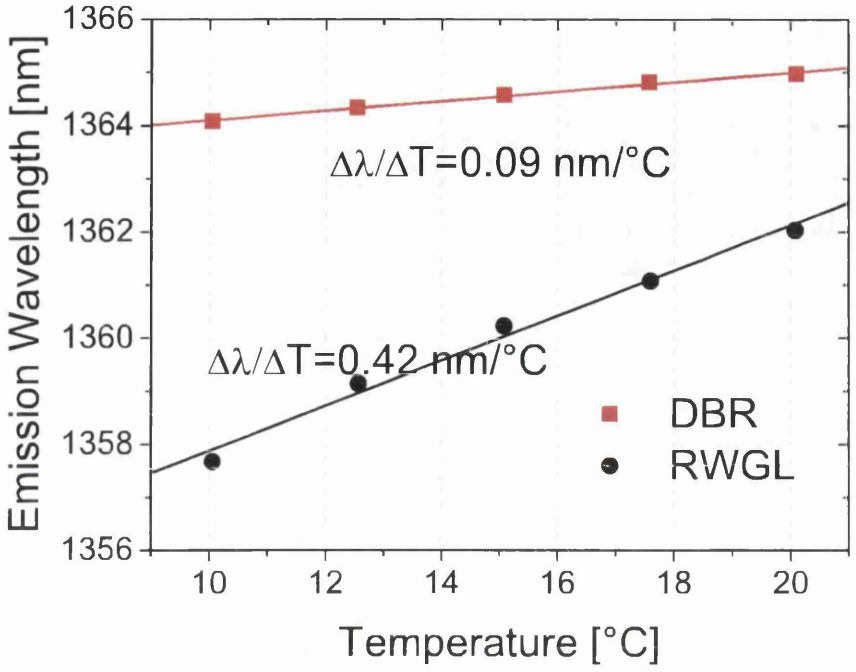

Figure 5.5: Wavelength vs. temperature dependence curves for a RWGL and a DBR (same devices as in Fig. 5.3).

taken at 12.5 °C and $2.5I_{th}$ for the same device, which demonstrates a high SMSR of more than 40 dB. This is a state-of-the art result for surface grating DFB lasers [Wang 05a]. A result from DFB lasers, fabricated on the same sample, having 1.6 nm period spacing is plotted in Fig. 5.8. It shows that periods of 210 nm and 211.6 nm give lasing wavelengths spaced by 10 nm, which perfectly agrees with the original design (3.3). Another result came from the fabrication of several batches of DFB lasers: it was established that the tolerance on the absolute grating period is around 1 nm.

Fine tuning by varying the operation temperature and the driving current were also assessed, giving values that are very similar to the expected 0.09 nm/°C that was measured for DBR lasers.

Recalling that the stop-band width is related to the κL product (section 2.3), the value of kappa can be estimated from the stop-band width of those DFB lasers

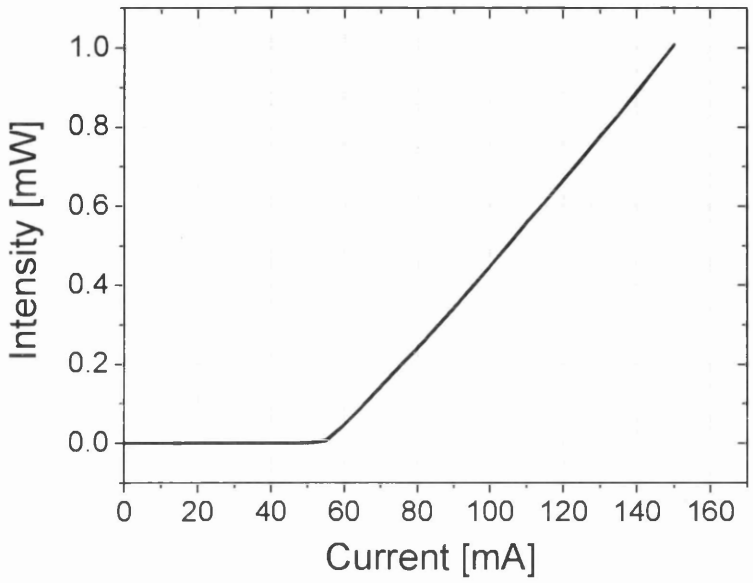

Figure 5.6: L-I characteristic of a typical single-mode DFB laser, with period Λ=210 nm, L=1 mm, and recess(w)=500 nm, etch depth h= 2 μm.

which were designed to be single-mode, but which lase on both sides of the stop-band, due to the fact the mode degeneracy had not been removed by the phase condition at the facet. Thanks to the fact that some lasers showing this behaviour were found on the fabricated samples, their spectra were used to estimate κ of the corresponding sample (assuming an uniform yield of the dry-etching process). By using the approximation $\Delta\beta L \approx 2\kappa L$, since the stop-bands were found to be 0.43 nm and 0.76 nm for a 1.89 μm deep and for a 2 μm deep sample respectively, their κ value was estimated to be 25 cm^{-1} and 42 cm^{-1} respectively.

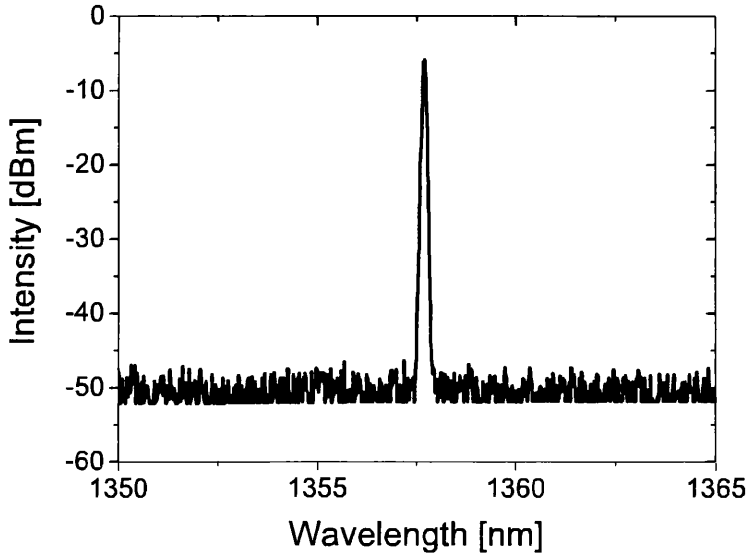

Figure 5.7: Optical spectrum of a typical single-mode DFB laser, with period Λ =210 nm, L=1 mm, and recess (w)=500 nm, etch depth h= 2 μm. Resolution bandwidth = 0.07 nm.

5.3 Conclusions

Results from testing of single-mode devices were reported. DBR lasers having 210 nm period and 1.68 μm etch depth, with 520 μm long active section and 400 μm long grating section, showed effective single-mode operation, with I_{th} around 70 mA. The coupling coefficient of these devices was estimated to be 8 cm^{-1}, lower than predicted due to shallow etching of the gratings. A comparison of the DBRs versus RWG lasers fabricated on the same sample demonstrated the effectiveness of the periodic structure in reducing the laser spectrum from multi-mode (Fabry-Perot) to single-mode (DBRs). Moreover, temperature tuning assessment gave a reduced dependence of the DBRs (0.09 nm/°C) with respect to the RWGLs (0.42 nm/°C), confirming the effectiveness of the Bragg grating. Single-mode DFB lasers were also fabricated and tested. They had different periods (210 and 211.6 nm), lengths (from 600 to 1000 μm), and etch depths (from 1.8 to 2 μm). The coupling

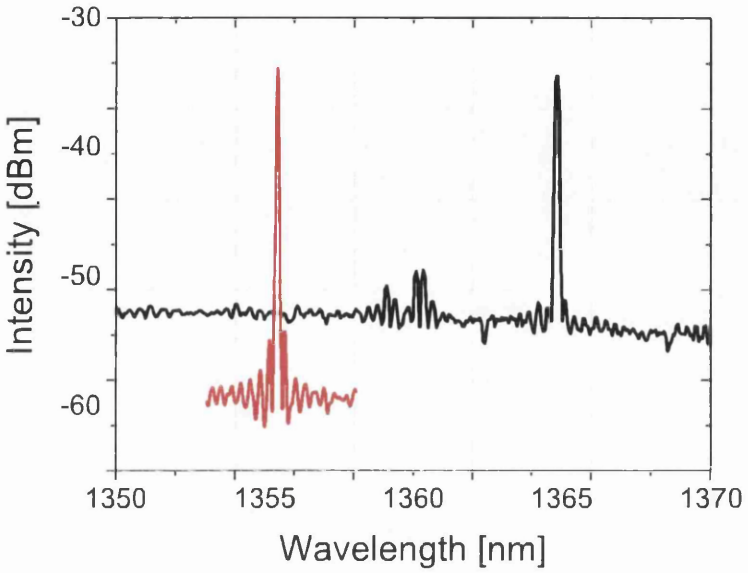

Figure 5.8: Optical spectra of DFB lasers: (red) a 210 nm period laser at 182 mA, (black) a 211.6 nm period laser at 192 mA. Resolution bandwidth = 0.07 nm.

coefficient was estimated to be 25 cm^{-1} and 42 cm^{-1}, for 1.89 μm and 2 μm deep DFBs respectively. Due to the higher κ, best performing devices were the 2 μm deep DFB lasers; low threshold currents of 55 mA and SMSR higher than 40 dB were recorded with 1 mm long devices. It was experimentally confirmed that a 1.6 nm variation of the grating period induces a 10 nm variation over the lasing wavelength. From testing of DFB lasers belonging to different batches, it was also observed that the EBL reproducibility of the grating period, from one run to another, can vary by up to about 1.5 nm.

Chapter 6

Dual-wavelength lasers

After demonstrating the feasibility of DBR and DFB lasers with the lateral grating structure, dual-wavelength DFBs were fabricated. Alongside the new dual-mode sources, three section DFB lasers were defined, to allow comparison with them. In this Chapter, results on the optical assessment of the novel dual-wavelength structure, such as L-I curves and optical spectra, are reported. In order to gain a deeper understanding on the device performance, other device characteristics were also carefully investigated, namely transversal mode distribution, four wave mixing, and injection locking behaviour. Finally, preliminary results from the assessment of the three-section lasers are reported.

6.1 Lasing characteristics

In order to gain as much information as possible, the double-grating DFB lasers were fabricated varying several geometrical parameters of the structure. The difference in period between the two gratings was varied from 0.1 nm to 1.6 nm, different etching depths were defined between 1.8 μm and 2 μm, and the cavity length was chosen in the range from 750 μm to 1.5 mm, to compensate for the low coupling factor κ.

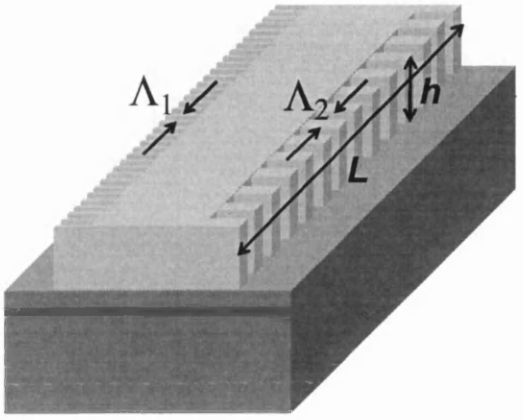

Figure 6.1: Schematic of the dual-wavelength laser, showing the design parameters.

Testing was conducted under CW conditions, with the laser chips mounted on a copper heat sink.

Light-Current characteristics were acquired using the same set-up employed to test the single-mode lasers (see section 5.1.1). Although a few batches of devices were fabricated, with different etch depths and grating periods, the double-grating DFBs which showed good dual-mode operation were all part of the same batch. These devices were designed with a 2.5 μm wide waveguide and a 0.5 μm recess, and the ridge was etched to 1.89 μm. The yield of the process was about 8 working devices (some of which were damaged during testing) out of 24 dual-wavelength lasers fabricated on the same sample. The results presented in this chapter were thoroughly collected between 4 of these devices, and they are very consistent among the tested lasers.

Typical values of the threshold current I_{th} are between 40 mA and 50 mA for 1.2 mm and 1.5 mm long devices at 15 °C. Fig. 6.2 shows a typical L-I curve up to $2I_{th}$.

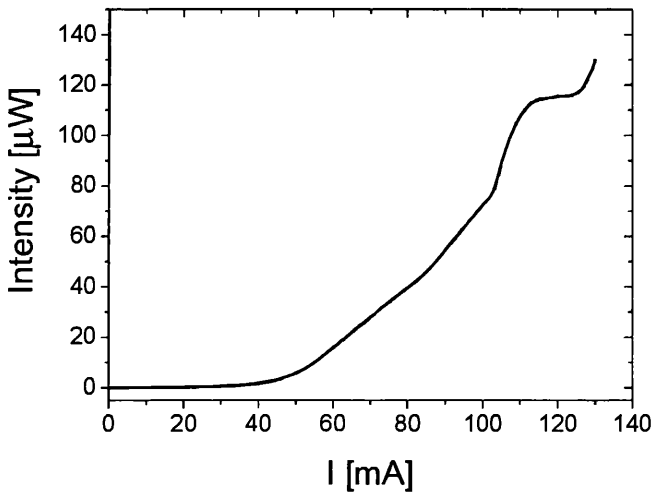

Figure 6.2: Light-Current (L-I) characteristic for a 1.2 mm long dual-wavelength DFB laser.

6.1.1 Optical spectra

Optical spectra were inspected using the Agilent OSA (0.07 nm resolution). As soon as the current crosses the threshold value, two lasing modes appear around 1347 nm, separated by 0.15 nm. The intensity of the mode at shorter wavelength is slightly higher up to current values of 100 mA, after which the two modes oscillate with the same intensity. Stable dual-wavelength lasing operation, with side mode suppression ratio around 28 dB, was observed in the range 100-150 mA of injected current. Fig. 6.3 shows a typical spectrum at twice I_{th}.

The emission wavelengths of the two modes were measured with higher accuracy by using the optical heterodyne method [Baney 98]. For devices with grating period difference $\Lambda_2 - \Lambda_1 = 0.07$ nm, λ_1 and λ_2 were found to be 1346.32 nm and 1346.47 nm, yielding a measured wavelength spacing of 0.15 nm. This value is in good agreement with the expected 0.16 nm spacing given by the formula

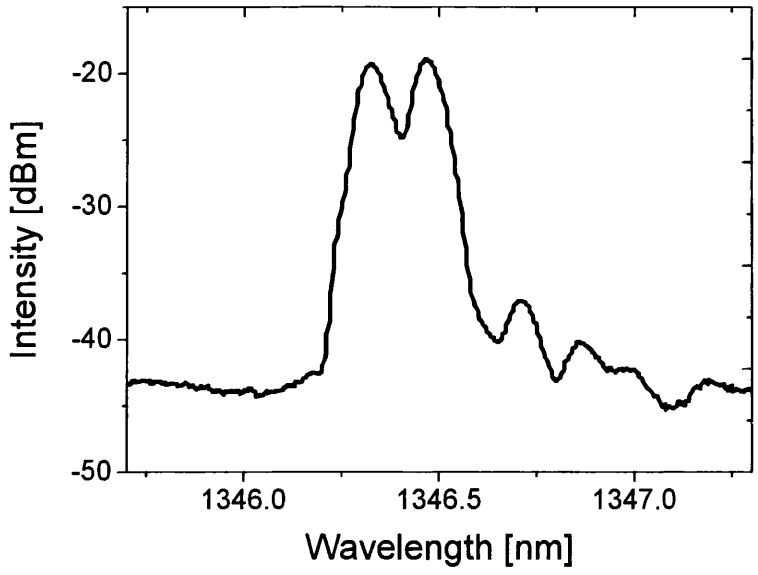

Figure 6.3: Optical spectrum from a dual-wavelength DFB (Λ_1= 1346.32, Λ_2= 1346.47), at $2I_{th}$. Resolution bandwidth = 0.07 nm.

[Möhrle 01]:

$$\lambda_1 - \lambda_2 = \mid \Delta\Lambda - \Delta_S \mid \tag{6.1}$$

where the detuning $\Delta\Lambda = 2n_{eff}(\Lambda_2 - \Lambda_1)$ is 0.45 nm and the stop-band width Δ_S is measured from the spectrum and it is 0.29 nm. A depiction of this situation is shown in Fig. 6.4.

From the measured Δ_S value the coupling coefficient κ was estimated to be 16 cm^{-1}. It is interesting to note that $\kappa < 25$ cm^{-1}, where 25 cm^{-1} is the coupling coefficient of the single-mode DFBs that were fabricated alongside this dual-mode device, on the same sample (section 5.2.1). This result is explained by the fact that in the double period DFB each periodicity is defined only on one side of the RWG. Nonetheless $\kappa > 25/2$ cm^{-1}, since each λi mode receives some feedback from the other grating, due to the small detuning between λi and Λ_j.

Although the emitted light was expected to be transverse-electric (TE) polarised,

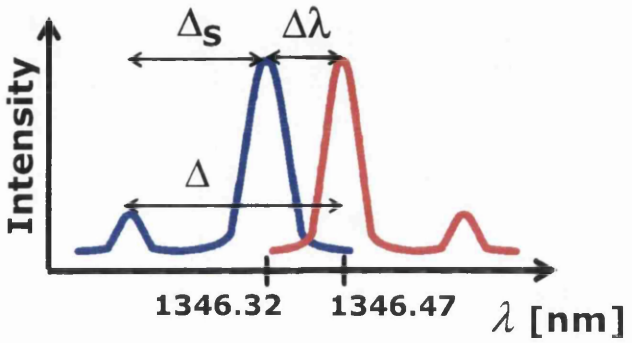

Figure 6.4: Schematic of the modes of the dual-wavelength laser.

for completeness, due to the novelty of the device, the state of polarisation was assessed using a Glan's cube. The TE signal was 99.5 μW, while the TM was only 4.35 μW, which confirmed the initial assumption. This result is important in that it maximises the efficiency of microwave generation when heterodyning the two signals.

6.1.2 Transversal mode distribution

A very interesting feature observed on these new dual-wavelength lasers is that the two longitudinal modes do not fully spatially overlap along the transversal direction. In fact, by displacing an optical fibre along the transversal x-axis, as shown in Fig. 6.5, it was observed that the optical spectrum varied as a function of the fibre position, as shown in Fig. 6.6.

Note that the zero position X_0 along the x-axis was set by maximising the power of the background level, and this condition corresponded indeed to that of the two modes having the same intensities. From the geometry of the device, it was also possible to establish on which side of the ridge each mode was located.

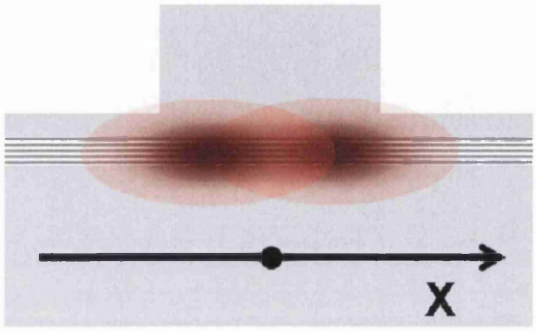

Figure 6.5: Schematic of the dual-wavelength laser, showing the x-axis orientation.

The result, which is illustrated in Fig. 6.7, was that the i mode is confined in the region underneath the j grating. This can be explained by recalling that the DFB structure is a distributed feedback reflector, hence, since in the Λ_i region the i mode is strongly reflected in the backward direction, on that side of the waveguide a weaker i mode is detected, and vice versa.

In order to have a better grasp of this effect, a more accurate set of data was collected by moving the micropositioner by steps, and collecting the emitted power per each mode. Fig. 6.8(top) shows the plotted data, as they were acquired in a dB scale, while a more interesting picture appears when the data are converted into a linear scale, as it can be seen in Fig. 6.8(bottom). The linear scale clearly shows the Gaussian distribution of the modes.

6.1.3 Four-wave mixing

By inspecting the spectra of some dual-wavelength lasers on a large wavelength span, it was observed that when the driving current was increased (above 130 mA, for dev2), two new sets of modes appeared at 1341 nm and 1351 nm. These sets were located at about 5 nm from the two main lasing modes (Fig. 6.9).

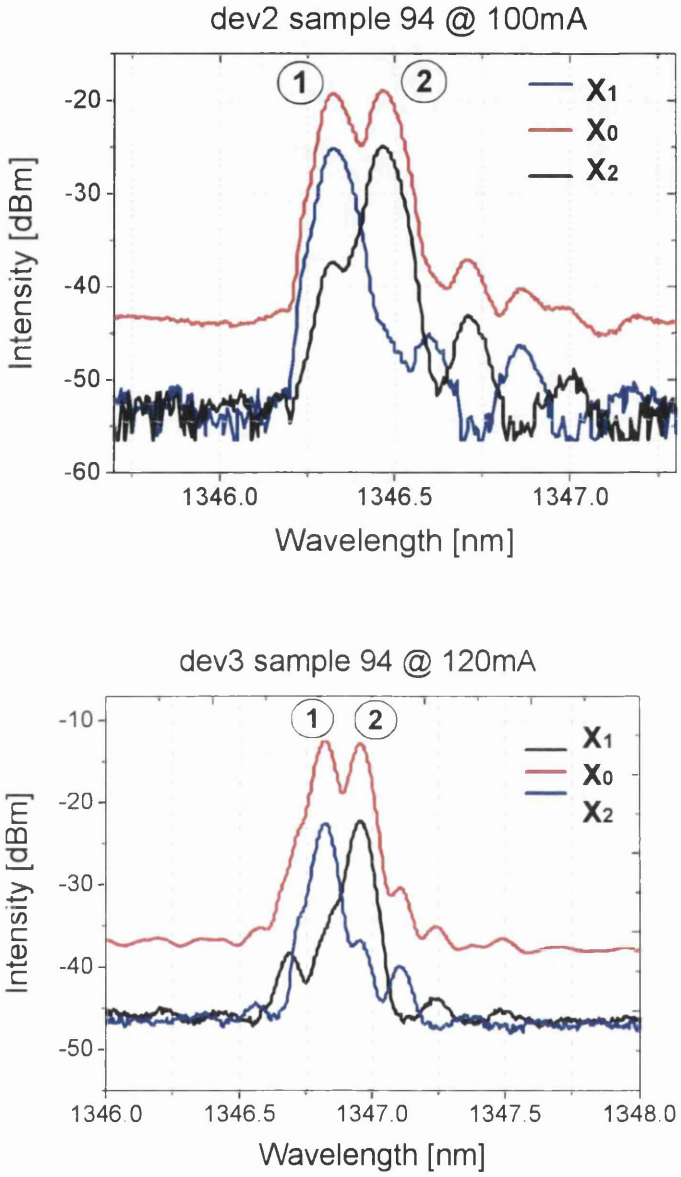

Figure 6.6: Typical optical spectra of dual-mode lasers, taken at different x positions: X_0 corresponds to the centre of the RWG, while $X_{1,2}$ are at the sides of the RWG. Resolution bandwidth = 0.07 nm.

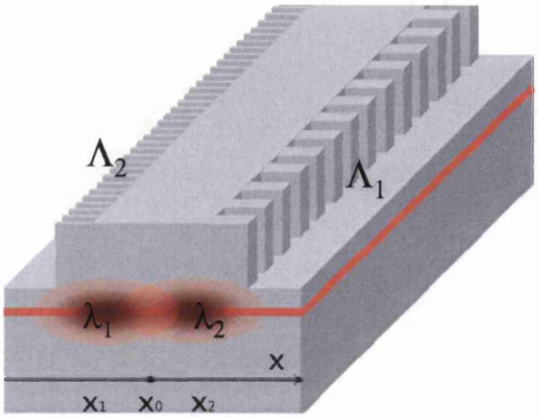

Figure 6.7: Schematic of the dual-wavelength laser, showing the location of the λ_i mode and of the Λ_i period.

Interestingly these modes did not show the spatial off-set previously reported. When moving the fibre along the x-axis, the two main modes at 1346 nm showed partial overlap, while the relative intensities of the modes at 1341 nm and 1351 nm did not vary (Fig. 6.9). This result suggests that the new sets of modes are originated by a single transversal mode, and that they are not affected by the asymmetrical periodicity of the structure. Also, their symmetrical position with respect to the main lasing modes suggests some type of four-wave mixing (FWM, or 4WM) effect, which was recently reported in other single-cavity two-mode lasers [Hoffmann 04b] and in [Wilk 07]. A deeper understanding of this phenomenon would require additional device characterisation that would go beyond the scope of this work.

6.2 Photo-mixing experiments

In order to assess the capabilities of the dual-wavelength DFB laser for mm-wave generation, photo-mixing of the two modes was performed. The experiment was carried out by heterodyne mixing of the optical modes onto a fast photodiode (New

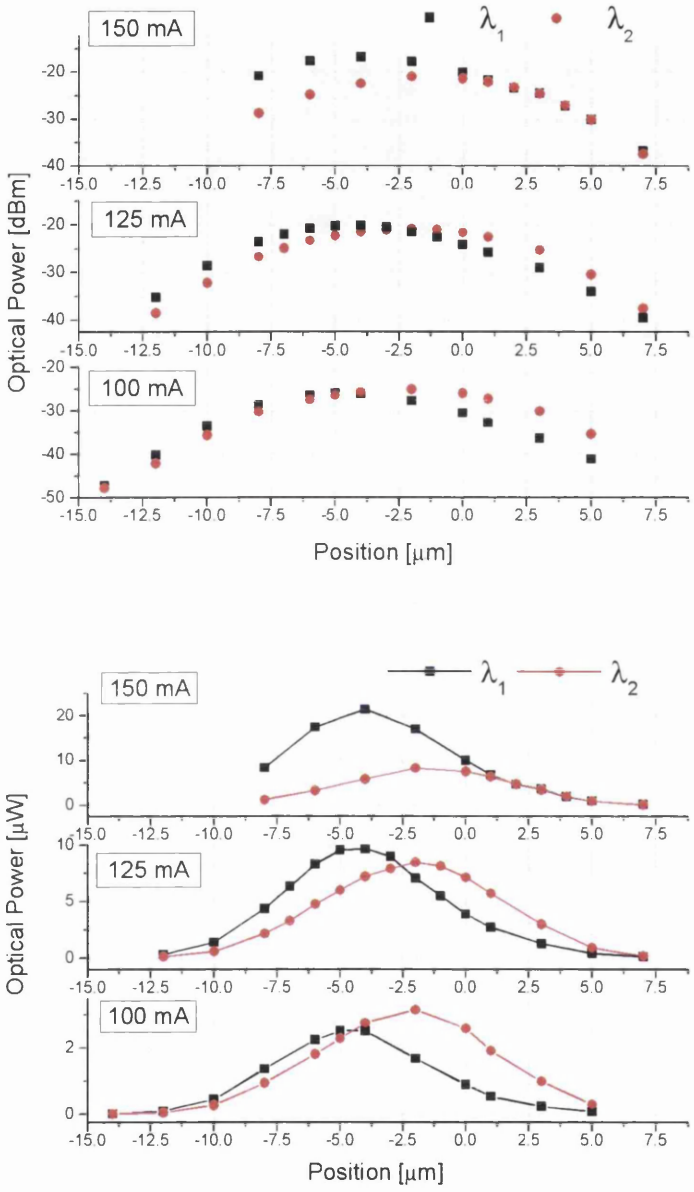

Figure 6.8: Plot of the peak power of each mode, at different positions of the lensed fibre: (top) in the acquired dB data, (bottom) converting into linear scale (dev12).

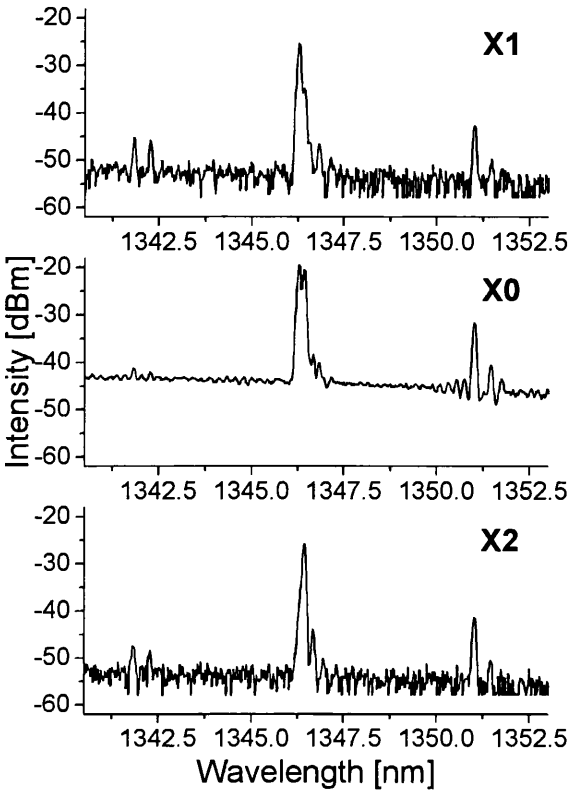

Figure 6.9: Spectra of a dual-mode laser taken at different x positions, using a broad span on the OSA, showing two sets of lateral modes. Resolution bandwidth = 0.07 nm.

Focus IR Photodetector, Model 1014, 45 GHz, (950-1650) nm), previous optical amplification (of around 10 dB) by a semiconductor optical amplifier (SOA). The electrical signal generated on the detector was then acquired using an RF spectrum analyser (40 GHz Agilent). Fig. 6.10 shows a schematic of the set-up used for this measurement.

The result was a beat mode signal at 22.5 GHz, as shown in Fig. 6.11, which confirmed indeed the 0.15 nm optical spacing reported above, when using the formula $freq = c\frac{\Delta\lambda}{\lambda^2}$.

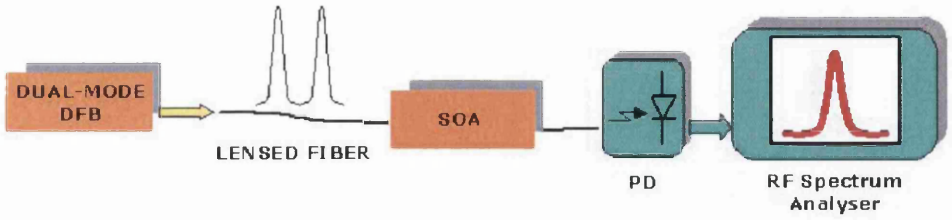

Figure 6.10: Schematic of the set-up used for the photo-mixing experiments.

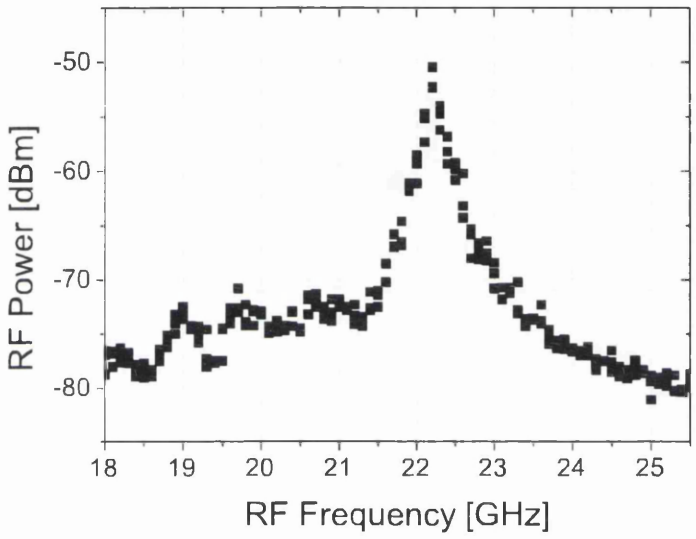

Figure 6.11: Measured RF spectrum of the beating between the two modes. Span = 3 GHz, resolution bandwidth = 1 MHz.

Typical RF power levels were in the range of -50 dBm, much lower than what was expected. Hence, the conversion efficiency was estimated by using the formula for the electrical power generated by photomixing [Donati 99]:

$$P_{el} = R(\sigma P_{opt})^2 \tag{6.2}$$

where R is the load and σ is the detector responsivity. Since in the present experiments $R = 50\ \Omega$ and the optical power was around P_{opt}= 0 dBm, the responsivity σ was estimated to be 0.02 A/W. It follows that the responsivity of the photodiode is a major limitation to the maximum achievable RF power, as it is

evident from Fig. 6.12.

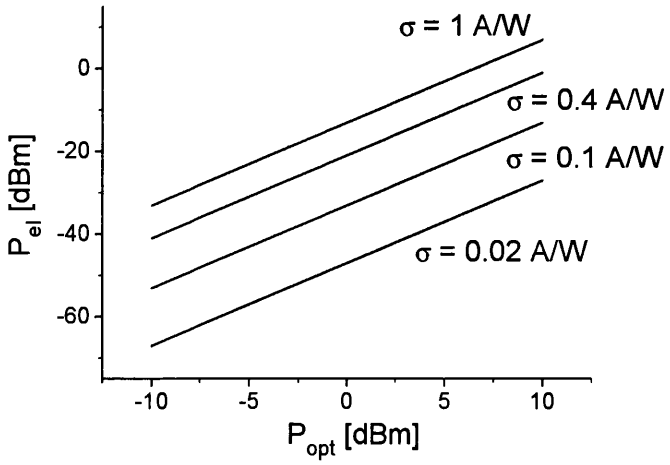

Figure 6.12: Electrical power generated by photomixing as a function of the detected optical power, for a 50 Ω load, for different photodetector responsivities.

In order to estimate the stability jitter of the generated microwave signal, measurements were performed setting different integration times, as it was reported in [McIntosh 95]. Comparison of the beat signal linewidth measured from RF spectra taken on different time-scales (the shortest sweep was 200 ms and the longest one was 60 s), gave a very small increase in the linewidth of the beast signal, from 65 MHz to 85 MHz, confirming that the single-cavity structure allows for the generation of very stable beat signals.

6.2.1 Tuning

The RF frequency generated by photo-mixing is given by the separation between the two optical modes, which are defined by the grating periodicity, hence it is predicted to be very small. However, due to interest in the potential for fine tuning, the effects of current and temperature tuning were assessed on the new devices. Results are reported in Fig. 6.13. As expected, by varying the temperature of

operation, both wavelengths were affected in the same way, hence the microwave frequency was almost constant over the inspected range of temperatures. This result confirms once more the very good stability performances expected from the single-cavity structure.

On the other hand, current tuning produced a different effect on each mode, causing a larger variation over the RF frequency. This result is probably due to a slight asymmetry in the current injection, which might be caused by a very small shift of the contact window with respect to the centre of the ridge WG. This feature could be conveniently exploited as a very fine tuning mechanism.

6.3 Linewidth measurements

The linewidths of both separate modes were assessed by the optical heterodyne technique [Baney 98]. This consists in beating the optical signal under test with a very narrow single-mode laser. In these experiments the signals were sent each through one input channel of a 50%-50% optical fibre-coupler (Fig. 6.14), and the output was connected to a photodetector (45GHz New Focus), followed by the RF spectrum analyser.

The narrow line source used in this work is a commercial 1.3 μm tunable laser (HP 8167B), with 1 MHz linewidth. A typical RF spectrum acquired using this technique is shown in Fig. 6.15. The full width at half maximum (FWHM) linewidth of the separate modes was then estimated through fitting the detected spectra with a Lorentzian function. From this assessment, typical linewidths were found to be in the range between 110 MHz and 60 MHz.

In order to allow a comparison between the modal linewidths of both separate modes and of their beat signal, the same measurement was carried out at different current injection levels on both signals. The result is plotted in Fig. 6.16.

From this graph it appears that both curves show the typical inverse dependence of the linewidth with respect to current level, which is expected from the

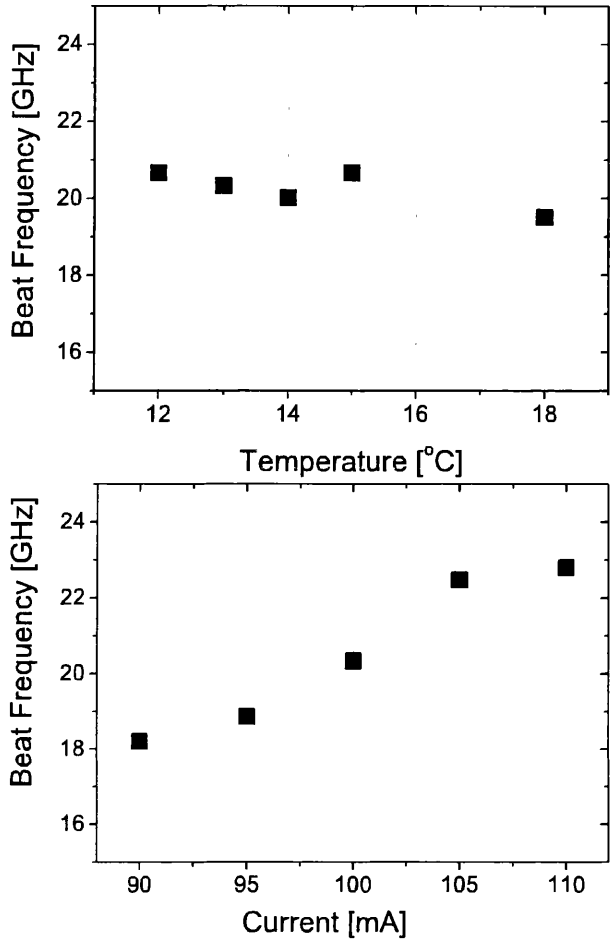

Figure 6.13: Effect of tuning on the frequency of the beat signal: with respect to temperature (top); with respect to current (bottom).

Henry law (section 2.26). However, the plot shows that while the linewidth of the separate modes decreases modestly with respect to the injection level, the linewidth of the beat signal shows a much stronger reduction. Note that the linewidth of the other optical mode, which is not shown in the plot, is of the same order as the one shown, and it has the same dependence over current injection. In order to confirm this result, the same measurement was carried out on a different device, showing the same trend (Fig. 6.17). These results confirmed what was expected from the discussion given in par 3.4.1: modes lasing within the same cavity are

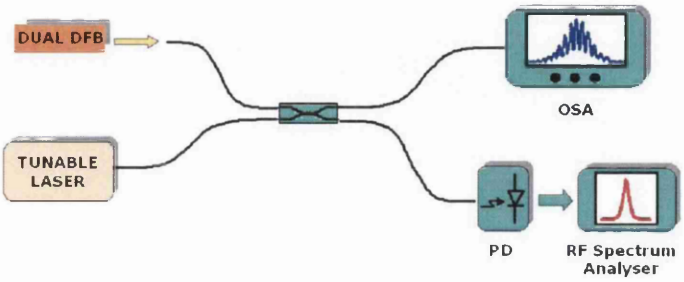

Figure 6.14: Schematic diagram of the optical hetorodyne technique, showing the experimental set-up used for the linewidth measurement.

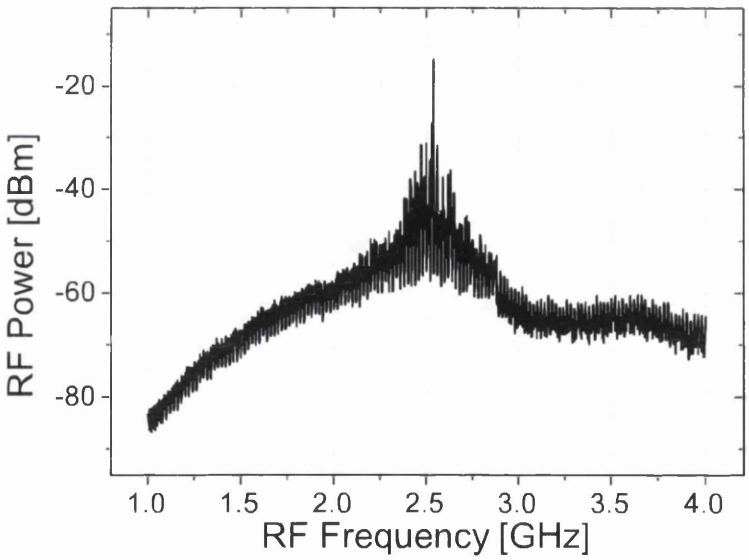

Figure 6.15: A typical RF spectrum detected using the optical hetorodyne technique. Span = 3 GHz, resolution bandwidth = 300 kHz.

subjected to common-mode-noise rejection effects, although they are not as strong as in microchip lasers.

The most likely explanation for this phenomenon is that there is some sort of

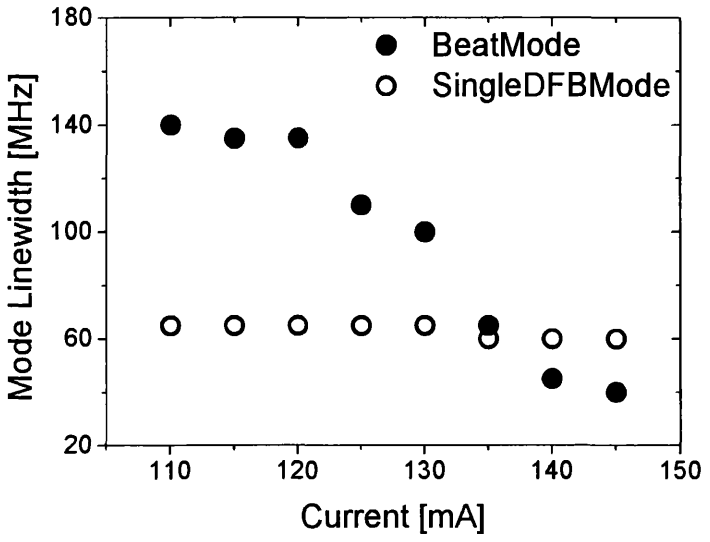

Figure 6.16: Mode linewidth as a function of the current injection, for one of the two modes (◇), and for the beat signal (○).

coupling between the two modes, which builds up as the current level is increased. The relation between the two modes depends on their degree of spatial overlap: at low injection levels and for a small overlap, they behave as independent lasers while, as the current is increased, a correlation builds up due to increased modal overlap. This phenomenon is likely to be linked to the way the modes share the carrier population [Valle 95].

6.4 Optical injection experiments

Optical injection locking experiments were performed on the two modes, using the commercial 1.3 μm tunable laser. The device under measurement was connected to the output of a 2x1 fibre-coupler, while the tunable laser and the OSA were coupled to the two input ports (Fig. 6.18).

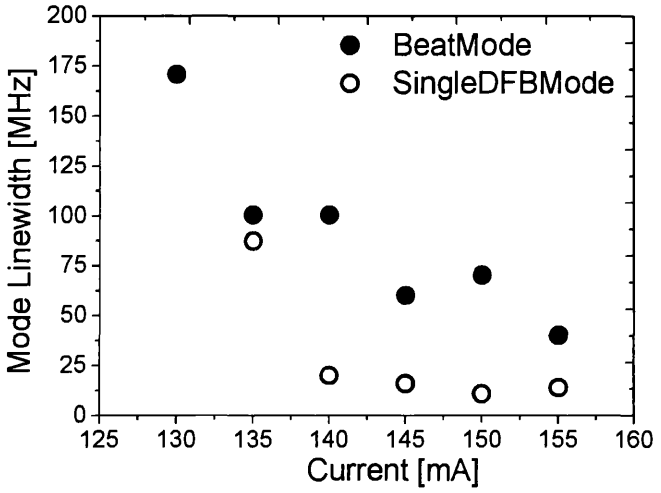

Figure 6.17: Mode linewidth as a function of the current injection, for one of the two modes (◇), and for the beat signal (○), on device 3.

At low current levels, it was observed that when mode 1 was injection locked the intensity of mode 2 remained unaffected, and vice versa (as they are labelled in Fig. 6.6). However, at higher driving currents, when one mode was injection locked the power of the other decreased. This result suggests that at low driving currents the two wavelengths are generated by substantially uncoupled transversal modes, however as the current is increased the modes start to affect one another, hence they couple between themselves. This behaviour confirms the previous observations about a carrier coupling effect taking place in the common cavity.
Injection experiments on the small side-modes immediately adjacent to the two main lasing ones seemed to confirm this effect. However, due to their low intensity, the effect was not as evident as on the two main modes.

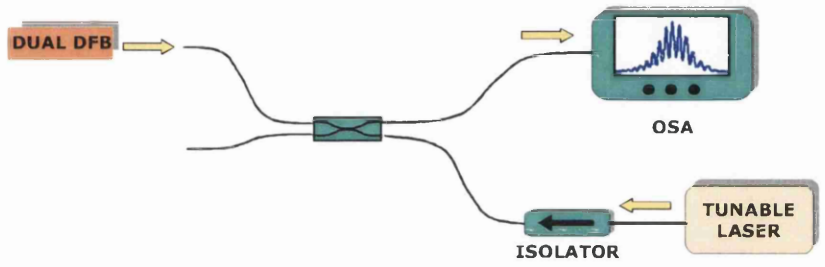

Figure 6.18: Schematic diagram of the set-up employed for the optical injection experiment.

6.5 Comparison of the proposed laser with other dual-wavelength lasers

Three section DFB lasers, similar to those reported by [Möhrle 01], were also fabricated alongside the double-grating devices, to allow a comparison in terms of photo-mixing performances. The geometry of the devices is shown in Fig. 6.19. They are basically two separate single-mode DFBs coupled through a simple RWG section, to allow adjustment of the phase difference between the two modes. Lengths were varied in the range of 600-750 μm for the laser cavities and 200-400 μm for the phase section, and periods were the same as for the dual-wavelength devices. Final devices were cleaved at both ends to allow assessment of both lasers. The two DFB sections were independently driven, while the phase section was

either reverse biased or forward biased, to bring it to transparency. Assessment of these sources did not lead to significant results, since few devices proved to be able to emit two wavelengths simultaneously, and even in that case the lasing performance was quite poor. This result is probably due to the fact that the two wavelengths were very close to each other, so that they locked to each other when they were mutually injected.

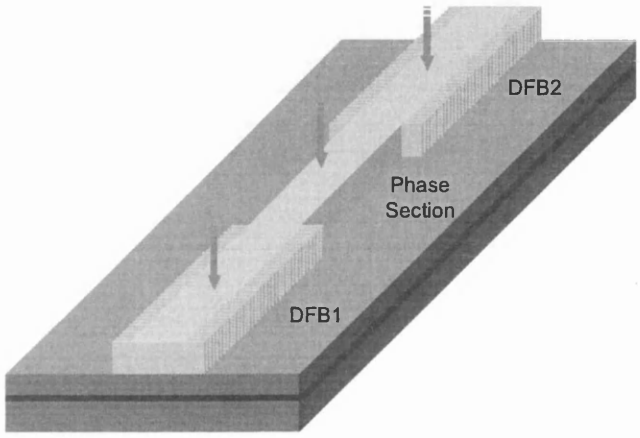

Figure 6.19: Schematic of the fabricated three-section DFB lasers.

6.6 Conclusions

Results from testing of novel dual-wavelength DFB lasers, defined with two gratings, one on each side of the RWG, were reported. Stable dual-mode emission in CW operation was recorded from devices with a period spacing of 0.07 nm, and an etch depth of 1.89 μm. The 1.2 mm long lasers showed a very low I_{th} of 40 mA, and SMSR around 30 dB. The emitted wavelength were carefully measured using an optical heterodyne technique, yielding a measured wavelength spacing of 0.15 nm, which was shown to agree very well to the design parameters. The coupling

coefficient of these devices was estimated to be around 16 cm^{-1}, in good agreement with the κ measured on single-mode DFBs (Chapter 5). A characteristic feature of the dual-wavelength DFB lasers was the partial spatial overlap of the transversal mode distributions. Photo-mixing experiments were reported, at around 23 GHz, to show the potential of the device for the generation of microwave signals. From these results it was demonstrated that much stronger RF signals could be achieved by employing a commercial detector with higher responsivity. Assessment of the linewidths of both the separate modes and of the beat signal showed that the beat signal linewidth experienced a much stronger decrease as the injection current was increased. This result confirmed the benefit given by the common cavity. External optical injection experiments were also performed, confirming that the two modes are independent at low injection level, while a mode coupling builds up as the current level is increased.

Chapter 7

Conclusions and Future Work

This work was concerned with the realisation of single- and dual-mode Bragg grating lasers for generation of signals in the FIR to microwave region.
The design and processing required to define lateral grating structures was implemented, and its potential in fabrication of DBR and DFB lasers was shown. The same structure was successfully used to realise a novel dual-wavelength device. This source was thoroughly investigated, and its potential for generation of microwave signals was demonstrated.

7.1 Conclusions on single-mode lasers

Fabrication of several batches of single-mode DBR and DFB lasers was carried out. Assessment of these devices showed that the lateral grating structure is effective in guaranteeing stable single-mode operation, at room temperature, with SMSR larger than 40 dB. These results demonstrated that the technology here implemented is reliable, with a tolerance on the absolute value of the grating period of around 1 nm.
Assessment of the tuning behaviour of these devices showed the feasibility of very fine tuning by temperature change, however it also showed that it is difficult to achieve the optimum tuning condition using QWI alone, since the bandgap shift

could not be easily controlled. Very accurate control over the bandgap shift has to be achieved to allow efficient and broad wavelength tuning by carrier injection. SEM inspection of the fabricated gratings showed that the pitch is not properly defined at the bottom of the waveguide, where it couples to the propagating mode. This lack of accurate control over the etch depth causes a reduction of the coupling coefficient with respect to the designed value, and therefore it affects the performance of the laser.

A substantial decrease in threshold current was achieved in the course of the research, in particular through increases in the grating etch depth, and demonstrated that a major improvement in the fabrication quality had been achieved. The measured results on single-mode DFBs were in line with state-of-the-art devices reported in the literature [Wang 05a].

7.2 Conclusions on dual-mode lasers

A novel dual-wavelength laterally coupled DFB laser, with two grating periods, one on each side of the ridge waveguide, was realised. Stable emission of two longitudinal modes, whose spacing was defined by the difference in Bragg periods, was observed in CW operation, with very low threshold currents. Careful assessment of their spectra showed that the transversal distributions of the two modes does not fully overlap in the horizontal direction.

In order to explore the potential of the double grating DFBs for the generation of microwave signals, photo-mixing experiments were performed. These measurements proved the capability of generating signals in the GHz region, at the designed frequency difference. Taking into account the limited responsivity of the detector employed in the measurements, these results look very encouraging, since it was shown that by using an improved detection scheme it is possible to produce much higher GHz or THz power level. Assessment of the generated beat frequency at different time spans showed a very stable signal, and this result was confirmed by

testing under different temperature conditions, which showed a variation of the generated frequency below 5%. Current tuning was assessed, showing the potential for very fine tuning of the microwave signal.

Another interesting result was given by assessment of the linewidths of both the separate modes and of the beat signal. Although all the linewidths decreased when the driving current was increased, as it is predicted by the Henry's law, it was found that the linewidth of the beat signal had a stronger decrease as the injection current was increased. This result was explained by the fact that when the carrier concentration increased the mode overlap increased as well, hence a correlation between the two modes built up, causing the strong reduction of the beat signal linewidth. The finding confirmed once more the benefits resulting from the simultaneous oscillation of the two modes inside the same laser cavity.

In order to further investigate the characteristics of the two modes, external optical injection experiments were performed. This assessment confirmed what was previously found from the linewidths measurements: at low injection level the two modes are independent, while as the driving current is increased a mode coupling builds up.

7.3 Suggestions for future work

In order to gain a clearer understanding of the features discovered in the novel DFB structure, it would be useful to fabricate more dual-wavelength devices, having different waveguide widths, to explore how the degree of spatial overlap can affect the device performances, and with larger wavelength spacings.

In order to achieve better performances, it is important to optimise the effectiveness of InP dry-etching, to ensure proper definition of the later grating structure.

Finally, in order to address the need for broader frequency sources, a structure comprising two DBR gratings should be developed.

Appendix

A1 Optical gain in semiconductors

Defining the real electric field as $\mathbf{e}(x, y, z)$, this can be described in terms of its complex amplitude $\mathbf{E}$ as [Buus 05]:

$$\mathbf{e}(x, y, z) = Re\{\mathbf{E}\exp(j\omega t)\} \tag{7.1}$$

Assuming a TEM wave propagating along the z direction of propagation of light, i.e. a uniform plane wave such that $\mathbf{E} = E(0, E_y, 0)$ and $\mathbf{H} = H(H_x, 0, 0)$, it can be written:

$$E_y = E_0 \exp(-j\beta z) \tag{7.2}$$

where $E_0 = E_y(z = 0)$.

Since in an isotropic and nonmagnetic medium $\nabla \times \mathbf{E} = -j\omega\mu_0\mathbf{H}$, it follows:

$$H_x = -\sqrt{\frac{\epsilon}{\mu}}\, nE_y \tag{7.3}$$

The average power per unit area I (intensity) is:

$$I = \overline{\mathbf{e} \times \mathbf{h}} = \frac{1}{2} Re\{E_y \cdot H_x^*\} \tag{7.4}$$

by substituting we get:

$$I = \frac{c\epsilon_0}{2} n' |E_0|^2 \exp(2k_0 n'' z) \tag{7.5}$$

Defining $I_0 = \frac{c\epsilon_0}{2} n' |E_0|^2$ we can simplify the previous equation to:

$$I = I_0 \exp(2k_0 n'' z) \tag{7.6}$$

It is clear that for $n'' > 0$ I increases, and vice versa. From this the optical gain g, or loss α, can be defined:

$$g = -\alpha = \frac{1}{I}\frac{dI}{dz} \tag{7.7}$$

Let us now consider a semiconductor heterostructure, where we define the propagation constant $\beta = n_{eff}k_0$ (n_{eff} is the effective refractive index of the propagating mode, k_0 is the free-space propagating constant) and a confinement factor Γ. Gain and loss in the active layer are accounted by letting n be complex:

$$n = n' + in'' \tag{7.8}$$

where the active layer (power/intensity) gain g_a is related to the imaginary part of n through $g_a = 2k_0n''$. For the case of modest refractive-index difference, it can be shown that the wavelength dependent modal gain is given by $g_{eff} = \Gamma g_a$. The net modal gain is given by:

$$g_{net} = g_{eff} - \alpha_i \tag{7.9}$$

Introducing the *end loss*, or mirror loss, of the cavity $\alpha_m = \frac{1}{2L}\ln\frac{1}{R_1R_2}$ and the cavity round-trip gain $g_c = g_{net} - \alpha_m$, and recalling the oscillation condition for a FP laser:

$$r_1 \cdot r_2 \exp(-2i\beta L) = 1 \tag{7.10}$$

we find the gain condition $g_c = 0$, that is:

$$\Gamma\, g_a - \alpha_i - \alpha_m = 0 \tag{7.11}$$

By defining:

$$\alpha_{tot} = \alpha_i + \alpha_m \tag{7.12}$$

one obtains:

$$g_{eff} - \alpha_{tot} = 0 \tag{7.13}$$

A2 Sidemode suppression ratio

The parameter which is generally used to account for the degree of single-mode operation of a laser source is the so-called *sidemode suppression ratio* SMSR, which gives the difference in amplitude between the main spectral mode and the most dominant side mode. The SMSR can be expressed as:

$$SMSR = \frac{\overline{S_N}}{\overline{S_{N+1}}} \tag{7.14}$$

where S_N and S_{N+1} are the photon densities for the main mode N and the next dominant one $N+1$. These can be found by calculating the time-averaged power of the laser modes, using multi-mode rate equations [Buus 05]:

$$\frac{dS_N}{dt} = R_{sp}(\lambda_N + \overline{S_N}\ v_g\ g_c(\lambda_N) \tag{7.15}$$

$$\frac{dS_{N+1}}{dt} = R_{sp}(\lambda_{N+1}) + \overline{S_{N+1}}\ v_g\ g_c(\lambda_{N+1}) \tag{7.16}$$

where $R_{sp}(\lambda_i)$ is the spontaneous emission rate. Note that under stationary conditions Eqs. 7.15 and 7.16 are both equal to zero.

Since the spontaneous emission spectrum is very broad, and the two modes N and $N+1$ are neighbouring ones, the dependence of R_{sp} over wavelength can be neglected, hence from Eq. 7.16 it follows:

$$\overline{S_{N+1}} = -\frac{R_{sp}}{v_g\ g_c(\lambda_{N+1})} \tag{7.17}$$

By expressing the gain of the $N+1$ mode as:

$$g_c(\lambda_{N+1}) = g_c(\lambda_N) - \delta g \tag{7.18}$$

with the gain difference δg such that $\delta g \gg \mid g_c(\lambda_N) \mid$, Eq. 7.17 becomes:

$$\overline{S_{N+1}} \approx \frac{R_{sp}}{v_g\ \delta g} \tag{7.19}$$

Taking into account the expression for P (Eq. 2.25) and using the expression that relates R_{sp} to the Einstein's coefficient of spontaneous emission n_{sp}:

$$R_{sp} = \Gamma v_g\ g_{eff}\ n_{sp}/V_a \tag{7.20}$$

it is found that, for the case of a laser having two identical facets with reflectivity R, the SMSR is:

$$SMSR = \frac{2P_N \delta g}{h\nu v_g n_{sp} \alpha_{tot} \alpha_m} \tag{7.21}$$

where $\alpha_{tot} \approx g_{eff}$ (see A7.12).

For the case of single-mode operation, since the N mode is dominant, it is possible to approximate P_N to P. By approximating the mode gain around λ_N to a parabola having peak at λ_P:

$$g_{eff}(\lambda_P + \delta\lambda) = g_{eff}(\lambda_P) - b_N \delta\lambda^2 \tag{7.22}$$

it is found:

$$\delta g = b_g \Delta\lambda_m (\Delta\lambda_m - 2 \mid \delta\lambda \mid) \tag{7.23}$$

$$\tag{7.24}$$

for $\mid \delta\lambda \mid < \Delta\lambda_m/2$. Here $\Delta\lambda_m$ is the mode spacing. The SMSR hence becomes:

$$SMSR = \frac{2P_N b_g \Delta\lambda_m (\Delta\lambda_m - 2|\delta\lambda|)}{h\nu v_g n_{sp} \alpha_{tot} \alpha_m} \tag{7.25}$$

In practice, it is found that for typical Fabry-Perot lasers the SMSR is at most 20 dB, while for single-mode laser diodes they can exceed 50 dB.

List of acronyms

AG	as grown
CAD	computer aided design
CB	conduction band
CMRR	common-mode rejection ratio
CW	continuous wave
DBR	distributed Bragg reflector
DFB	distributed feedback
DIAL	differential absorption lidar
DR	distributed reflector
EBL	electron-beam lithography
EC	external-cavity
FIR	far-infrared
FWHM	full width at half maximum
GHz	gigahertz
L-I	light-current characteristic
MMI	multi-mode interference
MBE	molecular beam epitaxy
ML	mode-locked
MOCVD	metal organic chemical vapor deposition
MQW	multi-quantum-well
MS	multi-section

NIR	near-infrared
OIC	optical integrated circuit
OPLL	optical phase-locked loop
OSL	oxide stripe laser
PECVD	plasma enhanced chemical vapor deposition
PD	photodiode
PMMA	polymethylmethacrylate
PhW	photonic wire
PIC	photonic integrated circuit
QCL	quantum cascade laser
QWI	quantum well intermixing
RIE	reactive ion etching
RF	radio frequency
RWGL	ridge waveguide laser
SE	spontaneous emission
SEM	scanning electron microscope
SCH	separate confinement heterostructure
SMSR	sidemode suppression ratio
SOA	semiconductor optical amplifiers
SP	self-pulsating
TE	transverse-electric
THz	terahertz
TM	transverse-magnetic
VB	valence band
VCSEL	vertical cavity surface emitting laser
WDM	wavelength division multiplexing

References

[Abe 95] H. Abe, S. G. Ayling, J.H. Marsh, R. M. De La Rue & J. S. Roberts. *Single-mode operation of a surface grating distributed feedback GaAs-AlGaAs laser with variable-width waveguide.* IEEE Photonics Technology Letters, vol. 7, no. 5, pages 452–454, May 1995.

[Abou-Jaoude 03] R. Abou-Jaoude. *ACC radar sensor technology, test requirements, and test solutions.* IEEE Transactions on Intelligent Transportation Systems, vol. 4, no. 3, pages 115–122, September 2003.

[Agrawal 86] G. P. Agrawal & N. K. Dutta. Long-wavelength semiconductor lasers, pages 287–332. Van Nostrand Reinhold, New York, NY, 1986.

[Agrawal 93] G. P. Agrawal & N. K. Dutta. Semiconductor lasers. Van Nostrand Reinhold, New York, 1993.

[ALMA] ALMA. *Atacama Large Millimeter/Submillimeter Array.*

[Annovazzi-Lodi 98] V. Annovazzi-Lodi, A. Sciré, M. Sorel & S. Donati. *Dynamic behavior and locking of a semiconductor laser subjected to external injection.* IEEE Journal of Quantum Electronics, vol. 34, no. 12, pages 2350–2356, December 1998.

[Baney 98] D. M. Baney & W. V. Sorin. *High resolution optical frequency Analysis.* In D. Derickson, editeur, Fiber Optic Test and Measurement, pages 169–219. Prentice-Hall, New Jersey, 1998.

[Beernink 94] K. J. Beernink, R. L. Thornton & H. F. Chung. *Low threshold current dual wavelength planar buried heterostructure lasers with close spatial and large spectral separation.* Applied Physics Letters, vol. 64, no. 9, pages 1082–1084, February 1994.

[Bennett 90] B. R. Bennett, R. A. Soref & J. A. Del Alamo. *Carrier-induced change in refarctive index of InP, GaAs, and InGaAsP.* IEEE Journal of Quantum Electronics, vol. 26, no. 1, pages 113–122, January 1990.

[Bordonalli 94] A. C. Bordonalli, C. Walton & A. J. Seeds. *High-performance homodyne optical injection phase-lock loop using wide-linewidth semiconductor lasers.* IEEE Photonics Technology Letters, vol. 8, no. 9, pages 1217–1219, September 1994.

[Bragg 13] W.L. Bragg. *The diffraction of short electromagnetic waves by a crystal.* Proceedings of the Cambridge Philosophical Society, vol. 17, pages 43–57, November 1913.

[Braun 98] R. P. Braun, G. Grosskopf, D. Rohde & F. Schmidt. *Low-phase-noise millimeter-wave generation at 64 GHz and data transmission using optical sideband injection locking.* IEEE Photonics Technology Letters, vol. 10, no. 5, pages 728–730, May 1998.

[Buus 05] J. Buus, D. J. Blumenthal & M. Amann. Tunable laser diodes and related optical sources. Wiley & Sons, New York, 2005.

[CARMA] CARMA. *Combined Array for Research in Millimeter-wave Astronomy.* `http://www.mmarray.org`.

[Carroll 98] J. Carroll, J. Whiteaway & D. Plumb. Distributed feedback semiconductor lasers. IEE, Stevenage, 1998.

[Chen 00] Y. F. Chen. *CW dual-wavelength operation of a diode-end-pumped Nd:YVO_4 laser.* Applied Physics B: Lasers and Optics, vol. 70, no. 4, pages 475–478, April 2000.

[Chen 06] D. Y. Chen, Z. Deng & J. Yao. *Photonic generation of microwave signal using a dual-wavelength single-longitudinal-mode fiber ring laser.* IEEE Transactions on Microwave Theory and Techniques, vol. 54, no. 2, pages 804–809, February 2006.

[Coherent] Coherent. *Coherent Inc.* `http://www.coherentinc.com`.

[Coldren 95] L. A. Coldren & S. W. Corzine. Diode lasers and photonic integrated circuits. Wiley & Sons, New York, 1995.

[Coldren 00] L. A. Coldren. *Continuously-tunable single-frequency semiconductor lasers.* IEEE Journal of Selected Topics in Quantum Electronics, vol. 6, no. 6, pages 988–999, November/December 2000.

[Donati 99] S. Donati. Photodetectors: devices, circuits and applications. Prentice Hall, Englewood Cliffs NJ, 1999.

[Dorney 01] T. D. Dorney, R. G. Baraniuk & D. M. Mittleman. *Material parameter estimation with terahertz time-domain spec-*

troscopy. Jounal of the Optical Society of America A, vol. 18, no. 7, pages 1562–1570, July 2001.

[Dragoman 04] D. Dragoman & M. Dragoman. *Terahertz fields and applications.* Progress in Quantum Electronics, vol. 28, no. 1, pages 1–66, 2004.

[Dutta 86] N. K. Dutta, T. Cella, J. L. Ziko, D. A. Ackerman, A. B. Piccirilli & L. I. Greene. *InGaAsP closely spaced dual wavelength laser.* Applied Physics Letters, vol. 48, no. 25, pages 1725–1726, June 1986.

[Edwards 06] T. Edwards, D. Walsh, M. Spurr, C. Rae, M. Dunn & P. Browne. *Compact source of continuously and widely-tunable terahertz radiation.* Optics Express, vol. 14, no. 4, pages 1582–1589, February 2006.

[Erwin 07] G. Erwin. *Edge-emitting laser diodes with high-reflectivity 1D PBG mirrors.* PhD thesis, University of Glasgow, 2007.

[Forrester 55] A. Theodore Forrester, Richard A. Gudmundsen & Philip O. Johnson. *Photoelectric mixing of incoherent light.* Phys. Rev., vol. 99, no. 6, pages 1691–1700, Sep 1955.

[Fukushima 03] S. Fukushima, C. F. C. Silva, Y. Muramoto & A. J. Seeds. *Optoelectronics millimeter-wave synthesis using an optical frequency comb generator, optically injection locked lasers, and a unitraveling-carrier photodiode.* Journal of Lightwave Technology, vol. 21, pages 3043–3051, December 2003.

[Garcia-Garcia 04] J. Garcia-Garcia, F. Martín & R. E. Miles. *Optimization of micromachined reflex klystrons for operation at terahertz*

frequencies. IEEE Transactions on Microwave Theory and Techniques, vol. 52, no. 10, pages 2366–2370, October 2004.

[Garcia 97] J. Ch. Garcia, E. Rosencher, Ph. Collot, N. Laurent, J. L. Guyaux, B. Vinter & J. Nagle. *Epitaxially stacked lasers with Esaki junctions: A bipolar cascade laser.* Applied Physics Letters, vol. 71, no. 26, pages 3752–3754, December 1997.

[Gnan 06] M. Gnan, G. Bellanca, H. M. H. Chong, P. Bassi & R. M. De La Rue. *Modelling of photonic wire Bragg gratings.* Optical and Quantum Electronics, vol. 38, no. 1-3, pages 133–148, January 2006.

[Goldberg 83] L. Goldberg, H. F. Taylor, J. F. Weller & D. M. Bloom. *Microwave signal generation with injection-locked laser diodes.* Electronics Letters, vol. 19, no. 13, pages 491–493, June 1983.

[Gregory 05] I. S. Gregory, W. R. Tribe, M. J. Evans, T. D. Drysdale, D. R. S. Cumming & M. Missous. *Multi-channel homodyne detection of continuous-wave terahertz radiation.* Applied Physics Letters, vol. 87, no. 3, pages 034106–1–034106–3, July 2005.

[Grosskopf 00] G. Grosskopf, D. Rohde, R. Eggemann, S. Bauer, C. Bornholdt, M. Moehrle & B. Sartorius. *Optical millimeter-wave generation and wireless data transmission using a dual-mode laser.* IEEE Photonics Technology Letters, vol. 12, no. 12, pages 1692–1694, December 2000.

[Gu 98] P. Gu, M. Tani, M. Hyodo, K. Sakai & T. Hidaka. *Generation of cw-terahertz radiation using a two-longitudinal-mode laser diode.* Japanese Journal of Applied Physics, Part 2: Letters, vol. 37, no. 8B, pages L976–L978, August 1998.

[Gurov 99] I. P. Gurov & A. Kirienko. *Two-wavelength interferometric signal processing by recurrence filtering method.* In M. Hrabovsky, P. Tomanek & M. Miler, editeurs, Proc. SPIE Vol. 4016, p. 382-387, Photonics, Devices, and Systems, Miroslav Hrabovsky; Pavel Tomanek; Miroslav Miler; Eds., pages 382–387, december 1999.

[Harde 01] H. Harde, J. Zhao, M. Wolff, R.A. Cheville & D. Grischkowsky. *THz time-domain spectroscopy on ammonia.* Journal of Physical Chemistry A, vol. 105, no. 25, pages 6038–6047, April 2001.

[Henry 82] C. H. Henry. *Theory of the linewidth of semiconductor lasers.* IEEE Journal of Quantum Electronics, vol. 18, no. 2, pages 259–264, February 1982.

[Hidaka 91] T. Hidaka & Y. Hatano. *Simultaneous two wave oscillation LD using biperiodic binary grating.* Electronics Letters, vol. 27, no. 12, pages 105–106, June 1991.

[Hoffmann 04a] S. Hoffmann & M. Hofmann. *Two-color semiconductor laser for generation of THz radiation.* In European Semiconductor Laser Workshop 2004, 2004.

[Hoffmann 04b] S. Hoffmann, M. Hofmann, E. Bründermann & M. Havenith. *Four-wave mixing and direct terahertz emission with two-color semiconductor lasers.* Applied Physics Letters, vol. 84, no. 18, pages 3585–3587, May 2004.

[Huber 01] R. Huber, F. Tauser, A. Brodschelm, M. Bichler, G. Abstreiter & A. Leitenstorfer. *How many-particle interactions develop after ultrafast excitation of an electron-hole plasma.* Nature, vol. 414, pages 286–289, November 2001.

[Hyodo 96] M. Hyodo, M. Tani, S. Matsuura, N. Onodera & K. Sakai. *Generation of millimetre-wave radiation using a dual-longitudinal-mode microchip laser.* Electronics Letters, vol. 32, no. 17, pages 1589–1591, August 1996.

[Iio 95] S. Iio, M. Suehiro, T. Hirata & T. Hidaka. *Two-longitudinal-mode laser diodes.* IEEE Photonics Technology Letters, vol. 7, no. 9, pages 959–961, September 1995.

[IPHOBAC] IPHOBAC. *IPHOBAC project.* `http://www.ist-iphobac.org`.

[Ito 04] H. Ito, S. Kodama, Y. Muramoto, T. Furuta, T. Nagatsuma & T. Ishibashi. *High-speed and high-output InPInGaAs unitraveling-carrier photodiodes.* IEEE Journal of Selected Topics in Quantum Electronics, vol. 10, no. 4, pages 709–726, July/August 2004.

[Kamp 99] M. Kamp, J. Hofmann, A. Forchel, F. Schäfer & J. P. Reithmaier. *Low-threshold high-quantum-efficiency laterally gain-coupled InGaAs/AlGaAs distributed feedback lasers.* Applied Physics Letters, vol. 74, no. 4, pages 483–485, January 1999.

[Kim 03] H. C. Kim, H. Kanjo, S. Tamura & S. Arai. *Narrow-stripe distributed reflector lasers with first-order vertical grating and distributed Bragg reflectors.* IEEE Photonics Technology Letters, vol. 15, no. 8, pages 1032–1034, August 2003.

[Koch 02] M. Koch. *Bio-medical applications of THz imaging.* In D. Mittleman, editeur, Sensing with Terahertz Radiation, pages 287–332. Springer-Verlag, Heidelberg, 2002.

[Kogelnik 71] H. Kogelnik & C. V. Shank. *Stimulated emission in a periodic structure.* Applied Physics Letters, vol. 18, no. 4, pages 152–154, February 1971.

[Kogelnik 72] H. Kogelnik & C. V. Shank. *Coupled-wave theory of distributed feedback lasers.* Journal of Applied Physics, vol. 43, no. 5, pages 2327–2335, May 1972.

[Köhler 02] R. Köhler, A. Tredicucci, F. Beltram, H. E. Beere, E. H. Linfield, A. G. Davies, D. A. Ritchie, R. C. Iotti & F. Rossi. *Terahertz semiconductor-heterostructure laser.* Nature, vol. 417, no. 6885, pages 156–159, May 2002.

[Kou 06] Q. Kou, I. Yesilyurt & Y. Chen. *Collinear dual-color laser emission from a microfluidic dye laser.* Applied Physics Letters, vol. 88, no. 4, pages 091101–091103, February 2006.

[Kurobe 88] A. Kurobe, H. Furuyama, S. Naritsuka, N. Sugiyama, Y. Kokubun & M. Nakamura. *Effects of well number, cavity length, and facet reflectivity on the reduction of threshold current of GaAs/AlGaAs multiquantum well lasers.* IEEE Journal of Quantum Electronics, vol. 24, no. 4, pages 635–640, April 1988.

[Lammert 97] R. M. Lammert, J. S. Hughes, S. D. Roh, M. L. Osowski, A. M. Jones & J. J. Coleman. *Low-threshold narrow-linewidth InGaAsGaAs ridge-waveguide DBR lasers with first-order surface gratings.* IEEE Photonics Technology Letters, vol. 9, no. 2, pages 149–151, February 1997.

[Langley 99] L. N. Langley, M. D. Elkin, C. Edge, M. J. Wale, U. Gliese, X. Huang & A. J. Seeds. *Packaged semiconductor laser op-*

tical phase-locked loop (OPLL) for photonic generation, processing and transmission of microwave signals. IEEE Transactions on Microwave Theory and Techniques, vol. 47, no. 7, pages 1257–1264, July 1999.

[Leinonen 05] T. Leinonen, Y. A. Morozov, A. Härkönen & M. Pessa. *Vertical external-cavity surface-emitting laser for dual-wavelength generation.* IEEE Photonics Technology Letters, vol. 17, no. 12, pages 2508–2510, December 2005.

[Lima 95] C. R. Lima, D. Wake & P. A. Davies. *Compact optical millimetre-wave source using a dual-mode semiconductor laser.* Electronics Letters, vol. 31, no. 5, pages 364–366, March 1995.

[Lin 99] C. Lin, M. Wu, H. Shiao & K. Liu. *High-temperature, low threshold current, and uniform operation 1 X 12 monolithic AlGaInAs/InP strain-compensated multiple quantum well laser array in* 1.5 *mm.* IEEE Trans. on Electron Devices, vol. 46, no. 8, pages 1614–1618, August 1999.

[Macintyre 06] D. Macintyre & S. Thoms. Introduction to ebeam lithography. University of Glasgow, 2006.

[Marsh 99] J. H. Marsh & A. C. Bryce. *Impurity-free vacancy disordering of GaAs/AlGaAs quantum well structures: processing and devices.* In E. H. Li, editeur, Optoelectronic properties of semiconductor and superlattices, volume 8, pages 339–370. Taylor and Francis, London, 1999.

[Matus 04] M. Matus, M. Kolesik, J. V. Moloney, M. Hofmann & S. W. Koch. *Dynamics of two-color laser systems with spectrally*

filtered feedback. Journal of the Optical Society of America B, vol. 21, no. 10, pages 1758–1771, October 2004.

[McIntosh 95] K. A. McIntosh, E. R. Brown, K. B. Nichols, O. B. McMahon, W. F. Di Natale & T. M. Lyszczarz. *Terahertz photomixing with diode lasers in low-temperature-grown GaAs.* Applied Physics Letters, vol. 67, pages 3844–3846, December 1995.

[Miller 91] L. M. Miller, J. T. Verdeyen, J. J. Coleman, R. P. Bryan, J. J. Alwan, K. J. Beernink, & J. S. Hughes andT. M. Cockerill. *A distributed feedback ridge waveguide quantum well heterestructure laser.* IEEE Photonics Technology Letters, vol. 3, no. 1, pages 6–8, October 1991.

[Minch 99] J. Minch, S. H. Park, T. Keating & S. L. Chuang. *Theory and experiment of* $In_{1-x}Ga_xAs_yP_{1-y}$ *and* $In_{1-x-y}Ga_xAl_yAs$ *long-wavelength strained quantum-well lasers.* IEEE Journal of Quantum Electronics, vol. 35, no. 5, pages 771–782, May 1999.

[Mittleman 98] D. M. Mittleman, R. H. Jacobsen, R. Neelamani, R. G. Baraniuk & M. C. Nuss. *Gas sensing using terahertz time-domain spectroscopy.* Applied Physics B: Lasers and Optics, vol. 67, pages 379–390, September 1998.

[Möhrle 01] M. Möhrle, B. Sartorius, C. Bornholdt, S. Bauer, O. Brox, A. Sigmund, R. Steingrüber, M. Radziunas & H. J. Wünsche. *Detuned grating multisection-RW-DFB lasers for high-speed optical signal processing.* IEEE Journal of Selected Topics in Quantum Electronics, vol. 7, no. 2, pages 217–223, March 2001.

[Mueller 06] E. R. Mueller. *Terahertz radiation sources for imaging and sensing applications.* Photonics Spectra, vol. 67, pages 60–69, November 2006.

[ODaniel 06] J. K. ODaniel, O. V. Smolski & E. G. Johnson. *High efficiency dual-wavelength surface-emitting laser incorporating integrated dual-grating reflector.* IEEE Photonics Technology Letters, vol. 18, no. 3, pages 445–447, February 2006.

[Okai 93] M. Okai, M. Suzuki & T. Taniwatari. *Strained multiquantum-well corrugation-pitch-modulated distributed feedback laser with ultranarrow (3.6 kHz) spectral linewidth.* Electronics Letters, vol. 29, no. 19, pages 1696–1697, September 1993.

[Pellandini 97] P. Pellandini, R. P. Stanley, R. Houdré, U. Oesterle & M. Ilegems. *Dual-wavelength laser emission from a coupled semiconductor microcavity.* Applied Physics Letters, vol. 71, no. 7, pages 864–866, August 1997.

[Photon Design] Photon Design. *2D Mode Solver.* `http://www.photond.com/products/fimmwave.htm`.

[Ramos 92] R. T. Ramos & A. J. Seeds. *Fast heterodyne optical phase-lock loop using double quantum well laser diodes.* Electronics Letters, vol. 28, no. 1, pages 82–83, January 1992.

[Razavi 98] K. E. Razavi & P. A. Davies. *Semiconductors laser sources for the generation of millimetre-wave signals.* IEE Proceedings - Optoelectronics, vol. 145, no. 3, pages 159–163, June 1998.

[Renaudier 05] J. Renaudier, R. Brenot, B. Dagens, F. Lelarge, B. Rousseau, F. Poingt, O. Legouezigou, F. Pommereau, A. Accard, P. Gallion & G. -H. Duan. *45 GHz self-pulsation with narrow*

linewidth in quantum dots Fabry-Perot semiconductor lasers at 1.5 μm. Electronics Letters, vol. 41, no. 18, pages 1007–1008, September 2005.

[Rennon 01] S. Rennon, L. Bach, J. P. Reithmaier & A. Forchel. *Complex coupled distributed-feedback and Bragg-reflector lasers for monolithic device integration based on focused-ion-beam technology.* IEEE Journal of Selected Topics in Quantum Electronics, vol. 7, no. 2, pages 306–311, March/April 2001.

[Roh 00] S. D. Roh, T. S. Yeoh, R. B. Swint, A. E. Huber, C. Y. Woo, J. S. Hughes, & J. J. Coleman. *Dual-wavelength InGaAs-GaAs ridge waveguide distributed Bragg reflectors lasers with tunable mode separation.* IEEE Photonics Technology Letters, vol. 12, no. 10, pages 1307–1309, October 2000.

[SAFIR] SAFIR. *Single Aperture Far-Infrared observatory.* `http://safir.jpl.nasa.gov`.

[Sargent III 74] M. Sargent III, M. O. Scully & W. E. Lamb. Laser physics. Addison-Wesley, Reading, Mass., 1974.

[Shen 04] Y. C. Shen, P. C. Upadhya, H. E. Beere, E. H. Linfield, A. G. Davies, I. S. Gregory, C. Baker, W. R. Tribe & M. J. Evans. *Generation and detection of ultrabroadband terahertz radiation using photoconductive emitters and receivers.* Applied Physics Letters, vol. 85, no. 2, pages 164–166, July 2004.

[Shinoda 03] K. Shinoda, K. Nakahara & H. Uchiyama. *InGaAlAs/InP ridge-waveguide lasers fabricated by highly selective dry etching in $CH_4/H_2/O_2$ plasma.* In International Conference Indium Phosphide and Related Materials (IPRM) 2003, pages 550–553, Santa Barbara, CA, May 2003.

[Shiraz 96] H. Ghafouri Shiraz. Distributed feedback laser diodes. Wiley & Sons, New York, 1996.

[Siebert 02] K. J. Siebert, H. Quast, R. Leonhardt, T. Löffler, M. Thomson, T. Bauer, H. G. Roskos & S. Czasch. *Continuous-wave all-optoelectronic terahertz imaging.* Applied Physics Letters, vol. 80, no. 16, pages 3003–3005, April 2002.

[Siegman 86] A. E. Siegman. Lasers. University Science Books, Sausalito, 1986.

[Skogen 05] E. J. Skogen, J. W. Raring, G. B. Morrison, C. S. Wang, V. Lal, M. L. Mašanović & L. A. Coldren. *Monolithically integrated active components: a quantum-qell intermixing approach.* IEEE Journal of Selected Topics in Quantum Electronics, vol. 11, no. 2, pages 343–355, March/April 2005.

[Stöhr 01] A. Stöhr, R. Heinzelmann, A. Malcoci & D. Jäger. *Optical heterodyne millimeter-wave generation using 1.55-μm traveling-wave photodetectors.* IEEE Transactions on Microwave Theory and Techniques, vol. 49, no. 10, pages 1926–, October 2001.

[Strain 06] M. J. Strain & M. Sorel. *Post-growth fabrication and characterization of integrated chirped Bragg gratings on GaAsAlGaAs.* IEEE Photonics Technology Letters, vol. 18, no. 24, pages 2566–2568, December 2006.

[SWAS] SWAS. *SWAS, Submillimeter Wave Astronomy Satellite.* `http://cfa-www.harvard.edu/swas/instrument.html`.

[Tani 00] M. Tani, P. Gu, M. Hyodo, K. Sakai & T. Hidaka. *Generation of coherent terahertz radiation by photomixing of dual-mode*

lasers. Optical and Quantum Electronics, vol. 32, pages 503–520, May 2000.

[Tani 05] M. Tani, O. Morikawa, S. Matsuura & M. Hangyo. *Generation of terahertz radiation by photomixing with dual- and multiple-mode lasers.* Semiconductor Science Technology, vol. 20, pages S151–S163, July 2005.

[Tanner EDA] Tanner EDA. *(Electronic Design Automation) softwares.*

[Teich 68] M. C. Teich. *Infrared heterodyne detection.* Proceedings of the IEEE, vol. 56, no. 1, pages 37–46, January 1968.

[Teng 00] J. H. Teng, S. J. Chua, Z. H. Zhang, Y. H. Huang, G. Li, & Z. J. Wang. *Dual-wavelength laser source monolithically integrated with Y-junction coupler and isolator using quantum-well intermixing.* IEEE Photonics Technology Letters, vol. 12, no. 10, pages 1310–1312, October 2000.

[TeraView] TeraView. *TeraView Limited.* `http://www.teraview.com`.

[THz-BRIDGE] THz-BRIDGE. *THz-BRIDGE project.* `http://www.frascati.enea.it/THz-BRIDGE`.

[THz-network] THz-network. `http://www.thznetwork.org`.

[Tiberio 94] R. C. Tiberio, P. F. Chapman, R. D. Martin, S. Forouhar & R. J. Lang. *Laterally coupled distributed feedback lasers fabricated with electron-beam lithography and chemically assisted ion-beam etching.* Journal of Vacuum Science and Technology B, vol. 12, no. 6, pages 3746–3749, November/December 1994.

[Tojo 05] T. Tojo, K. Yamanaka, B. P. Singh, K. Onozawa, D. Ueda, I. Soga, K. Maezawa & T. Mizutani. *Dual-wavelength high-power laser diodes fabricated by selective fluidic self-assembly.* Japanese Journal of Applied Physics, Part 1: Regular Papers and Short Notes and Review Papers, vol. 44, no. 4 B, pages 2568–2571, April 2005.

[Tredicucci 05] A. Tredicucci, R. K öhler, L. Mahler, H. E. Beere, E. H. Linfield & D. A. Ritchie. *Terahertz quantum cascade lasersfirst demonstration and novel concepts.* Semiconductor Science Technology, vol. 20, pages S222–S227, June 2005.

[Uchida 05] S. Uchida, S. Agatsuma, N. Hoshi, K. Tanno, H. Iki, S. Yoshida, S. Satoh, Y. Asano, K. Sahara & T. Yamamoto. *Monolithic dual-wavelength high-power lasers for CD-R/DVD ± R/RW/RAM.* IEEE Journal of Selected Topics in Quantum Electronics, vol. 11, no. 5, pages 1148–1152, September/October 2005.

[Valle 95] A. Valle, J. Sarma & K. A. Shore. *Spatial holeburning effects on the dynamics of vertical cavity surface-emitting laser diodes.* IEEE Journal of Quantum Electronics, vol. 31, no. 8, pages 1423–1431, August 1995.

[Walton 98] C. Walton, A. C. Bordonalli & A. J. Seeds. *High-performance heterodyne optical injection phase-lock loop using wide linewidth semiconductor lasers.* IEEE Photonics Technology Letters, vol. 10, no. 3, pages 427–429, March 1998.

[Wang 99] X. Wang, W. Mao, M. Al-Mumin, S. A. Pappert, J. Hong & G. Li. *Optical generation of microwave/millimeter-wave sig-*

nals using two-section gain-coupled DFB lasers. IEEE Photonics Technology Letters, vol. 11, no. 10, pages 1292–1294, October 1999.

[Wang 05a] J. Wang, J. B. Tian, P. F. Cai, B. Xiong, C. Z. Sun & Y. Luo. *1.55-μm AlGaInAsInP laterally coupled distributed feedback laser.* IEEE Photonics Technology Letters, vol. 17, no. 7, pages 1372–1374, July 2005.

[Wang 05b] W. Wang, M. Cada, J. Seregelyi, S. Paquet, S. J. Mihailov & P. Lu. *A beat-frequency tunable dual-mode fiber-Bragg-grating external-cavity laser.* IEEE Photonics Technology Letters, vol. 7, no. 11, pages 2436–2438, November 2005.

[Wiedmann 01] J. Wiedmann, K. Ebihara, H. C. Kim, B. Chen, M. Ohta, K. Matsui, S. Tamura, J.-I. Shim & S. Arai. 1.5 *mm wavelength distributed reflector lasers with vertical grating.* Electronics Letters, vol. 37, no. 13, pages 831–832, June 2001.

[Wilk 07] R. Wilk, A. Klehr, M. Mikulics, M. Walther & M. Koch. *Terahertz generation with a 1064nm DFB laser diode.* Electronics Letters, vol. 43, no. 2, pages 108–110, January 2007.

[Williams 06] B. S. Williams, S. Kumar, Q. Hu & J.L. Reno. *High-power terahertz quantum-cascade lasers.* Electronics Letters, vol. 42, no. 2, pages 89–91, January 2006.

[Wong 93] V. V. Wong, W. Y. Choi, J. M. Carter, C. G. Fonstad & H. I. Smith. *Ridge-waveguide sidewall-grating distributed feedback structures fabricated by x-ray lithography.* Journal of Vacuum Science and Technology B, vol. 11, no. 6, pages 2621–2624, November/December 1993.

[Wong 05] H. Y. Wong. *InGAAs/InAlGaAs monolitically integrated Mach-Zehnder interferometer devices.* PhD thesis, University of Glasgow, 2005.

[Woodward 03] R. M. Woodward, V. P. Wallace, R. J. Pye, B. E. Cole, D. D. Arnone, E. H. Linfield & M. Pepper. *Terahertz pulse imaging of ex vivo basal cell carcinoma.* Journal of Investigative Dermatology, vol. 120, no. 1, pages 72–78, January 2003.

[Woolard 05] D. L. Woolard, E. R. Brown, M.Pepper & M. Kemp. *Terahertz Frequency Sensing and Imaging: A Time of Reckoning Future Applications?* Proceedings of the IEEE, vol. 93, no. 10, pages 1722–1743, October 2005.

[Yan 06] J. Yan, J. Cai, G. Ru, X. Yu, J. Fan & F. S. Choa. *InGaAsPInP dual-wavelength bipolar cascade lasers.* IEEE Photonics Technology Letters, vol. 18, no. 16, pages 1777–1779, August 2006.

[Yanson 02] D. A. Yanson, M. W. Street, S. D. McDougall, I. G. Thayne, J. H. Marsh & E. A. Avrutin. *Ultrafast harmonic modelocking of monolithic compound-cavity laser diodes incorporating photonic-bandgap reflectors.* IEEE Journal of Quantum Electronics, vol. 38, no. 1, pages 1–11, January 2002.

[Yee 95] H. H. Yee. *Semiconductor quantum-well extended cavity lasers and deep-surface gratings for distributed Bragg reflector lasers.* PhD thesis, University of Glasgow, 1995.

[Yee 99] H.H. Yee, S. Ayling & R.M. De La Rue. *Surface-grating distributed Bragg reflector quantum-well lasers fabricated in AlGaAs-GaAs asymmetric epitaxial waveguides.* Applied Optics, vol. 38, no. 30, pages 6325–6332, October 1999.

[Yu 97] J. Yu, P. Rambaldi & J.-P. Wolf. *Dual-wavelength diode-seeded Ti:sapphire laser for differential absorption lidar applications.* Applied Optics, vol. 36, pages 6864–6868, september 1997.